ISSN en trámite

Geofísica Internacional

Revista Trimestral Publicada por el Instituto de Geofísica de la Universidad Nacional Autónoma de México

México
Volume 57 Number 1
January - March
2018

— Geofísica Internacional —

GEOFÍSICA INTERNACIONAL, Año 57, Vol. 57, Núm. 1, enero - marzo de 2018 es una publicación trimestral, editada por la Universidad Nacional Autónoma de México, Ciudad Universitaria, Alcaldía Coyoacán, C.P. 04150, Ciudad de México, a través del Instituto de Geofísica, Circuito de la Investigación Científica s/n, Ciudad Universitaria, Alcaldía Coyoacán, C.P. 04150, Ciudad de México, Tel. (55)56 22 41 15. URL: http://revistagi.geofisica.unam.mx, correo electrónico: revistagi@igeofisica.unam.mx. Editora responsable: Andrea Rostan Robledo. Certificado de Reserva de Derechos al uso Exclusivo del Título: 04-2022-081610251200-102, ISSN: en trámite, otorgados por el Instituto Nacional del Derecho de Autor (INDAUTOR). Responsable de la última actualización Saúl Armendáriz Sánchez, Editor Técnico. Fecha de la última modificación: 31 de diciembre 2017, Circuito de la Investigación Científica s/n, Ciudad Universitaria, Alcaldía Coyoacán, C.P. 04150, Ciudad de México.

Geofísica Internacional

Vol. 57, Núm. 1, enero-marzo de 2018

Contents

Geofísica
Internacional

Evidence of small ferrimagnetic concentrations in mice (Mus musculus) livers and kidneys exposed to the urban dust: A reconnaissance study.

Francisco Bautista, María E. Gonsebatt,, Rubén Cejudo, Avto Goguitchaichvili, Ma. Carmen Delgado, Juan J. Morales. Francisco Bautista, María E. Gonsebatt,, Rubén Cejudo, Avto Goguitchaichvili, Ma. Carmen Delgado, Juan J. Morales

Geofísica Internacional (2018) 57-1: 9-10

Original paper

Application of multiple proxies in Mexican tropical coasts to prove evidence of tsunami deposits

Comment To: Ocampo-Rios, et al., *Geofisica Internacional, 56*(1), 2017. DOI: 10.19155/geofint.2017.056.1.4

María Teresa Ramírez-Herrera*, Avto Goguitchaichvili, Francisco Bautista, Patricia Quintana, Ana-Carolina Ruiz-Fernández, Néstor Corona, Violeta Rangel, Marcelo Lagos, Vladimir Kostoglodov, Maria Luisa Machain, Daniel Aguilar Treviño, Rocío Castillo-Aja, Krzysztof Gaidzik

Received: August 17, 2017; accepted: October 06, 2017; published on line: January 01, 2018

The study of tsunami deposits has significantly advanced since the Chilean 2010 and Tohoku 2011 tsunamis providing opportunities to analyze tsunami deposits and their characteristics (Rubin *et al*., 2017). In tropical environments, the combination of multiple proxies has demonstrated to be a necessity to prove evidence of ancient earthquakes and tsunamis (Ramirez-Herrera *et al*., 2012, 2016; Williams *et al*., 2011). Challenges faced in the study of tsunami deposits in tropical areas frequently affected by hurricanes, lead to problems of differentiation between tsunami and storm deposits, and misinterpretations of climate/seasonal changes.

Ocampo-Rios *et al*. (2017) attempted to study the geologic evidence of the 1985 tsunami in Barra de Potosí, México. Their assertion that an "erosive base" is the only tool to prove the existence of tsunami deposits is not correct. (1) Our previous work in the Barra de Potosí area (field and survey-based interviews to witnesses of the 1985 tsunami) indicate that the area around the village has been intervened by human activity, thus surficial sediments are not reliable. (2) Beaches are very dynamic, and are located where normally tsunami erosion occur, thus, this type of environments are not suitable for tsunami deposits preservation. (3) Ramirez-Herrera *et al*. (2012) research results

M.T. Ramírez-Herrera*
V. Rangel
Laboratorio Universitario de Geofísica Ambiental
Instituto de Geografía
Universidad Nacional Autónoma de México
*Corresponding author: tramirez@igg.unam.mx

A. Goguitchaichvili
Laboratorio Universitario de Geofísica Ambiental
Instituto de Geofísica
Universidad Nacional Autónoma de México
Unidad Michoacán, UNAM-Campus Morelia, México

F. Bautista
Laboratorio Universitario de Geofísica Ambiental
Centro de Investigaciones en Geografía Ambiental
Universidad Nacional Autónoma de México
Campus Morelia, Morelia, México

P. Quintana
D. Aguilar Treviño
Centro de Investigaciones y Estudios Avanzados,
Unidad Mérida, Yucatán, México

A.C. Ruiz-Fernández
Instituto de Ciencias del Mar y Limnología
Universidad Nacional Autónoma de México
Unidad Académica Mazatlán, Mazatlán, México

N. Corona
Centro de Estudios en Geografía Humana
El Colegio de Michoacán A.C., Michoacán, México

M. Lagos
Instituto de Geografía, Laboratorio de Tsunamis
Pontificia Universidad Católica de Chile
Santiago, Chile

V. Kostoglodov
Instituto de Geofísica
Universidad Nacional Autónoma de México
Ciudad de México, México

M.L. Machain
Instituto de Ciencias del Mar y Limnología
Universidad Nacional Autónoma de México
Ciudad Universitaria, Ciudad de México, México

R. Castillo-Aja
Posgrado en Geografía
Universidad Nacional Autónoma de México
Ciudad Universitaria, Ciudad de México, México

K. Gaidzik
Department of Fundamental Geology
University of Silesia, Poland

come from sites in the Ixtapa estuary and not from Zihuatanejo Bay, i.e. a completely different geomorphic setting that consequently changes the tsunami impact and distribution of tsunami deposits. Thus, comparison by Ocampo-Rios *et al*. (2017) with their sites is inadequate. (4) Ocampo-Rios *et al*. (2017) hydraulic roughness calculation (0.02) to determine the inundation limit shows inaccuracies. Values from 0.011 to 0.02 apply to flood plains with very irregular shape which is not the case for Ixtapa estuary studied by Ramirez-Herrera *et al*. (2012) nor is the Zihuatanejo Bay. The calculation of Manning´s values for the specific location (using the local topography, vegetation density, presence of barriers, etc.) is more appropriate than using standardized Manning´s values. We reassessed here the tsunami flooding area interpreted by Ocampo-Rios *et al*. (2017) using their data and demonstrate that their results are not correct, the inundation continues beyond 700 m in both Zihuatanejo and Barra de Potosi areas. (5) . Mineral content and assemblages are source-dependent and therefore, they are not a useful tool alone to identify tsunami deposits (Jagodzinski *et al*., 2012). (6) Except for the Br concentration values, Ocampo-Rios *et al*. (2017) do not show significant differences in the elemental composition of the "pre-tsunami" and "tsunami deposits". The explanation provided on the low concentrations of Na, Cl and Br is not plausible. These elements have been widely used to identify marine provenance on sediment paleorecords along coastal areas. Br concentrations on soils can vary from 5 to 40 ppm, while on marine sediments they can reach up to 300 ppm (e.g. Ruiz-Fernández *et al*., 2016). The oxides used to demonstrate tsunami origin of the Barra de Potosi sediments named "tsunami deposits", i.e. SiO_2 and TiO_2, if there was in fact any significant difference in values, would prove terrigenous characteristics and origin, and not marine. In summary, multiple proxies are required to prove evidence of tsunami deposits.

References

Jagodzinski *et al*. 2012. DOI:10.1016/j.sedgeo.2012.07.015

Ocampo-Rios *et al* (2017).

Ramirez-Herrera *et al*. 2012. DOI:10.1016/j.geomorph.2011.11.002

Ramirez-Herrera *et al*. 2016. DOI:1016/j.geomorph.2016.02.011

Ruiz-Fernández *et al*. 2016. DOI:10.1177/0959683616632882

Rubin *et al*., 2017. DOI: 10.1038/ncomms16019, Williams et al. 2011. DOI: 10.23919/OCEANS.2011.6107137

Geofísica Internacional (2018) 57-1: 11-12

Original paper

Tsunami deposit research in Mexico compels multi-disciplinary approach, not just multi-proxy application

Reply to: Comment by Ramírez-Herrera, *et al*.

Priyadarsi D. Roy*, M.P. Jonathan, José Luis Sanchez-Zavala, Ma. Consuelo Macias, Rufino Lozano-Santacruz, Brenda Grisset Ocampo-Rios

Received: October 10, 2017; accepted: ; published on line: January 01, 2018

There has been an upsurge in geological and biological characterization of tsunami deposits after the 2004 Indian Ocean tsunami with the intention to identify paleo-tsunami events in sedimentary archives (Goff *et al*., 2011). Although there is noteworthy progress in recent years, there is still no perfect recipe to identify deposits associated with paleo-tsunami. Similarity between tsunami and storm deposits in coastal regions and the lack of any global proxy to identify paleo-tsunami, continue to be some of the main limitations. Tsunami deposits from different parts exhibited variable grain size, sediment structure and mineralogy. Some contain and others lack of marine fauna and shell fragments. One approach to overcome the limitations is the characterization of known-tsunami deposits in different regions and the documentation of possible independent proxies for different parts of the world. The paper by Ocampo-Rios *et al*. (2017) is a small step in that direction since it documented the geological characteristics (our expertise) of a known-tsunami deposit. It also compared various recent tsunami deposits from near-by sites with similar geomorphological and geological settings in order to uncover a local proxy for the southwestern Mexico. Only the erosive base was useful among the entire observed characteristics.

Contrary to the critics' comments, Ocampo-Rios *et al*. (2017) presented geological characteristics of sediments deposited by the 1985 tsunami at margins of the El Potosi estuary (up to 15-70 cm depth) at distances of >600 m from the shore. It is quite possible that inundation continued beyond 700 m and that far away sites also host tsunami deposits. Hydrological roughness was calculated from the inundation limit and the estimated roughness (for lagoons) was helpful in testing the eyewitness account. Geological proxies were not used to identify any paleo-tsunami deposit and the inundation limit was never estimated from the Manning's number. Similarly, the comparable chemical compositions of tsunami as well as non-tsunami deposits were a consequence of the geology of southwestern Mexico and its mineralogical composition. Considering the proximity of the Middle American Trench and the southwestern coast of Mexico, it is most probable that sediments transported by fluvial activity into the Pacific Ocean were reworked from the continental shelf by the tsunami waves and deposited in the estuary. The absence of higher Na_2O and Br in sediments deposited during a tsunami that occurred more than two decades before the sampling expedition were due to the lack of preservation or dissolution of highly soluble Na and Br-bearing salt minerals (deposited by sea water) in the sedimentary archive by several years of pluvial/fluvial activity (Chagué-Goff, 2010). Oxides of Si (quartz and feldspars) and Ti (mafic and heavy minerals) represent the mineralogical composition and they cannot be used as proxies to differentiate between continental and marine sources. In this particular case, minerals eroded from the Guerrero Composite Terrain (Centeno-García *et al*., 2011) were reworked from the Pacific

P.D. Roy*
J.L. Sanchez-Zavala
Ma. Consuelo Macias
R. Lozano-Santacruz
Instituto de Geología
Universidad Nacional Autónoma de México
Ciudad Universitaria
Delegación Coyoacán, CP 04510
México CDMX, México
*Corresponding author: roy@geologia.unam.mx

M.P. Jonathan
Centro Interdisciplinario de Investigaciones
y Estudios sobre Medio Ambiente y Desarrollo
Instituto Politécnico Nacional
Calle 30 de Junio de 1520, Barrio La Laguna Ticomán
Delegación Gustavo A. Madero, CP 07340
México, CDMX, México

B.G. Ocampo-Rios
Posgrado en Ciencias de la Tierra
Universidad Nacional Autónoma de México
Ciudad Universitaria
Delegación Coyoacán, CP 04510
México CDMX, México

Ocean into the estuary. However, we appreciate the comments since they provided a platform to discuss if simple multi-proxy application is sufficient, or the tsunami sediment research in Mexico compels a multi-disciplinary approach with the participation of experts from different disciplines.

References

Chagué-Goff C., 2010, Chemical signatures of palaeotsunamis: A forgotten proxy?, *Marine Geology*, 271, 67-71.

Centeno-García E., Busby C., Busby M., Gehrels G., 2011, Evolution of the Guerrero composite terrane along the Mexican margin, from extensional fringing arc to contractional continental arc., *GSA Bull*., 123, 9-10, 1776 -1797.

Goff J., Chagué-Goff C., Dominey-Howes D., McAdoo B., Cronin S., Bonté-Grapetin M., Nichol S., Horrocks M., Cisternas M., Lamarche G., Pelletier B., Jaffe B., Dudley W., 2011, Palaeotsunamis in the Pacific Islands. *Earth-Sci. Rev.*, 107, 1-2, 141-146.

Ocampo-Rios BG., Roy P.D., Marcías M.C., Jonathan M.P., Lozano-Santacruz R., 2017, Tsunami deposits of September 21st 1985 in Barra de Potosí: comparison with other studies and evaluation of some geological proxies for southwestern Mexico. Geofisica Internacional, 56, 1, 57-69.

Geofísica Internacional (2018) 57-1: 13-38

Original paper

Understanding active volcanoes: the case of Usu Volcano, Japan, with emphasis on the 1977 summit eruption

I. Yokoyama and N. Matsushima

Received: September 13, 2017; accepted: October 30, 2017; published on line: January 01, 2018

Resumen

Comprender el comportamiento de un volcán activo requiere un análisis multidisciplinario de sus actividades pasadas y presentes. En este trabajo se pretenden explicar los mecanismos eruptivos del volcán Usu, uno de los volcanes activos más pequeños del mundo, pero no por ello menos peligroso, ya que ha producido diversos tipos de erupciones como eyecciones de pómez, cenizas y piroclastos y la formación de domos de lava en la cumbre y en su base. La actividad pasada del volcán, particularmente las erupciones piroclásticas, se discute brevemente basado en los artículos y mapas geológicos publicados. Usu es un volcán dacítico que ha producido erupciones desde la cumbre y desde bocas parásitas en su base, como las de 1910 y 1943. La primera fue freática y la segunda produjo un domo de lava. La erupción de 1977 inició con una erupción pumítica en la cumbre y continuó con erupciones freáticas por más de 5 años. La erupción de 2000 fue freato-magmática, desde la base NW. Las erupciones de este volcán desde el siglo 17 muestran un tiempo de recurrencia media de 57 años. La erupción de 1977 es una de las más grandes y fue un caso típico de las erupciones de la cumbre. El objetivo de esta recopilación de las diversas observaciones geofísicas de esa erupción contribuye a la comprensión de su estructura interna y de los mecanismos de erupción del Usu.

Palabras clave: Erupciones desde la cumbre, erupción parásita, modelo de fractura por cizalla, movimiento de bloque, estructura del volcán, depósito de magma.

Abstract

Understanding the behavior of an active volcano requires a multidisciplinary analysis of its past and present activities. The aim of the present study is to explain the eruption mechanisms of Usu Volcano, which is one of the smallest active volcanoes of the world, yet a hazardous one as it has produced various types of eruptive activity such as pumice, ash and pyroclastic ejections, and the formation of lava domes at the summit and at its base. The past activity of the volcano, particularly the pyroclastic eruptions, is briefly discussed on the basis of the published papers and geologic maps. Usu is a dacitic volcano that has produced summit and basal eruptions from parasitic vents, as those of 1910 and 1943. The former was phreatic and the latter resulted in a lava dome formation. The 1977 eruption began with a pumice eruption at the summit, and phreatic eruptions continued for over 5 years. The 2000 eruption was phreato-magmatic with the outbreak at the NW base. The eruptions of this volcano since 17th century show a 57-year mean recurrence time. The 1977 eruption is one of the largest and was a typical case of the summit eruptions. This compilation of the various geophysical observations of this eruption will contribute in the understanding of its internal structure and of the eruption mechanisms of this volcano.

Key words: Summit eruption, parasitic eruption, shear fracture model, block movement, volcano structure, magma reservoir.

I. Yokoyama*
The Japan Academy
Ueno Park, 7-32, Taito-ku,
Tokyo, 110-0007, Japan

N. Matsushima
Geological Survey of Japan
1-1-3 Higashi, Tsukuba
Ibaraki, 305-8567, Japan
*Corresponding author:

1. Introduction

Usu Volcano is located in the S part of Hokkaido Island (Figure 1) and was formed about 30,000 y BP. This volcano is one of the world's smallest active stratovolcanoes, measuring 6 km in basal diameter and 0.5 km in relative height. Usu has produced various types of eruptive activity including ejection of pumice, ash and pyroclasts, and the formation of lava domes at the summit and at the base. It is a dacitic volcano that has erupted about every 57 years, in average, since the 17th century. The present study of the different types of volcanic activity at Usu, and of the multiple geophysical observations on it is aimed to improve our understanding of the eruption dynamics of Usu and of active volcanoes in general.

Historical records in Hokkaido are short, only after 17th century. The first recorded eruption of Usu Volcano was at the summit in 1663 and subsequently, the volcano repeated eruptions at the summit and the base. In the last summit eruption in August 1977, coinciding with the timely development of the activity, the new volcano observatory belonging to the University of Hokkaido began its observation routine. The volcanic activity continued till around 1982. In the present paper, these activities are simply named the 1977 eruption. And in 2000, a parasitic eruption occurred at the NW base.

During these periods, many papers were published after each respective eruption. However, there still remain many unsolved problems. To discuss some of them, the present authors would like to address some questions about the 1977-1982 eruption of Usu Volcano.

Tōya caldera was formed with pumice flows about 110,000 YBP, and presently, its rims are not clearly distinguishable. The original caldera rims may have been dissected and the caldera area expanded. In Figure 2, the thick broken contour connects triangulation points on peak lines, and does not outline the caldera rim. The red contours show the Bouguer gravity anomalies on Tōya caldera in mgal (Yokoyama, 1964), roughly corresponding to the caldera depression. Based on the gravity anomalies, the original Tōya caldera can be estimated to be about 8 km in diameter. A probable caldera boundary is shown by the thin black broken line in Figure 2. The post-caldera activities resulted in formation of Nakajima Island (andesitic rocks) at the center of the caldera, and Usu Volcano was initially formed about 30,000 y BP with basaltic rocks. Usu volcano is located on the rim or nearly outside of Tōya caldera. Such relationship is similar to that between Aira caldera and Sakurajima volcano in Kyushu, and that between Krakatau and Anak Krakatau in the Sunda straits (Bemmelen, 1949). In general, during the post-caldera activities, it may be difficult for magma to develop new conduits in the "soft" caldera deposits and would prefer to select conduits along the boundaries between caldera deposits and basements.

In Section 2, the eruptive history of Usu Volcano is reviewed from a geological viewpoint. Section 3 is focused on summarizing past eruptions from the standpoints of associated physical manifestations such as explosions, seismicity, and deformations, with emphasis on the parasitic eruptions, and introducing a tectonic structural line (TSL) at the N base of

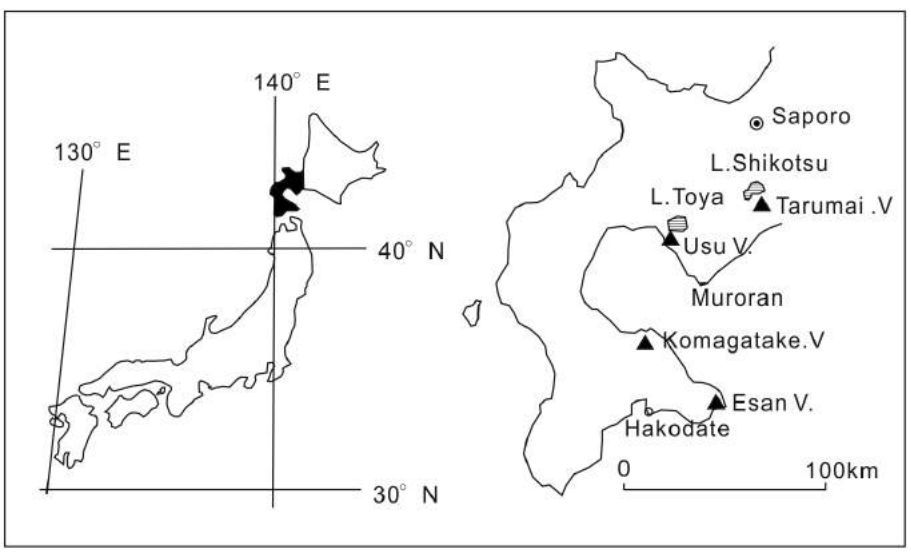

Figure 1. Location map of Usu Volcano.

Usu volcano, which is not directly related to the boundary of Tōya caldera. In Section 4 the 1977 summit eruption is discussed and a hypothetical model of the block movements of the upper part of the volcano is presented. In Section 5, subsurface structure of the volcano from various geophysical observations such as P- and S-wave velocity structure, aquifer configuration, electrical resistivity and muographic outline of the summit are discussed. The five main results obtained in the present paper are finally detailed.

At this point a special mention is made of two technical terms to be used in this work:

Craterlet: The activity of Usu Volcano formed many explosion craters in the summit and at the base, usually shallow and with small diameters. In the present paper, to avoid confusion between the summit crater and the explosion craters, the latter shall be named "craterlet" after Ōmori (1911, 1913). These craterlets may be ephemeral since they are rather small in dimension.

Lava dome and mound: Once the 1910 hill or Meiji-Shinzan (new mountain formed in the Meiji era (ab. MS) was called cryptodome. Later, Tanaka and Yokoyama (2013) based on muography (cf. 4.2. Parasitic eruptions) proved it to be a mound without any hidden domes; it was forced up by magma intrusion. The magma intrusion front remains at a depth of about 70 m. In the present paper, cryptodomes and mounds are told apart. Such a structure would be formed by viscous dacitic magmas.

In the following, the discussion will be initiated with the volcano activities during historical time after 1663, and proceed to the 20th century, and finally concentrate on the 1977 eruption.

2. Activities of Usu Volcano in historical times

2.1 Historical eruptions of Usu Volcano

Historical records of Hokkaido Island are rather short and eruptions of Usu Volcano have been recorded only after the 1663 eruption as summarized in the Table 1.

Usu Volcano is considered small, measuring 6 km in the basal diameter and 500 m in relative height, making it one of the smallest active volcanoes of the world. It is also remarkable that eruption activity has occurred almost regularly in time since 1663, with 57 years as the longest interval between the eruptions, and that the eruption sites irregularly changed between the summit and the base. In historical times, it has not erupted simultaneously at the summit crater and the base. At the base of the volcano, we have observed three parasitic eruptions since 1910, and the 1977 eruption was the first summit eruption after 1853. At present, we cannot predict where the next eruption will occur.

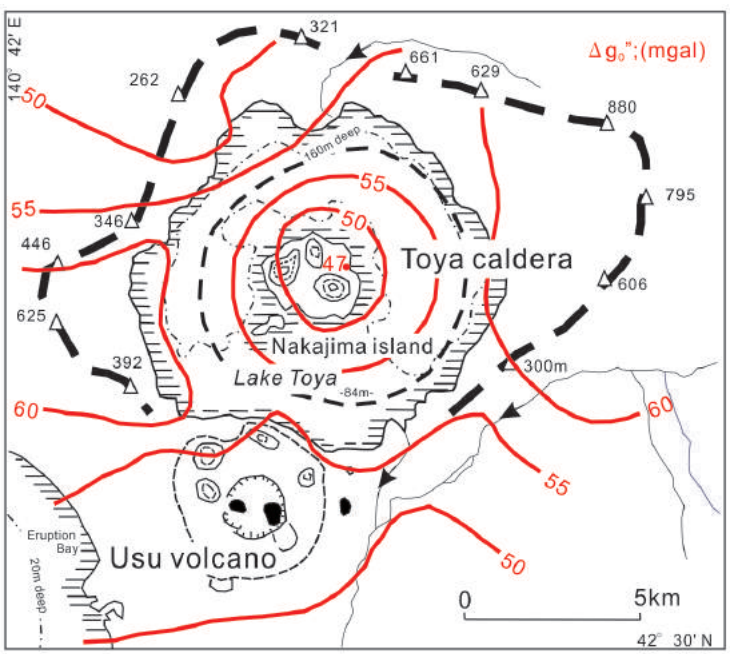

Figure 2. Tōya caldera and Usu Volcano. Thick broken line connects topographic peaks around the lake. Red contours show Bouguer gravity anomalies mainly on Tōya caldera (Yokoyama, 1964). 47 mgal at the island is the minimum value. A thin broken line outlines the probable caldera boundary.

Table 1. Eruptions of Usu Volcano in historical times.

Period	Interval (years)	Eruption site	Type of activity	Type of ejecta	Volume of ejecta and lavas (km^3 DRE)
1) 1663		summit	base-surge	pyroclastic flows (Us-b)	~ 1
1')	>pre-1769				
2) 1769		summit	Ko-Usu lava dome	ash	0.03
	>53				
3) 1822		summit	Ogariyama mound	"Bunsei nue ardente"	0.02
	>31				
4) 1853		summit	Oo-Usu lava dome	pyroclastic flows	0.05
	>57				
5) 1910		N base	craterlets and mounds	ash	small
	>33				
6) 1943		E base	Showa-Shinzan lava dome	ash	0.05
	>34				
7) 1977		summit	craterlets and deformations	pumice and ash	0.03
	>23				
8) 2000		NW base	craterlets	ash	0.0001

1') Between the 1663 and 1769 eruptions, Nakagawa *et al*. (2005) found the deposits of an unknown eruption. Underlined: Distributions of the ejecta are shown in Figure 3. Volume estimates of the ejecta are approximate.

Table 1 shows a wide range of eruption styles, including phreatic, pumice, pyroclastic eruptions, and mound and dome formation. Such sequence of varying volcanic activity is characteristic of this volcano. Matsumoto and Nakagawa (2010, Figure 6) discussed petrology of the volcanic rocks of Usu Volcano: One of their results shows that SiO_2 content of the whole-rock components of historical ejecta has decreased almost linearly from 75 % of 1663 to 70 % of 2000. This means that the Usu magmatic system has changed since 1663 from rhyolite to dacite, causing a decrease of the magma viscosity with time according to the experimental results of Goto (1997).

2.2 Pyroclastic ejecta in historical times

Katsui (1973) studied pyroclastic deposits, falls and flows, on and around Usu Volcano. Three typical ash falls are depicted in Figure 3 where the explosion of the 1769 and the 1822 ash emissions are known as Ko-Usu dome and Ogari-yama mound, respectively. The origin of the 1663 ash surges is not clear. It is very important to determine the exact eruption center of each pyroclastic flow. In the figure, the location of the eruption centers are estimated, considering E-ward drifts as prevailing winds in this area. Probably, the 1769 pyroclastic falls may have occurred simultaneously with the growth of Ko-Usu dome. The 1853 pyroclastic flows may have been caused by collapses of the new Oo-Usu lava dome, considering that the dome partly collapsed prompted by earthquakes at the beginning of the 1977 eruption.

For any quantitative discussion, it is desirable and important to know the magnitudes of these eruptions that may be estimated by the volumes of their effusive ejecta. Distributions of ash deposits from the three summit eruptions, in 1663, 1769 and 1822, are shown in Figure 3 by Katsui (1973) and volume of some recent eruptions are already published. Approximate ejecta volumes of historical pyroclastic flows and lava domes in Figure 3 are graphically calculated with some assumptions made by the present authors as shown in Table 1. As for the recent activity, the 1977 eruption issued 0.030 km^3 DRE in total (Katsui *et al*., 1978) and the 2000 eruption produced 0.0001 km^3 DRE (Geological map, 2007). During these 350 years, Usu volcano eruptions have occurred almost regularly in time, but their ejected volumes have been variable. In Table 1, allowing for some errors, the summit eruptions ejected larger volumes than the parasitic eruptions.

3. Some characteristics of the eruptions, mainly in the 20th century

Modern Japanese development of natural sciences documenting actually started in 1860's and the 20th century was a progressively advancing period; The 1853 eruption of Usu Volcano was not monitored scientifically, but the 1910 eruption was monitored in a greater detail, even if the scientists arrived at the locations after the outbreaks. The activities of this volcano are characterized by dacitic magmas with high viscosity.

It is difficult to obtain precursory information on future eruption activity of a volcano from its static images. Eruption activity of Usu Volcano can be obtained from summarization of its eruption activity. In this Section, the eruption activities in the 20th century shall be studied at two localities, its base and the summit. At the former, numerous small parasitic vents formed in the 1910 and the 2000 eruptions, and lava dome in the 1943 eruption occured. In the latter, only the 1977 eruption formed several vents and caused remarkable deformation of the summit. The latter is briefly referred in this section, but shall be discussed in detail in Section 5. The simplified distributions of the craterlets formed after the 1910 eruption is shown in Figure 4.

3.1 Precursory earthquakes of the eruptions in historical times

Precursory earthquakes of the Usu eruptions were counted by felt shocks in historical times and instrumentally observed after 1943. The leading manifestations of this volcano were usually explosive after precursory earthquakes of which duration usually ranged from 1 to 10 days, with one exception that lasted 6 months during the 1943 eruption: Deviation from 1 to 10 days may depend on magma paths from

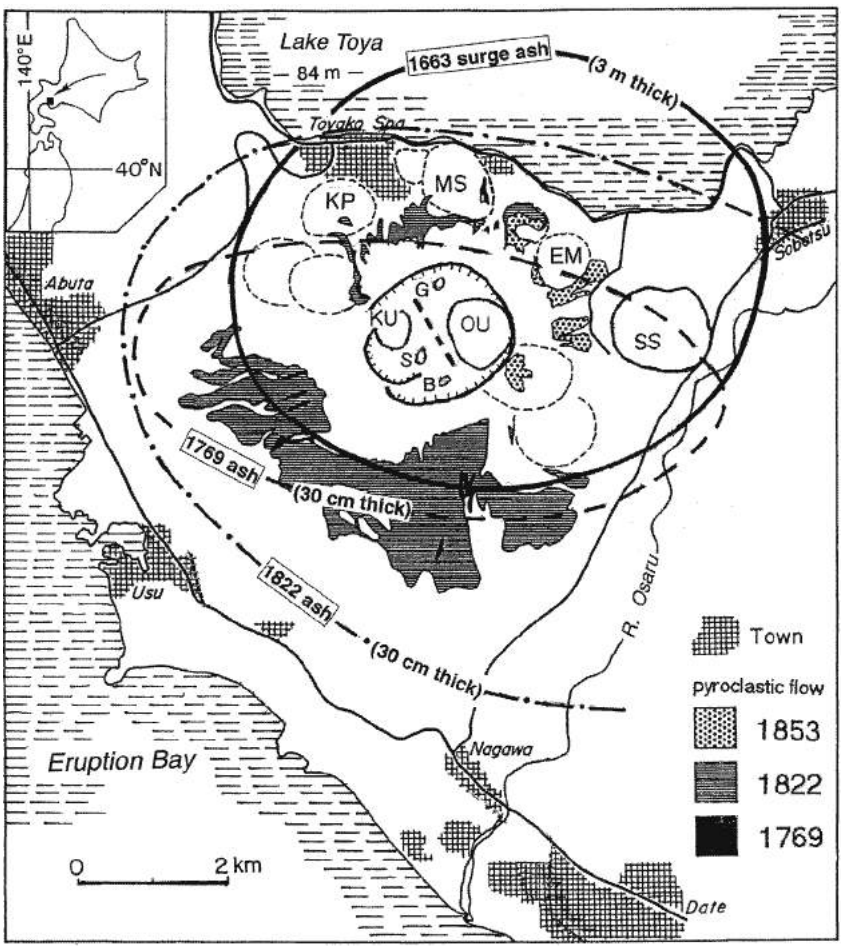

Figure 3. Distribution of pyroclastic ejecta from Usu Volcano copied and simplified from a geologicmap prepared by Katsui (1973). G, S and B in the summit crater denote the ponds, respectively.

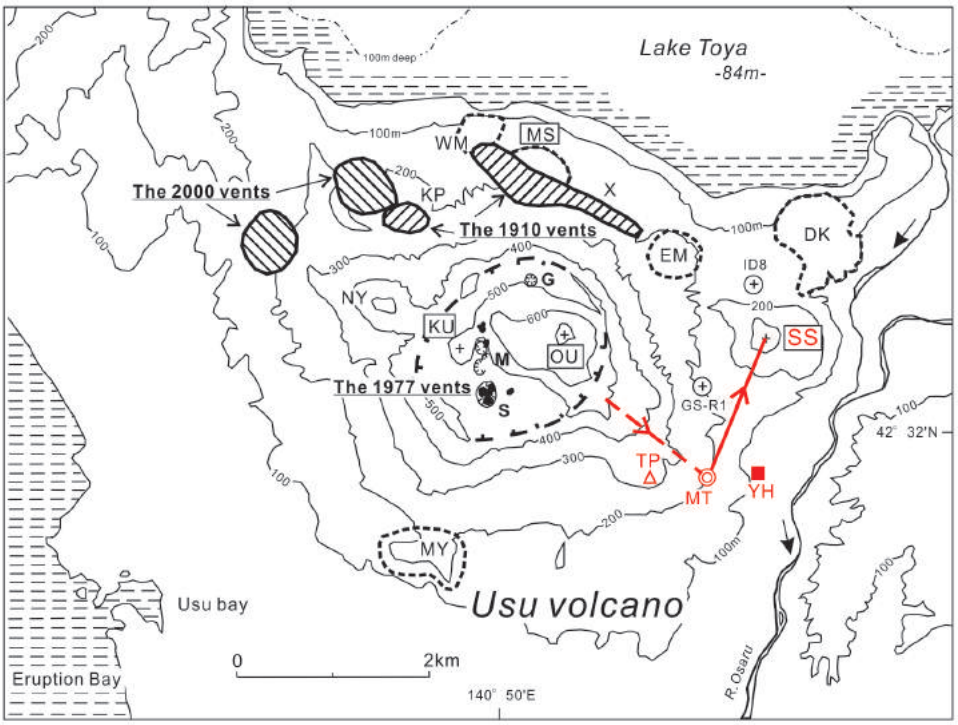

Figure 4. Domes, mounds, craterlets and parasites on Usu Volcano formed after 1910.
KU: the 1769 lava dome, OU: the 1853 lava dome, MS: Meiji-Shinzan (the 1910 mound), SS: Showa-Shinzan (the 1944 lava dome), WM: West maru-yama, KP: Kompira-yama, EM: Eastern maru-yama (lava and scoria, basalt and andesite), DK: Donkoro-yama (scoria, basalt), NY: Nishi-yama, MY: Minami-yama, ■YH: Yanagi-hara station, □TP: Triangulation point, ◎MT: Assumed location of magma top (its depth is about 1 km), ⊕: Drilling sites, M: main craterlets (Nos. 1,2 and 3, and I) , G: "Golden Pond", S: "Silver Pond".

reservoirs to vents. Magma movements during the 6 months before the outbreaks of the 1943 eruption shall be discussed in Subsection 3.2.

In Table 2, it is remarkable that the 1977 eruption had the shortest precursory period of 32 hours and the smallest magnitude of precursory earthquakes detected was M 3.7. These characteristics shall be discussed in Subsection 4.1.

3.2 Parasitic eruptions in the 20th century

Historical eruptions of Usu volcano are clearly distinguished as basal and summit eruptions. On Usu volcano, simultaneous eruptions at the base and the summit have never occurred and basal eruptions have been recorded only after 1910. The basal eruptions are necessarily parasitic.

Table 2. Precursory earthquakes observed in the historical times.

Eruption		Precursory period	Main type of activity	Hypocentral depths (km)	Maximum magnitude
1663	summit	3 days			
?	summit	?	?		
1769	summit	a few days ?	Ko-Usu (KU dome)		
1822	summit	3 days			
1853	summit	10 days	Oo-Usu (OU dome)		
1910	N base	6 days	phreatic, MS mound		5.1
1943	E base	6 months	Showa-Shinzan lava dome	1 ~ 4	5.0
1977	summit	32 hours	pumice eruption	0 ~ 5.5	3.7
2000	NW base	4 days	phreatic eruption	5 ~ 7	4.6

(a) The 1910 parasitic eruption at the northern base

The activities of the 1910 eruption were reported in detail by Omori (1911, 1913) and Satō (1910 1913 in the reference list!!!). Precursory earthquakes large enough to be felt persisted for 6 days. About 45 vents of small and large diameters opened in random order, roughly along the contour of 200 m a.s.l. at the N base of the volcano, as shown in Figure 5 (b); the distribution of the craterlets was originally described by Sato (1913) and the majority of those with small diameter have disappeared topographically years ago. The craterlets issued mudflows and a small quantity of lapilli and ash. Considering the random formation of small craterlets, we may assume a "tectonic structural line" (T.S.L.) for a series of the 1910 craters including Kompira-Yama (KP), East Mound and the 1943 lava dome (SS-dome) in Figure 5 (b). Moreover the 2000 eruption formed many craterlets around the 200 m contour at the NW slope or at the extension of the above T.S.L.

As will be discussed in Subsection 4.3, T.S.L. is the surface edge of the summit block which tilted as volcanic activity developed during the 1977 eruption. At the 1910 craterlets in the region of point X in Figure 5 (b), magma was fed along the vertical plane of T.S.L Such a manner of magma supply may have caused the random occurrence of parasitic eruptions along T.S.L.

In the 1910 eruption, a mound Meiji-Shinzan (MS) of relative height about 80 m was formed. Tanaka and Yokoyama (2013) studied the structure of MS mound (Figures 5 and 6). Hitherto this mountain has been called a "cryptodome" describing a lava dome covered by a domelike hill. Muography revealed that actually it is a mound that was lifted by magma intrusion and the magma top remains about 70 m below the surface. The magmas exploded in

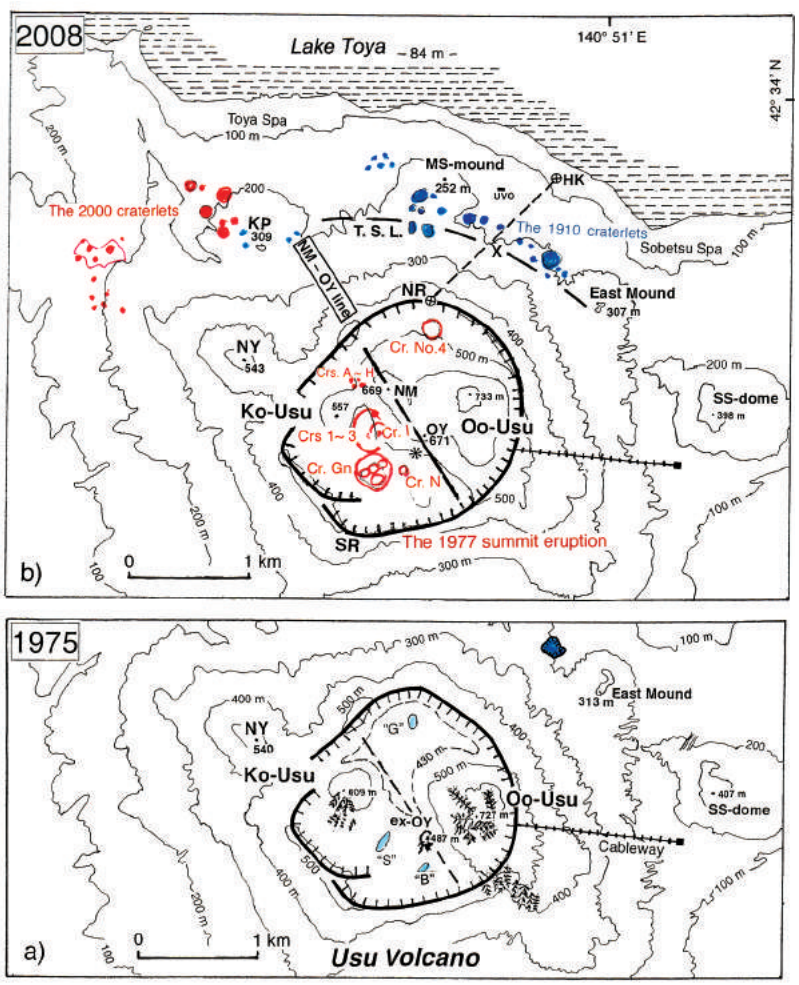

Figure 5. The volcanic features of Usu Volcano before and after the 1977 eruption. The topographic maps were surveyed in 2008 and 1975 respectively by the Geographic Survey Institute.
a) Summit part before the 1977 eruption. OY: Ogari-yama (a mound of unknown age).
b) Summit and base as of 2008, including volcanic structures formed in the 20th century.
NR – HK: GPS survey line, T.S.L. (tectonic structural line). Blue dots: the 1910 craterlets.
Red dots at the base: the 2000 craterlets.
Red colors in the summit crater: the craterlets formed in the 1977 eruption.
NR: north rim. SR: south rim. OY: Ogari-yama. NM: New Mountain. KP: Kompira-yama.
NY: Nishi-yama. SS: Showa-Shinzan lava dome formed in 1944. Asterisk: Site of a scarp shown in Photo 2.
NM –OY line corresponds to NM point in Figure 13.

the shallower parts forming three craterlets A, B and C at the surface as shown in Figure 6.

(b) The 1943 parasitic eruption at the eastern base:

The sequence of this eruption was reported by Minakami, Ishikawa and Yagi (1951) from synthetic application of geophysics and geology. Later Nemoto *et al*. (1957) studied the geothermal field on and around the lava dome applying multiple techniques.

Precursory earthquakes of the eruption began on Dec. 28, 1943. After 4 months, on May 1, upheaval of the railroad track at YH point (Figure 4) had reached 23 m at the maximum location within a distance of about 3 km (Inoue, 1948). The upheavals were surveyed along the railroad in the N-S direction but may have extended wider into the area covered with forests. The present authors suspect the center of upheaval may have been located a little W-ward from YH point in Figure 4. We newly found deformation of a triangulation point at about 1 km west (TP in Figure 4). This was 302.5 m a.s.l. in 1920 and 1932, and had changed to 316.8 m by a re-survey in 1955; namely this point had lifted about 15 m probably related with the 1943 activity. Now, we propose that the magma top may have been around MT point between YH and TP, or around the 200 m contour as shown in Figure 4.

Adopting the point-source model, the depth of the pressure source (or magma top) is approximately determined at about 1 km depth. In other words, viscous dacitic magma took 4 months to reach under the MT area from their origin, probably around 4 ~ 5 km b.s.l. Thereafter, the magma migrated N-ward and upward and reached SS point around June 1, 1944, with an apparent velocity of 1.5 km / month or 50 m/ day. On the other hand, in the period of dome upheaval near the ground surface discussed by Yokoyama (2002, Figure 2), its averaged velocity was about 1.8 m / day. Such considerable difference was surmised to be partly due to a remarkable increase of viscosity of the magma by cooling and dehydration even though their circumstances were rather different.

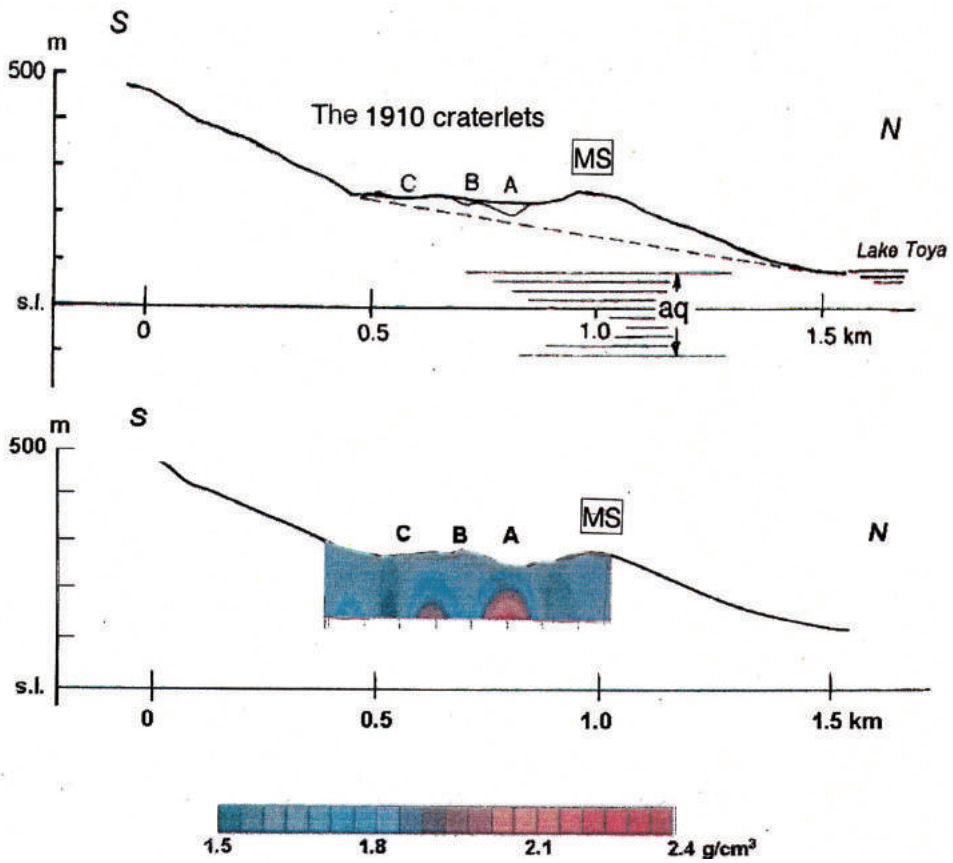

Figure 6. A muograph of Meiji-Shinzan (MS) mound after Tanaka and Yokoyama (2013).

Minakami *et al*. (1951) carried out seismological observation using mechanical seismometers at five points during the period June to September 1944. Volcanic earthquakes of A-type during July 1944 were located at the S slope of the volcano or at the NW of MT area (Figure 4) and the hypocenter depths ranged mainly between 3 to 5 km. Duration of the precursory earthquakes was exceptionally long, lasting 6 months (Table 2). SS lava dome is peculiar in being located at the base while the other lava domes such as Ko-Usu and Oo-Usu are in the summit area. The viscous dacitic magma may have developed a separate route.

Why did the magma change its course towards the N at MT? There may exist a caldera boundary or an extension of the tectonic structural line (an extension of T.S.L) to obstruct its E-ward migration. The magma may have followed the weakest route with least resistance. During the migration, the magma top ascended to about 200 m b.s.l. (Yokoyama, 2002, Figure 2). At SS point, the rising magma had lifted the ground surface and contacted the aquifer on June 23, 1944 causing the first explosion.

The dome finally reached a relative height of about 400 m, and grew laterally into an onion-shaped dome and completed its development as the Showa-Shinzan (SS) lava dome. Yokoyama (2002) discussed growth mechanism of the lava dome, and Tanaka and Yokoyama (2008) carried out a muographic survey and clarified the structure of the upper part of the lava dome.

(c) The 1977 parasitic eruption in the summit crater: This is a unique summit eruption in the 20th century. This eruption shall be discussed in Section 4.

(d) The 2000 eruption at the western base: Precursory earthquakes occurred for 4 days, similar to the 1910 eruption (6 days) and the magmas took the paths in similar structure, but in different directions. The eruption started on March 31 at the W foot of Nishi-yama (NY in Figure 4) around the 200 m (a.s.l.) contour and was magma-phreatic. The explosion column reached to about 3.2 km that was lower than that of the 1977 summit eruption (12 km). On the next day, new craterlets opened at Kompira-yama (KY) where a few craterlets of the 1910 eruption pre-existed. By the middle of April, the eruption had formed 65 small craterlets roughly on the extension of T.S.L. as shown in Figure 5b. At the W base of (NY), the central part finally had upheaved about 80 m by intrusion of magmas (Mori and Ui, 2000), as well as Meiji-Shinzan (MS). In Figure 5, a contour of 50 m upheaval is shown in red color. At the Kompira-yama (KP) area, it is not clear whether a few of the 2000 vents reoccupied the 1910 ones. At present, a precise determination of the 1910 vents on KP is difficult because the vents were very small and many of them have disappeared.

In contrast to main craters, parasitic ones usually don't repeat eruptions at the same vents probably because conduits of the latter are small in diameter and remain blocked with magmatic material of previous eruptions. However, if the previous conduits are not totally blocked, following magma-phreatic material may pass through the conduits and reach the previous vents to repeat the eruptions. If the previous conduits are totally blocked, usually parasitic eruptions must take alternate routes to reach the surface because their intrusive force and magnitude are not strong enough to overcome the barrier or blockage.

3.3 Topographies of the summit area in the early 20th century

During the documented history of this volcano, extending from the 17th to the 19th centuries, all the eruptions occurred at the summit. During the following century, only the 1977 eruption occurred at the summit. Here, topographies of the summit area in the early period of the 20th century shall be referred to.

On the Military Topographical Maps published in 1896 and 1910, three small depressions were clearly expressed as ponds within the summit crater, namely "Golden Pond", "Silver Pond" and "Brown Pond" and later, only "Silver Pond" in the S part remained as a pond and the other two remained as small dry basins on the maps. It is unfortunate that no historical record exists about their formation because they may have seemed so small in diameter and insignificant. Probably the first two vents may be twin parasites (Subsection 4.1) considering that their locations are symmetric around the center of this volcano even if they formed at different periods. Furthermore, as mentioned previously, the origins of the three pyroclastic flows have not been recorded. There may be some possibility that all or any of the three ponds were their origins.

Additionally, a Japanese pioneering geologist, Katō (1909) studied geology of Usu Volcano. His geological map of the summit area is reproduced in Figure 7. It was just 1 year before the 1910 eruption. In the figure, G ("Golden Pond"), S ("Silver Pond") and B

("Brown Pond") are the three depressions at the bottoms. This may suggest that both or either of the two ponds, G and S ponds were remains of the vents of pyroclastic ejecta in the 1822 eruption.

In all the geological maps after 1909 (Figure 7), there is no indication of a central crater within the summit crater. This may be interpreted as the central crater was originally located between Ko-Usu and Oo-Usu lava domes but was hidden by the domes and their ejecta and the main conduit may exist at some depth below.

In the 1977 eruption, "Golden Pond" erupted forming Craterlet No. 4 at the early stage, and later Craterlets J, K, L and M successively formed around "Silver Pond" and finally all merged to form Craterlet Gn (J ~ M) as shown in Figure 5 (b).

4. Activities of the 1977 summit eruption

The 1977 eruption was the first summit eruption after the 1853 eruption, and since then no other eruptive activity occurred. We are not aware of any scientific documents regarding observations of other summit eruptions for this volcano. Geological and geophysical research reports of the 1977 eruption were published shortly after the eruption by Katsui *et al*. (1978) and Niida *et al*. (1979 1980 in the reference list) and by Yokoyama *et al*. (1981) and Okada *et al*. (1981), respectively. In this paper, a brief summary of the eruption was prepared introducing some new interpretations based on geophysical considerations.

4.1 Sequence of the 1977 eruption

According to Katsui *et al*. (1980 1978 in the reference list), the 1977 activity is divided in two stages:

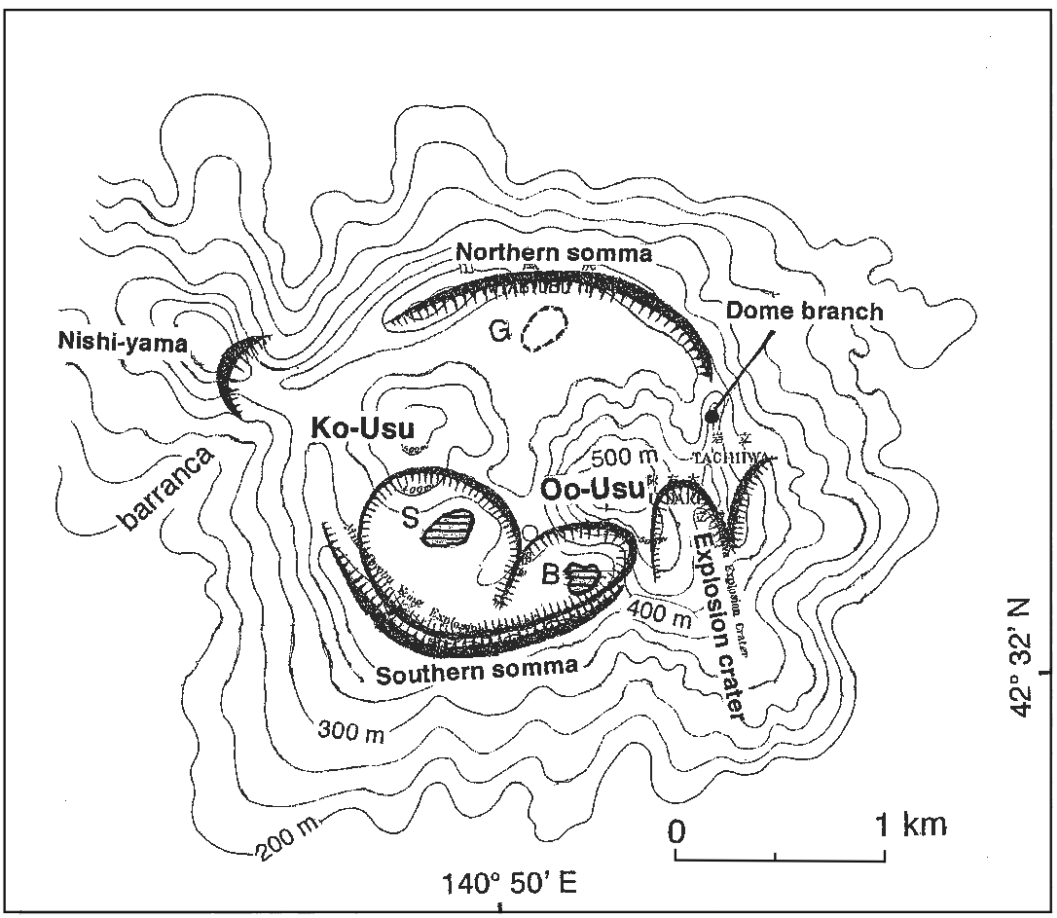

Figure 7. A geological sketch map of the summit crater of Usu Volcano before the 1910 eruption (Kato, 1909). Kato's "Explosion crater" indicates a depression containing two vents of S and B. In the present discussion, the two vents, G and S proved to be twin vents.

First Stage (sub-Plinian eruptions) (Aug. 7 ~ 14, 1977)
Craterlets Nos. 1, 2 and 3: pumice eruptions and explosion columns reaching about 12 km.
Craterlet No. 4: pumice eruptions (Aug. 9).

Second Stage (phreatic-phreatomagmatic-magmatic eruptions)
Substage I: Typical phreatic eruptions (Nov. 16, 1977 ~ Mar. 13. 1978)
Craterlets A ~ H,
Substage II: Phreatic to phreatomagmatic eruptions (Apr. 24 ~ June 28, 1978)
Craterlet I,
Substage III: Phreatic to phreatomagmatic eruptions (July 9 ~ Oct. 27, 1978)
Craterlets J ~ N; Craterlets J. K, L and M gradually merged into Craterlet "Silver Pond".

With relation to the above external activities, related seismic activity shall be summarized as follows. Precursory earthquakes of the 1977 eruption continued for about 32 hours and their hypocenters were located at 0 ~ 5 km b.s.l. Magma took 32 hours to reach vents at the surface from depths of roughly 4 ~ 5 km making a new path or along old conduits as indicated by the relatively small magnitudes of earthquakes (max. M 3.7).

During the period of the precursory earthquakes, the expected accompanying deformations of the summit area were not initially distinguishable, but soon upheavals of "Ogari -Yama" (OY in Figure 5) had become clear, and periodical theodolite surveys of point OY from the base point at about 8 km south were started on Aug. 15.

Figure 8 shows three kinds of activities: (1) daily release rates of seismic energy after Seino (1983), (2) eruption activity of each craterlet, and (3) upheaval rates of Ogari--Yama (OY). In the figure, all the three have the same time axes. Coinciding rates of seismic energy and upheaval of the central part of the summit crater indicates pressure induced by rising magma below the volcano.

At 01 h 06 m on Aug. 6 (JST), 1977 precursory earthquakes started. This stage is indicated by S_0 in Figure 8 - top. And at 09 h 12 m of Aug. 7, a violent summit eruption took place producing Craterlet No.1 at the eastern base of Ko-Usu lava dome. After the first eruptions (S_0), seismic energy decreased sharply for several days and recovered to Step S_1, and thereafter, decreased exponentially. At the end of January, 1978, both rates changed to an increase by a step (S_2 in the top of Figure 8) and, thereafter decreased exponentially. The next eruption activity resumed on Feb. 25, and continued to March 13, forming 6 craterlets (C, D, E, F, G and H). This development was fully discussed by Yokoyama *et al*. (1981).

According to Niida *et al*. (1980), the eruptions of Craterlets A to H were phreatic and their ejecta were almost entirely ash derived from pre-existing rocks. It is clear that magma intruded at Step S_2 and probably, the magma may have been more viscous than the earlier one and reached near the bottom of the volcano on Apr. 24, when Craterlet I began its activity: Before Step S_3 , six craterlets C ~ H were successively formed but they were not magmatic. They may have been activated by energy from the magma of Step S_1 . The magma of the Step S_2 may have been more viscous than Step S_1 and needed more time to reach the vent possibly because the magma had lost its H_2O component. The magmas needed about 75 days to rise to an explosion depth, namely ($S_2 \rightarrow S_3$) as shown in Figure 8. Craterlet I erupted amid the three craterlets, Nos. 1, 2 and 3, and its magmatic activity lasted about 2 months from Apr. 24 to June 28, 1978, and later only fumarolic activity continued with strong emission with high temperature gases until 1982. Craterlet I may have been energized by similar mechanisms as those of Craterlets Nos. 1, 2 and 3.

Judging from the sequence of the three activities shown in Figure 8, the largest amount of magmatic material and energy was afforded from the depths by the first outbreaks.

Singularity of the eruptions of Craterlet No. 4: As mentioned above, Craterlet No. 4 was formed at "Golden Pond", about 1 km NE from Ko-Usu lava dome, on the 3rd day following the outbreak. A major pumice eruption lasted 3 hours forming a crater of about 100 m across. The pumice and ash were scattered to the E of the volcano. The site of the "Golden Pond" was dry in 1909 and 1975 (Figures 7 and 5 (a), respectively). Its origin is not documented, and probably may be pre-historic. Photo. 1 shows Craterlet No.4 immediately after its formation: the first opening of this craterlet was cylindrical, not funnel shape. It was about 100 m across and about 50 m deep. The uppermost white layer was the new ejecta of pumice and ashes. Leaves of the trees dropped but trunks were not damaged; explosivity was not so high and was directed vertically. In short, the eruption of Craterlet No. 4 was rather simple and readily ejected pumice and ash without expanding its crater. This may due to access through a previously formed conduit. A few months later, the surface circumference collapsed to form a funnel-shaped craterlet.

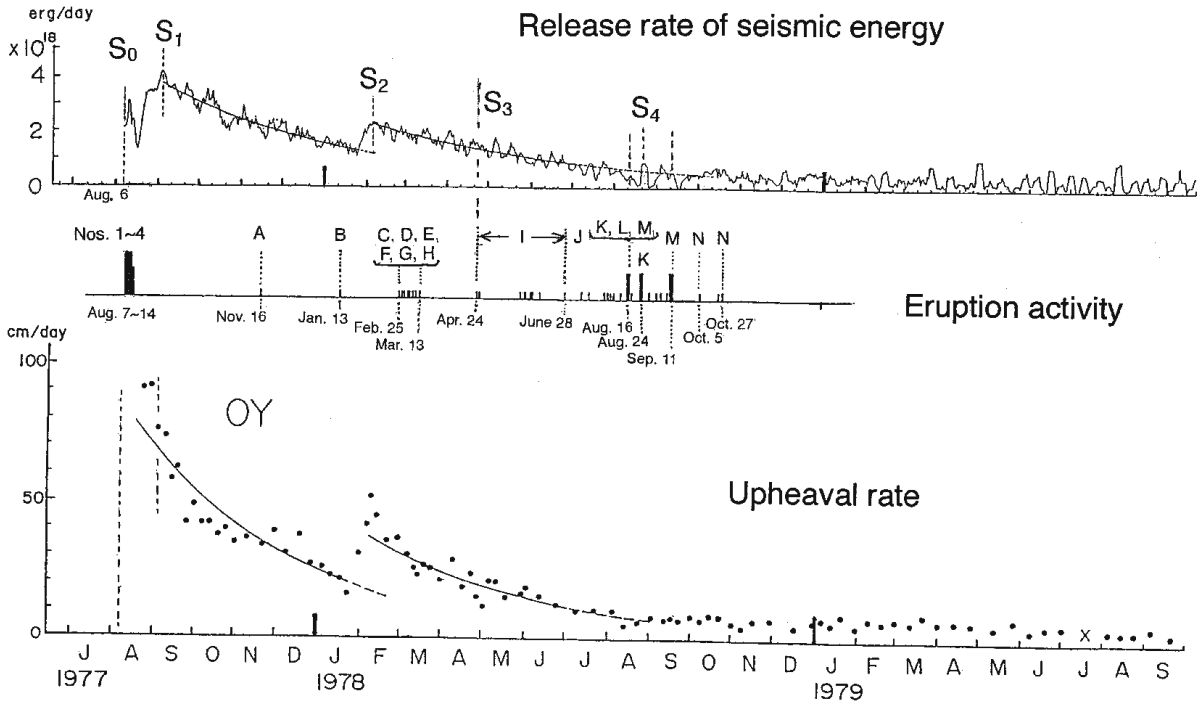

Figure 8. (top) Release rate of seismic energy (after Seino, 1983), (middle) Eruption activity (mainly after Niida *et al*., 1980), Nos. 1 - 4, and A ~ N are signs of the craterlets, (bottom) Upheaval rate of Ogari-yama (OY in Figure 5).

Twin parasitic vents in the summit crater: As referred above, "Golden Pond" erupted in August, 1977, and "Silver Pond" erupted in September, 1978. Here it is assumed that these two vents were twin parasitic vents formed by a dilatational source acting from the middle of the two vents. This upward pressure source serves an important role in the tilt movement of the summit region as shall be discussed in Subsection 4.3 with Figure 13.

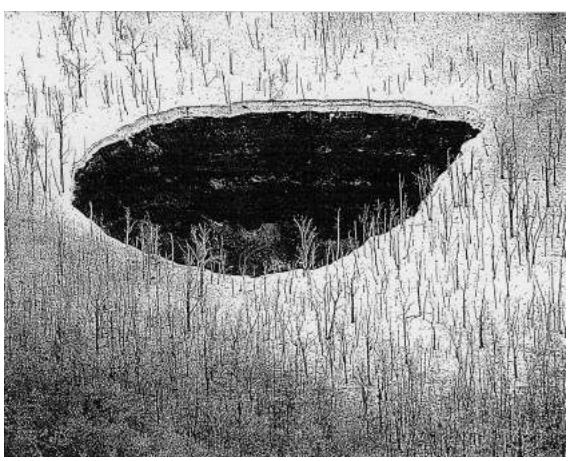

Photo 1. Craterlet No. 4 immediately after the formation on Aug. 9, 1977. (Hokkaido Shimbun Press).

Shear fracture model for formation of twin vents by a dilatational source: This was already discussed by Yokoyama (2015) and shall be briefly summarized in the following:

As a volcano becomes active, magmatic pressure is exerted towards the pre-existing main crater through the main conduit, and if the pressure overcomes the yielding strength of cap-rocks at its crater, an explosion should be triggered; this is usual in polygenetic volcanoes and interpretable by the maximum stress theory. Many volcanoes may have a complex of sills and dikes formed in past activities. New magma invading the volcano complex may utilize these sills and dikes for their new conduits leading to vent. In the following section, formation of parasitic vents in homogeneous volcanic bodies is discussed by applying the criteria of fracture mechanics, specifically the maximum shear stress theory. At a certain point under the flat surface of a volcano, both pressure and shear stresses exert on the structure. If either of them reach the yielding strength, the corresponding part of the volcano should fracture. Usually shearing strength of rocks is much less than the compressive one. In Figure 9 (a), the plane polar coordinates (r,θ) at the surface are adopted and the effects of shear stress due to a dilatational source P_0 are considered : the

maximum shear stress is equal to half of the horizontal differential stress and is expressed as:

$$1/2(\sigma_{\rho\rho} - \sigma_{\theta\theta}) \qquad (1)$$

where σ_{rr} and $\sigma_{\theta\theta}$ denote the principal stresses. The maximum shear stress occurs across a plane whose normal bisects the angle between the greatest and least principal stresses.

After some calculations, the value of term (1), positive or negative maximum, was obtained

$$r = \pm 0.82\, D, \text{ or } D = 1.22\, r \qquad (2)$$

In other words, the medium undergoes the maximum horizontal differential stress at a radial distance r = ± 0.82 D, or where the dip angle of the pressure source from the fracture point at the surface is 51°. Consequently shear fracture develops there, in the radial direction on the surface or along the slope. Theoretically the maximum horizontal differential stress is expected to be present at two points, r = ± 0.82 D, or on symmetrical sides of volcanoes. In the actual volcanic fields, the media are not always uniform, and so any weaker point ruptures first eliminating any further rupturing to occur.

Anderson (1936) discussed the dynamics of the formation of cone-sheets caused by point dilatation and showed opening fractures (solid lines) and isostatic surfaces (broken lines) in Figure 9 (b). The twin parasitic fractures S_1 and S_2 are added to the figure by the present authors.

On the actual volcanoes, the shear fracture model may be useful when the volcano is still young and remains uniform in structure.

Yokoyama (2015) mentions several examples of twin parasitic vents on volcanoes of the world. Their origins were not always documented and one or both of them sometimes would be omitted from the maps after substantial time because they are usually not so large in diameter.

Considering the past volcanic activities of Usu Volcano, the shear fracture model shall not be strictly applicable to future formation of twin parasites on this volcano because the volcano is not homogeneous any longer. Magma may supply preexisting sills and dikes to form a new conduit and vents.

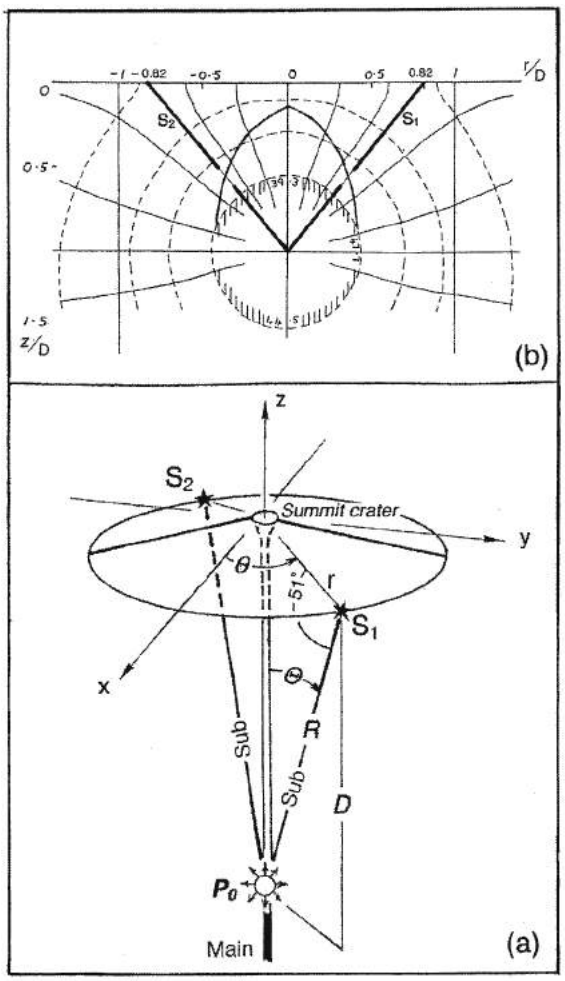

Figure 9. Shear fracture model: (a) Point dilatational model, (b) Isostatic surfaces (broken lines) produced by point dilatation after Anderson (1936).

4.2 Deformations in and around summit crater

a) Ko-Usu lava dome: It was formed in 1769 and had 608.8 m a.s.l. before the 1977 eruption. The dome began to subside as a whole, simultaneously with the pumice eruptions of Craterlets Nos. 1, 2 and 3, accumulating at the E base of this lava dome. Finally the height reached 557 m, about 50 m drop in about 3 days from Aug. 7 to 9, and it was clearly visible by naked eye. No one expected such subsidence of the dome, and so no instrumental surveys were conducted. Pumice explosions at Craterlets Nos. 1, 2 and 3 probably may have dug the base beneath the lava dome, or the conduit of the lava dome was, in part, common with those of the new craterlets. The 1977 eruption started after 32 hours of precursory earthquakes, and the maximum

magnitude of the earthquakes was M 3.7, both quantities were minimal relative to other historical eruptions. The present authors suspect that the magma passed through some preexisting cracks of the conduit of Ko-Usu lava dome and reached the surface in a short time with minimal resistance.

b) Oo-Usu lava dome: It was formed in the 1853 eruption. Before the 1977 eruption, the main peak was 727 m a.s.l. and a dome branch ("Tate-iwa" or obelisk) separated at the northern side was about 650 m a.s.l. (Figure 4 and Figure 5a). In the early period of the 1977 eruption, a branch of the dome collapsed by earthquake movements or tilting of the summit area. Frequent earthquakes occurring directly beneath the dome partly destroyed it (cf. Figure 5), and its height decreased while the area of Oo-Usu dome was upheaved by tilting of the summit block. Finally, the height decreased to about 670 m a.s.l. and the highest peak apparently shifted northward about 400m and attained a height of 733 m (a.s.l.). As shall be discussed later (cf. Subsection 4.3), a summit block bounded a line from Oo-Usu toward N 30° W tilted gradually since the outbreak of the eruption. Such deformation caused upheavals of Oo-Usu dome as a whole. In a short time, Oo-Usu lava dome had been altered from upheavals and collapses. This suggests that the upward magmatic force acted under NM-OY line (Figures 5b and 13) accompanied by relatively large earthquakes (M 4). This shall be discussed later (Subsection 4.4).

c) Horizontal displacements: The summit crater of the volcano deformed according to the progress of volcanic activity. The Geographic Survey Institute of Japan had carried out photogrammetric surveys over the summit crater three times after the starting of the 1977 eruption: The results are shown in Figure 11 where the S half of the crater rim has not deformed. OY denotes a mound formed in the 1769 eruption and its relative height was about 10 m as for 1976. A curved line connecting OY and the base of Ko-Usu lava dome had displaced about 250 m and NR-point of the northern rim about 130 m, both NE-ward during 2 years and 3 months after the beginning of the 1977 eruption. This pattern of the horizontal deformation indicates that the summit block displaced toward the NE, and the SW rim (SR) of the caldera had not deformed probably because crater deposits are explosion ejecta, and are soft and not elastic.

d) Upheaval or tilt movement of the summit block: The 1977 eruption began on August 7 and after a few days, Ogari-yama (ex-OY in Figure 5a) was noticed to have been rising daily. Routine theodolite-observations of the target OY commenced in the middle of August 1977 and its upheaval rates are shown in Figure 8. Later, point NM (new mountain) was installed as another target.

Harada *et al*. (1979) installed an EDM measuring line between the N rim (NR) and the base station (HK) near the lake as shown in Figure 5. According to them, the line had shortened about 100 m during 1 year after September 1977. Complementing the above measurements, Maekawa and Watanabe (1981, Figure 3) monitored the N-ward displacement

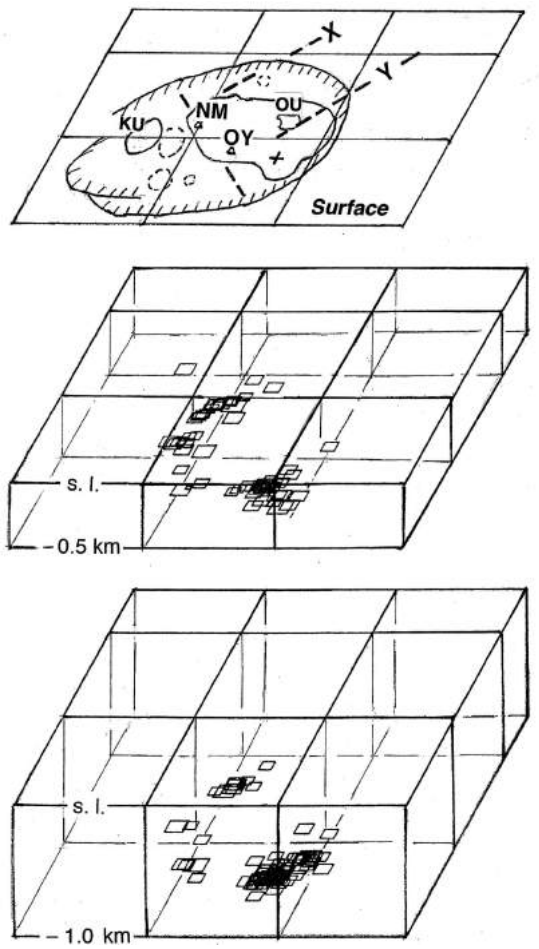

Figure 10. Hypocenter distribution of magnitude M 3.8 ~ 4.3 during October 1977 ~ July 1979 classified according to depths. At the deeper depths, earthquakes are of smaller magnitude. The surface shows the topographies from 1982.

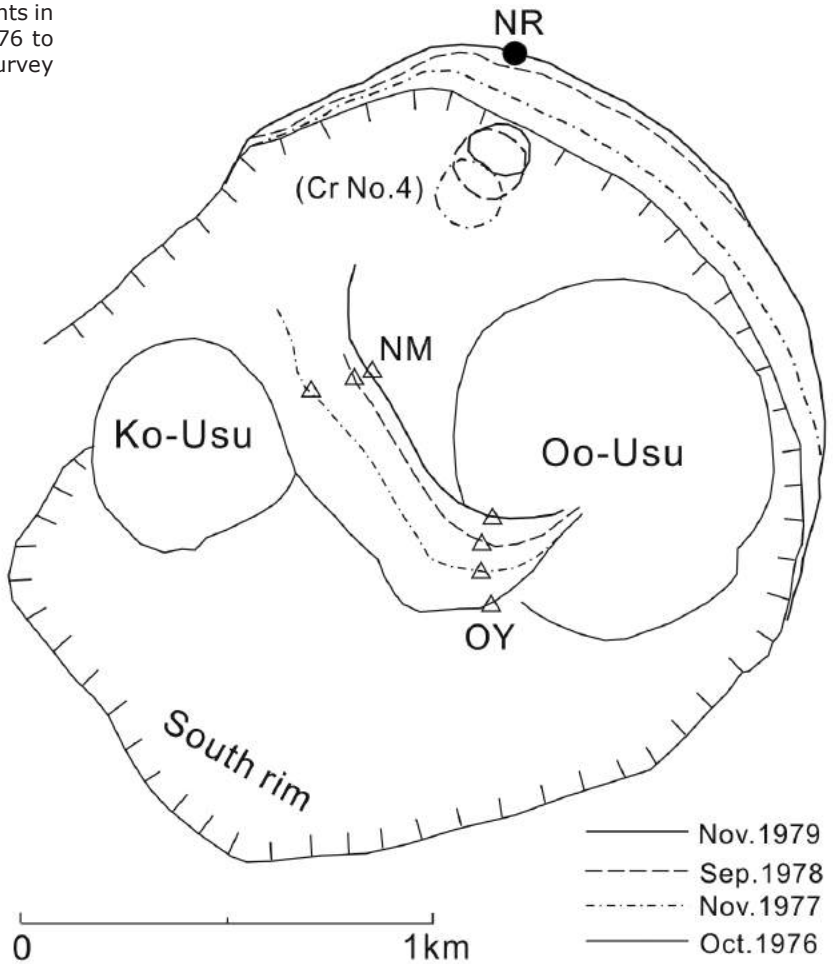

Figure 11. Horizontal displacements in the summit crater during Oct. 1976 to Nov. 1978 (after Geographical Survey Institute).

of the caldera wall, along the line NR – HK. The results are shown in Figure 12 where there is a stationary point (X in Figure 12) in the displacement. For 11 months from July 1980 to May 1981, NR point on the northern rim had displaced about 1.3 m towards the NE in reference to the base station HK while point X and the lower point (UVO) displaced very little and discontinuously.

These results mean that point X is located at the boundary line between the movable summit part and the fixed base. The boundary line is the tectonic structural line (T.S.L.). It is remarkable that the 1910 eruption formed many craterlets roughly along T.S.L. The ground at the lake side of T.S.L. had remained stationary while the Usu summit side had tilted. The block movement of the summit part shall be discussed in Subsection 5.3.

A summit block containing NM – OY line in Figure 5 started to rise simultaneously with the eruptive activity. The driving force was believed to be magmatic pressure that caused the summit block to tilt. The block sheared along NM – OY line . A hypothetical profile of the summit block is shown in Figure 13.

4.3 Block movements of the summit part

Deformations of the summit part of Usu Volcano observed during the 1977~1982 activity suggest block movements. A working hypothesis to interpret the block movements is proposed. To prove validity of the model, the block movements will be correlared with fault movements at the block boundary. Yokoyama and Seino (2000) presented a hypothesis that the summit part extending from Craterlet No. 4 to the tectonic structural line (ab. T.S.L.) at the N base and to the bottom of 500 m (b.s.l.) tilted accordingly as volcanic activity developed. In the present discussion, the previous model is improved. On Figure 5 (b), NM-OY line apparently moved toward the NE, but actually the summit block tilted as shown in Figure 13 where the tilting axes of the three

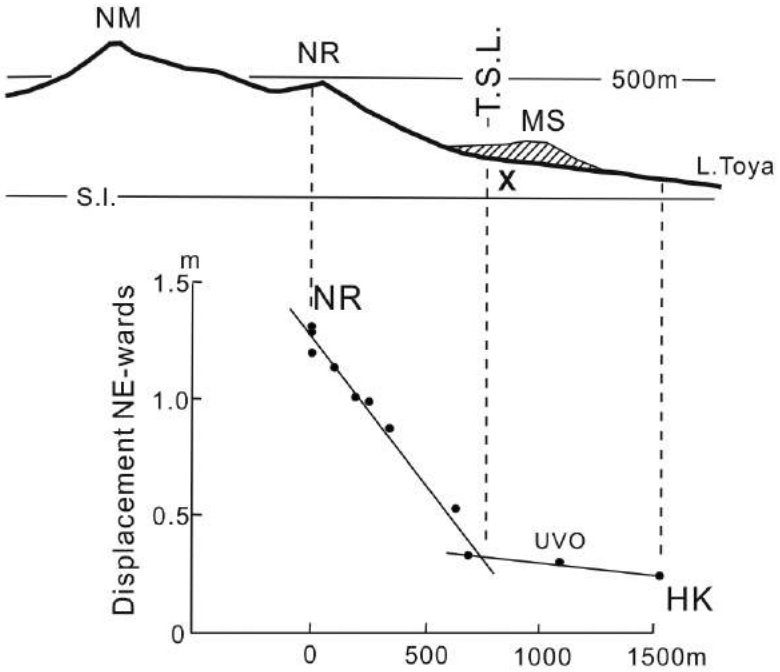

Figure 12. Distance measurements between the northern slope of the volcano and the base point (NR – X – HK in Fig. 5(b)) for the period July 1980 to May 1981. MS: the 1910 mound shown in Figure 4. Point X is the hinge-line of both parts.

points, NM, Craterlet No.4 and NR, converge approximately at P point at a depth of about 1.5 km b.s.l. Thus, the block is determined to be larger than in the previous model. In Figure 11, the N part of Ko-Usu and OY line had moved NE-ward while the SW part did not move. Their tilt angles amounted to 8, 8 and 5 degrees, respectively. The last one may have resulted from resistance, because the N ground is relatively immobile at T.S.L Thus it is presumed that the ground remained fixed at a depth of P point (1.5 km b.s.l.). The NR-SR profile of the summit part of the volcano is shown in Figure 13 where NM-OY line in Figure 5 (b) and NR (the N rim) in Figure 11, shifted NE-ward or actually tilted about 8 degrees around the common pivotal point P which is assumed to be located at 1.5 km b.s.l. This trial model is very approximate.

According to the shear fracture model, the branch of the conduit leading to Craterlet No. 4 should be located at about 0.5 km b.s.l. in Figure 13. A substantially strong force N acted at point Q to tilt the block Q-Cr-X-P around pivotal point P. In Figure 13, the 1910 eruption started along the tectonic structural line (T.S.L.), and its magma conduit may have been derived from a deeper source below point Q (cf. Figure 15).

The upper surface of the block can be defined, but deep structure is uncertain and may be shallower or deeper around the pivotal point. The rotational movement is defined in Figure 13, which shows deformation of the NE-ward profiles observed during the period from Oct. 1976 (before the eruption) to Nov. 1980. At some particular points such as the main craterlets (Cr), Craterlet No. 4 and NR (the N rim), their rotation angles around pivotal point P were estimated. As shown in Figure 13, the first two rotated about 8 degrees and the last one about 5 degrees: The last (NR) was at the edge of the summit block and could not deform further. Additionally, the summit block may have tilted about 8 degrees around pivotal point P.

The crater deposits between the S crater rim (SR) and Cr – Q line (in Figure 13) may be soft and inelastic as previously referred in the horizontal deformation of the summit part (Figure 11) and thus did not present any detectable deformation. The depth or configuration of the crater deposits is uncertain but assumed to be at the level of Q point at a depth of 1.5 km b.s.l. Thus Cr – Q line may have deformed by upward pressure N acting at point Q.

Rotational kinetic energy and earthquake occurrence:

The dynamics of the summit block shall be interpreted from mechanical movements. It is assumed that the summit block repeats rotational and upheaval movement stepwise around the pivotal point. Here angular velocity, moment of inertia and force are denoted as ω, I and N, respectively. The following relationships were then used:

$$N = I\frac{d\omega}{dt} \quad (3)$$

and

$$I = M \bullet r^2 \quad (4)$$

where M and r denote mass of the block and lever length between pivot P and the center of gravity G of the block, respectively. In the following, configuration of the block and the above factors cannot definitely be determined and shall be estimated within an order of magnitude on Figures 5 and 13: the side length is roughly equal to NM – OY line , about 1.5 km, and the depth probably range from the surface of the summit (about 0.5 km a.s.l,) to the level of 1.5 km b.s.l. as indicated by volcanic earthquakes that occurred above this depth (cf. Figure 10).

In the present case, pivot P is assumed to be located roughly at the same level as the bottom. Thus the summit block is determined to be cubic, having the side [Cr – X – P – Q] in Figure 13 and its volume is roughly estimated at 8 km^3. Its mass (M) is estimated at 2 × 10^{13} kg, assuming a density for the summit part of 2.5 × 10^3 kg / m^3. In this case, the lever length r is equal to the distance between the pivot and the center of gravity (G) of the block, which is about 1.4 km. Subsequently, the rotational kinetic energy K is given as

$$K = 1/2 \bullet I\omega^2. \quad (5)$$

In this case, angular velocity ω is evaluated by streaks on the upheaval boundary indicated by earthquake faulting exposed at the surface and duration times of the upheavals. The former is indicated by a photo of the streaks (Photo. 2), and the latter is estimated by seismograms registered by upheaval movements. Photo. 2 was taken by T. Maekawa and H. Watanabe (pers. com.) on Sep. 12, 1978 at a scarp marked by an asterisk at the S of OY in Figure 5b. During this period, the block uplifted stepwise 2.5, 3.5 and 5 cm, all being accompanied by relatively large earthquakes of M 3 ~ 4, located at levels of – 0.5 and – 1.0 km below mark (+) on the surface in Figure 10. Though their occurrence times are not exactly

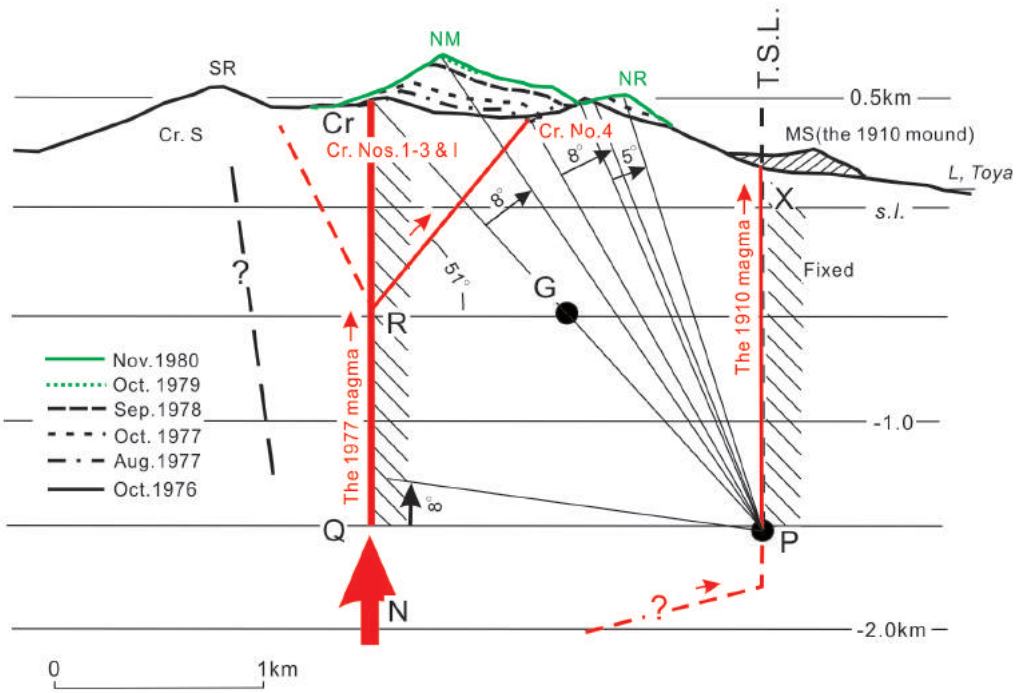

Figure 13. Schematic figure of tilting of the summit block. A vertical profile of Usu Volcano in the NE direction, in Figure 5.
G: Center of gravity of the summit block (Cr – X – P – Q),
NM: New mountain, NR: North rim, MS: Meiji-Shinzan (a new mound formed in 1910),
T.S.L. or X – P line: Tectonic structural line, P: Pivotal center of the rotation,
Q : Assumed magma front pressing the summit block in 1976 ~ 1982,
R : Branch point of magma conduits for Craterlet No. 4 ("Golden Pond") and Craterlet S ("Silver Pond") determined by the shear-fracture model,
Cr: Site of Craterlets group Nos. 1 ~ 3 and I. Cr point moved to NM during Aug. 1977 to Nov. 1980.
Cr. S: Craterlet "Silver" composed of craterlets. J, K, L and M, not on the same plane as Cr. No. 4.

known, reference to the seismograms observed at approximately similar periods are made. Mizukoshi and Moriya (1980) observed volcanic earthquakes from December, 1977, to October, 1978, by accelerographs and displacement seismographs of low magnification at the Usu Volcano Observatory (UVO in Figurfe 5b). The three displacement seismograms indicated the block movement occurring from the S base of Oo-Usu lava dome (+ mark in Figure 10) shown in Figure 14.

The authors interpret that NM – OY line in Figure 5b formed by an upheaval of a summit part and the upheaving boundary is at a surface earthquake fault, and a slip plane (a kind of slickensides) produced by upheavals of one-sided land block. Probably in the case of formation of Showa-Shinzan (SS) lava dome in 1943 may have produced similar slip planes under the ground surface, even though they were not found. In case of Showa-Shinzan, solidified magmas continuously upheaved causing slickensides while in case of NM – OY line, magmas upheaved stepwise causing fault-like traces.

In Figure 14, the rise-time is defined as the time needed for a certain place on the fault plane to displace from the beginning to the end. The rise-times derived from the seismograms shown in Figure 14 and are about 1 sec. in average. Then, angular velocity ω is estimated as 0.03 m / 3 km / 1 sec.

Thus rotational kinetic energy K is calculated as:

$$K = 1/2 \bullet Mr^2 \omega^2 = 2 \text{ x } 10^9 \text{ Joule} \quad (6)$$

A part of the kinetic energy can be attributed to the occurrence of earthquakes of magnitude 3 which discharge kinetic energy of 2×10^9 Joule. In the above calculation, the energy necessary to overcome frictional resistance is not considered during the movements. If this effect is considered, the related earthquakes of magnitude M 3 ~ 4 can be explained. By the above calculations, it is proved that kinetic energy necessary to tilt the summit part is just enough to cause the seismic movements observed at an edge of the block.

Eruption mechanism of Usu Volcano determined from the observations in the 20th century

Eruption activity of Usu Volcano discussed in Sections 3 and 4 should afford an inductive model of its eruption system even though it may be revised with further analyses.

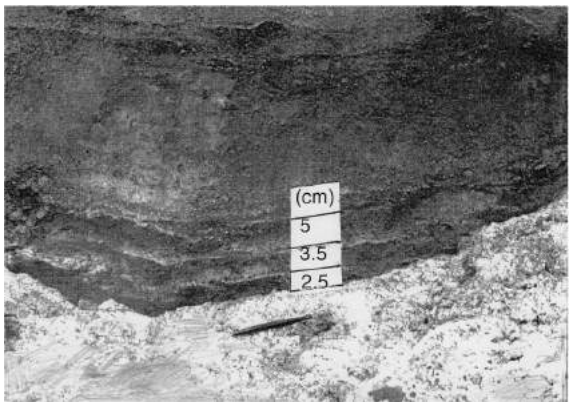

Photo 2. A fault scarp as of Sep. 12, 1982. The location is shown by an asterisk in Figure 5b. This side is covered with sublimates and a ball pen is a scale.

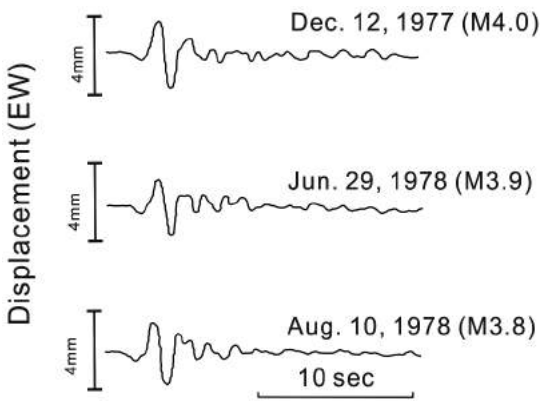

Figure 14. Seismogram-samples of earthquake family having large amplitude, mostly located at the southern base of Oo-Usu lava dome (+ mark in Figure 10 top) (The traces are taken from Mizukoshi and Moriya, 1979 1980 in the reference list).

Originally, the main vent was thought to be roughly at the center of the summit crater, measuring about 2 km in diameter, and the vent was suspected to be blocked with Oo-Usu and Ko-Usu lava domes. At the beginning of the 1977 eruption, magmas may have ascended through the main conduit and erupted beside Ko-Usu dome, forming the three craterlets. Also, magma channeled through the main conduit caused eruptions of the twin parasitic vents, "Golden Pond" and "Silver Pond" in pre-historic times. The magma pressure from the conduit system presumably caused tilting of the summit block. Magma intrusion at the upper part of the main conduit was verified by the electrical resistivity surveys (cf. 5.3). The first three eruptions may have partly deviated from the main conduit, and passed beneath

the old conduit to Ko-Usu lava dome because the dome subsided about 50 m simultaneously with the early eruptions. The central conduit may have been active in supplying magmatic material to parasitic eruptions.

Magma supply systems of Usu Volcano that functioned in historical times are schematically shown in Figure 15 in the SW – NE cross-section. In a previous study, De la Cruz-Reyna and Yokoyama (2011, Figure 11) brought up the parasitic vents of Usu using a fracture criterion for brittle materials. Here, the present authors include the block movements and local structure of the NE sector of the volcano in Figure 15. We assume that Ko-Usu, Oo-Usu and SS-lava domes formed in 1769, 1853 and 1944, respectively, may have developed directly from the magma reservoir because supply of the juvenile dacitic magmas may need special conditions. On the other hand, parasitic eruptions, such as the 1910 and the 2000 eruptions, may have been fed through branches from the main central conduit. In Figure 15, only the path of the 1910 eruption along a lateral side of the tilting block and T.S.L is indicated; the 2000 eruption took other paths that branched from the central conduit. Such idea may develop to an assumption that magma-supply routes are related to local melting condition at starting point from the reservoir or that a magma reservoir is not always uniform in melting condition.

In the future, the above suppositions should be revised with more advanced studies of geophysics and petrography.

5. Subsurface structure of Usu volcano

Knowledge of the subsurface structure of an active volcano is usually the result of multiple observations, from monitoring data during periods of activity and from exploration methods during quiescence periods.

To further understand volcanic eruptions, it is essential to explore the detailed subsurface structure of the volcano. The research directions and methods should vary with magma types, history of the eruptions and the present knowledge of the structure. One of the actual ultimate purposes on studying the subsurface structure of Usu Volcano is defining the parameters of its magma reservoir, such as its location, structure and action mechanisms. Data bases covering extended periods of time are essential for understanding the long-term changes in volcanic structure and behavior.

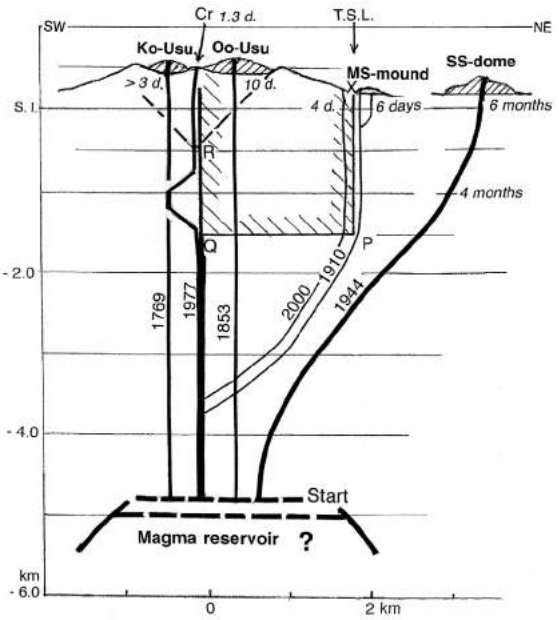

Figure 15. An assumptive and schematic model of eruption system of Usu Volcano, projected on the SW-NE direction. Days and months denote precursory times before the outbursts. Cr denotes the positions of Craterlets Nos. 1, 2 and 3 of the 1977 eruption. T. S. L. denotes a tectonic structural line appeared in the 1910 eruption at the eastern foot of the volcano. This figure overlaps partly with Figure 13.

5.1 Seismic structure

Real-time acquisition and precise analyses of seismic data are most important processes to interpret the dynamic state of the volcano. At the time of the 1977 eruption of Usu Volcano, a new volcano observatory was just under construction. Okada *et al*. (1981) located the hypocenters of the volcanic earthquakes as mentioned in Subsection 4.2 and proved that some relatively large earthquakes were related with tilt movements of the summit block.

During the 2000 eruption of Usu Volcano, Onizawa *et al*. (2002) studied three-dimensional P- and S-wave velocity structure around the volcano using traveltime data of the volcanic earthquakes. After the eruption, Onizawa *et al*. (2007) studied the three-dimensional P-wave velocity structure beneath the volcano using 288 temporary seismic stations and seven programmed dynamite-explosions. The velocity structure down to the Pre-Neogene basement below the volcano or to a depth of about 3 km was revealed and low-velocity (1.5 ~ 2 km / s) area at depths 3 ~ 4 km was found. The most prominent feature of the velocity model was the deepening of the basement toward the

S-SW. This feature agrees with decrease of the gravity anomaly toward the S, at the S of the volcano as shown in Figure 2.

Accurately determined velocity structure is necessary to precisely locate hypocenters of volcanic earthquakes, and permitted the relocation of the precursory earthquakes of the 2000 eruption by Onizawa *et al*. (2007), as shown in Figure 16. The seismic activity was then divided into three patterns: (1) a quasi-vertical distribution indicating magma ascent toward the summit, (2) a N-ward distribution indicating the subsequent eruptions at the NW base, and (3) S-ward distribution indicating S-ward intrusion of sills. The present authors notice that the last pattern (3), indicates possibility of parasitic eruptions at the S base. Additionally there is Minami-Yama (MY) mound of unknown age on the topographic maps (Figure 4).

5.2 Aquifer structure beneath Usu Volcano

Aquifer structure beneath and around any volcano fundamentally affects magmatic activity. Usu Volcano is located between Lake Tōya (83 m a.s.l.) and Eruption Bay (Figure 4). In general, underground water flows from the lake towards the sea smoothly even if there

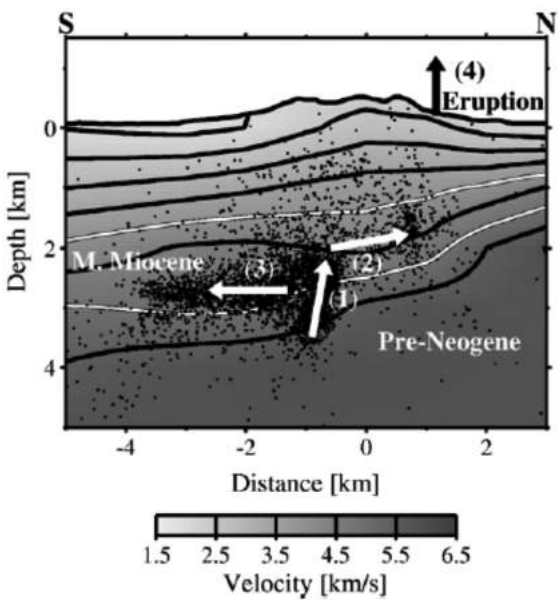

Figure 16. Earthquake hypocenters during the precursory stage of the 2000 eruption and the sequence of the possible magma movements projected on the N–S velocity cross-section after Onizawa *et al*. (2007, Figure 14). The dots represent the hypocenters during the precursory stage, and two white lines denote the boundaries of geological strata. The arrows indicate direction of the magma movements.

are temporal rises of the water level due to volcanic activity. In fact, coinciding with the 1977 eruption of Usu Volcano, the water level at GS-R1 well (Figure 4) at the E base rose 37 m and then recovered after about 4 years. Watanabe (1983) interpreted these changes as a result of increased pore pressure diffusion beneath the summit crater. Such changes in water level are relatively small in comparison with the volcano height, of about 600 m, and similar changes were not reported in the case of the 2000 eruption. Also, the flow rates may not be high because the gradient of the flows is roughly 83 m / 7 km. Thus, the aquifer beneath Usu Volcano may be almost flat, flowing from 83 m (a.s.l.) to the sea. Ascending magmas should first contact the Quaternary aquifers which are located at the upper boundary of Neogene period layers, as shall be discussed in the next subsection.

5.3 Electrical-resistivity structure of Usu Volcano

Underground structure of Usu Volcano was investigated using magnetotelluric soundings (Ogawa *et al*., 1998; Matsushima *et al*., 2001). A characteristic structure of the edifice is a thick low resistive layer (<10 Ωm) located from sea level to 2 km b. s. l. (Figure 17). This low resistive layer is thought to contain highly altered rocks produced in the Neogene period. The base line (point Q and point P in Figure 13) of the block tilt model proposed in the present paper corresponds to the lower boundary of the low resistive layer. At this boundary, the physical property changes among the different formations. The earthquakes associated with the 2000 eruption of Usu Volcano showed a unique distribution which spreads horizontally with time (Onizawa *et al*., 2007). The precisely relocated hypocenters, based on a three-dimensional P-wave velocity structure, are located just below the lower boundary of the low resistive layer (Figure 17). This distribution also suggests the existence of a sharp boundary of the physical property. A sufficiently large amount of magma was located at near point Q to induce tilt movement of the volcanic edifice. Figure 16 indicates that the number of volcanic earthquakes is few at the location of the presumed magma body. The limited number of earthquakes may indicate that the magma body is still at high temperature and molten or partially molten. However, the magma body could not be identified from resistivity data. This is due to the insufficient sensitivity of the anomaly below the thick low resistivity layer (Matsushima *et al*., 2001), or lack of resistivity contrast between the cooling magma body and surrounding formations.

A relatively high resistive part (>500 Ωm) is located below Craterlet I at a depth from 200 m (a. s. l.) to 400 m (b. s. l.). This resistive part is interpreted as the cooling magma which may have intruded to a shallower part of the 1977 eruption site because the corresponding resistive part was not observed by the surveys just after the eruption (Ogawa *et al*., 1998). This intrusion is probably derived from the deep-seated magma body near point Q (Figure 13) which induced the tilting of the volcanic edifice. The inhomogeneous structures such as the original vents associated with Craterlet "Silver Pond", and Ko-Usu lava dome acted as a buffer between the NE inclined block and SW stationary block. The magma intruded into the shallow part at the boundary between the two blocks to compensate for the horizontal extension produced by the inclined movement. The upheaval of "New Mountain" (NM) continued to 1982, suggesting the deep-seated magma body had sufficient magmatic force causing further intrusion into shallow part. The phreatomagmatic explosions occurred repeatedly at Craterlet "Silver Pond" in 1978. The scale of the explosion and the content of fresh magma output increased gradually after the onset of the explosions (Niida *et al*., 1980). At the 1945 eruption of Usu Volcano, phreatomagmatic explosion started when the rising magma contacted the Quaternary aquifer (Yokoyama and Seino, 2000). The increase of pore pressure with vaporization of the water which leads to the rock failure, depends on the permeability of the formation: the lower the permeability, the larger the pore pressure (Delaney, 1982). On the other hand, an explosion, which is induced by vaporization, needs sufficient water in a permeable formation (Wohletz, 1986). A phreatomagmatic explosion occurs by satisfying these contradicting conditions. Although the hydrological condition at the summit of Usu Volcano is unknown, phreatomagmatic explosions at Craterlet "Silver Pond" are supposed to start when the intrusive magma passed through the Neogene layer constituted by less permeable altered rocks. The highly resistant part observed by magnetotelluric soundings probably indicates cooling of the intrusion at a shallow depth. The accompanying heat discharge from the surface after the 1977 eruption suggests that the pore of the high resistive part was filled with superheated vapor (Matsushima, 2003). Geochemical analysis of fumarole at Craterlet I indicates that the gas contains foreign water and the water vapor must be heated sufficiently before the mixture with the volcanic gas (Tomiya *et al*., 2012). These observations indicate that the highly resistive part also contains the high temperature rocks heated by magma and volcanic gas.

5.4 Structure of the summit part surveyed by muography

Installation sites of muographic equipment for volcanoes are limited mainly by topographic conditions: On and around Usu Volcano, some of the extruded structures were studied by muography, such as, the 1943 lava dome (SS) by Tanaka and Yokoyama (2000 2008 and 2013 in the reference list), and the 1910 mound (MS) by the same authors (2000).

Kusagaya and Tanaka (2015) developed a multi-layered telescope using seven detectors for selecting linear trajectories and preliminarily carried out a muographic survey for the summit part of this volcano with this muographer installed at the Usu Volcano Observatory (UVO in Figure 5). A muograph obtained after 38 days is shown in Figure 18b which shows a two-dimensional density map

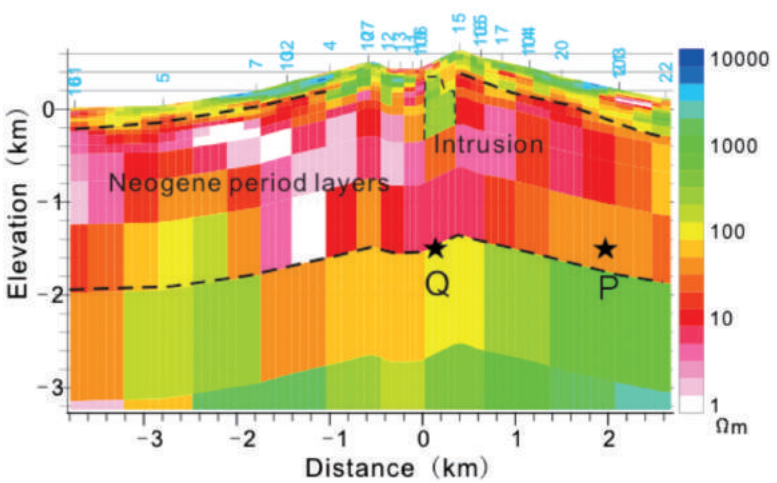

Figure 17. Resistivity cross-section through the center of Usu Volcano from SW to NE, obtained by the two-dimensional inversion of AMT and MT data, and its geological interpretations after Matsushima *et al.* (2001, Figure 5). "Intrusion" in the central part corresponds to the central magma conduit in Figure 13. Underground structure is divided to three layers by two broken lines; Quaternary, Neogene and Pre-Neogene period layers from surface to depth. The low resistivity area bounded by broken lines corresponds to the altered Neogene-period layers. Q and P are the same as those in Figure 13, and they are located on the lower boundary of Neogene period layers.

of the vertical cross-section along line A – B in Figure 18a.

A muograph of the summit part is shown in Figure 18b where the present muographic observation can detect the volcano structure roughly above the elevation angle of 150 mrad from the muographic telescope, or roughly, above 300 m (a.s.l.) in average. We may assume this anomaly below OY-NM line or A - B line, and here the former case is examined:

Along the elevation angle 150 mrad, anomalous material with density ρ, and range of muon path Δl are expected . The total path length of muon is about 2000 m in Figure 18c, the width of the intrusion is Δl, and the average density along the path is assumed to be 2.1 g/cc. Then, we obtain the following equation:

$$\Delta l \times \rho + (2000 - \Delta l) \times 2.0 = 2000 \times 2.1 \quad (\rho \text{ and } \Delta l \text{ are unknown}) \qquad (7)$$

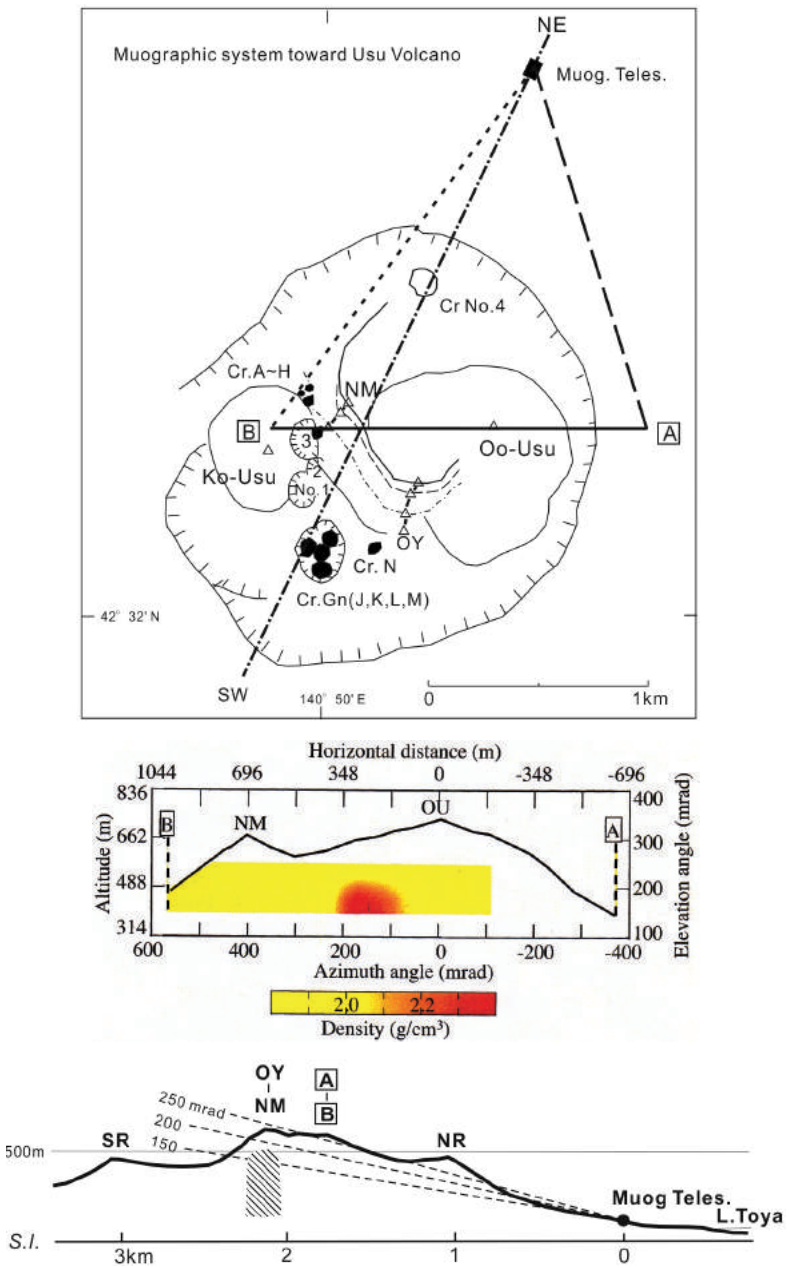

Figure 18. Muographic structure of Usu Volcano.
a) Muographic instrumentation after Kusagaya and Tanaka (2015)
b) A muograph along line B ~ A In Figure 18a (Kusagaya and Tanaka, 2015),
c) Interpretation: a hatched part is an assumed magma intrusion. Its muon path-length is expressed as Δl.

Here, a probable Δ l as 200 m was adopted considering the results of electric-resistivity surveys in Subsection 5.3, then the following relation was obtained:

$$200\times\rho+(2000-200)\times 2.0=2000\times 2.1 \quad (8)$$

The density of the anomalous material should be 3.0 g/cc. The horizontal position of the material ρ = 3.0 on the 150 mrad line cannot be precisely determined. Such material of high density may be the remnant of intruded magmas in the past, not in the 1977 eruption. Another observation from the EW direction is needed. In the present case, the time for the anomalous material intrusion could not be determined.

Magma reservoirs under Usu Volcano

Location and properties of magma reservoirs under active volcanoes are important parameters that influence their activities. After the 2000 eruption of Usu Volcano, magma reservoirs under the volcano were investigated with seismological and petrological methods.

Seismological methods: Generally the standards for detection of magma reservoirs by seismometric methods should be seismic wave velocities propagating through them, and reflections and refractions at their boundaries. First, the seismological method and results at Usu volcano are summarized as follows: Onizawa *et al*. (2007) studied the three-dimensional P-wave velocity structure of Usu Volcano by using first arrival time data of the 2001 active seismic survey. Hypocenters of precursory earthquakes of the eruption were accurately determined (Onizawa *et al*., 2002, 2007) and most of these were confined to depths of less than about 4 km. The scarcity of deeper earthquakes is considered to be caused by the ductile behavior of the crust as a result of its elevated temperature (Onizawa *et al*., 2007), suggesting the presence of magma bodies below 4 km depth. Large magma bodies have not been detected to a depth of about 7 km by seismological observations (Onizawa *et al*., 2007) nor electrical measurements (Matsushima *et al*., 2001).

Activity related to magma reservoirs beneath Usu Volcano, if any, should be governed by characteristics of dacitic magmas, of which viscosity is relatively high, and drastically changes with temperature and pressure. Goto (1997) measured viscosity of dry melts of Showa-Shinzan (SS dome) lavas, such as 10^7 Pa•s at 950 °C, and 10^9 Pa•s at 850 °C. The viscosities of magmas would increase by degassing (mainly H_2O) at the same temperature. At the boundary zone of a magma reservoir, all factors such as the material, temperature, mechanical strength and viscosity, would change continuously toward the center. Therefore such magma reservoirs cannot be considered as a simple sphere. Furthermore configurations of reservoirs may vary, from simple spheres to complicated assemblies of sills or dykes which are related to the genesis of the reservoirs. At present, their location can only be reliably discussed by seismic wave velocities.

The 2000 eruption was observed from various standpoints of seismology. In the present paper, a hypothesis is presented considering that usual parasitic eruptions of this volcano may be driven by magma branches or derivatives of the magma reservoir not by the magma reservoir itself (cf. 4.4 and Figure 15); only one exception is the 1943 eruption of SS dome. The 2000 eruption was not directly fed by the magma reservoir. Hence, within the reservoirs, physical parameters such as temperature and viscosity, may not always be uniform.

Petrological methods: Tomiya and Miyagi (2002) considered magma movement during the 2000 eruption of Usu Volcano as follows: (1) the 2000 eruption started by the ascent of magma from the deep (high-P) chamber; (2) this magma from the deep chamber was injected into the shallow (low-P) chamber; (3) this injection triggered an eruption at the surface from the shallow chamber. This process is similar to those proposed for other historical eruptions, all based on petrographic observations (Tomiya and Takahashi, 1995; 2005).

Tomiya *et al*. (2010) studied the rhyolite pumice from mafic magma that existed in the 1663 eruption (Us-b in Table 1) by high-pressure melting experiments, and determined the depth of magma reservoir just before the 1663 eruption as around 200 – 250 MPa (high-P), corresponding to a depth of about 8~10 km based on a crustal density structure. They consider this depth to be the level of mafic magma that existed beneath the rhyolitic magmas just before the 1663 eruption. On the other hand, Tomiya and Takahashi (20051995 in reference list) studied the eruptive products of Usu Volcano after the 1663 eruption and proposed that a new shallow magma reservoir (low-P) formed during or just after the 1663

eruption. On the basis of experimental results on the eruptive products, the pressure for the low-P magma is estimated at 100 ~ 150 MPa, corresponding to a depth of about 4 ~ 6 km. According to Tomiya *et al*. (2010), this depth may also correspond to the level of neutral buoyancy for the dacite

Geophysical methods, such as seismometric observations, have to be used to detect any deeper magma reservoirs beneath Usu Volcano and to confirm the results from petrological studies.

6. Concluding remarks

Interpretations of various eruptive events of Usu Volcano are presented in the above discussions. An hypothetical model of eruption activities mainly observed in the 20th century is tentatively developed below.

Based on P- and S-wave velocity structure and electrical resistivity structure, the shallow part of the volcano was modeled after 2000 by Onizawa *et al*. (2007) and Matsushima *et al*. (2001), respectively. Location of all of the magma reservoirs has not yet been established.

In the present discussion, the following results were reached:

a) Parasitic vents in the summit crater, "Golden Pond" and "Silver Pond" formed as twin parasites before historical time and reawakened in the 1977 eruption.

b) On Usu Volcano, during the last 350 years, its eruptions occurred almost regularly in time, and the ejected volumes have been dispersed, and generally the summit eruptions ejected larger volumes than parasitic ones.

c) The 1944 lava dome (SS dome) formed was a parasite at the base. This may be exceptional in the history of this volcano. Juvenile magma rarely reached the basal surface. It is recognized that the conduit to this lava dome was derived from a central part of the parental volcano. At present, this is the southernmost branch from the center of the volcano. It is not clear why the magma changed the direction at YH point. Based on the magma activities during the 1944 eruption, it seems possible that magma will extrude towards the S base in the future. S-ward migration of magmas just before the 2000 eruption observed by Onizawa *et al*. (2007) may support this possibility.

d) The 1977 eruption took place very near Ko-Usu lava dome that formed in 1769 AD. The conduits of the 1977 eruption have probably been very close to the lava dome. The magma conduit of Ko-Usu lava dome played a role at the first outbreak. Its magma reached the summit crater partly via the old conduit of Ko-Usu, rapidly in 32 hours, and without strong resistance accompanied only by small earthquakes, M≦3.7 in magnitude.

e) Analyses of the block movements at the summit part in the 1977 eruption indicate strong magmatic pressure that may cause the mountain to collapse.

Acknowledgements

The authors wish to cordially thank Dr. R. Y. Koyanagi who kindly checked our manuscript and contributed to improve the quality of the paper. Prof. S. De la Cruz-Reyna has been on Usu Volcano and gave us suitable criticism. Our best thanks are also due to him. The authors owe various observational data used in their discussion to many colleagues, too many to be mentioned individually but would express heartful thanks to all of them.

References

Anderson, E.M.,1936, The dynamics of the formation of cone-sheets, ring-dykes, and caldron-subsidences. *Proc. Roy. Soc. Edin*., 56, 128-157.

Bemmelen, R. W., van, 1949, The geology of Indonesia, Chapter 3: Volcanism, The Hague: Govt. Printing Office, 188-224.

De la Cruz-Reyna S., Yokoyama I., 2011, A geophysical chracterization of monogenetic volcanism. *Geofísica Internacional*, 50, 465-484.

Delaney, P.T., 1982, Rapid intrusion of magma into wet rock: Groundwater flow due to pore pressure increase. *J. Geophys. Res*. , 87, 7739-7756.

Goto, A., 1997, An experimental study on the viscosity of some silicate melts. Doctoral Thesis,

Graduate School of Science, Hokkaido University, 56 pp.

Harada, T., Yamashita H., Watanabe, H., 1979, Quasi-continuous observation of changes in distance caused by the 1977-78 eruption

of Usu volcano, Hokkaido. Geophys. Bull. Hokkaido Univ., 38, 31-40 (in Japanese with English abstract).

Inoue, W., 1948, Earthquakes and deformations accompanied by volcanic activities of Usu Volcano. *Quarterly Journal of Seismology,* 14, 9-24 (in Japanese)

Katō, T., 1909, Geology of Usu–dake volcano and Tōya lake. *Rep. Earthq. Inv. Comm*., No. 65, 1-72 (in Japanese).

Katsui, Y., 1973, Geological map of Usu volcano in the Report of Yokoyama *et al*., 1973.

Katsui, Y., Oba, Y., Onuma, K., Suzuki, T., Kondo, Y.,Watanabe, T., Niida, K., Uda, T., Hagiwara, S., Nagao, T.,, Nishikawa, J., Yamamoto, M., Ikeda, Y., Katagawa, H., Tsuchiya, N., Shirahase, M., Nemoto, S., Yokoyama, S., Soya, T. Fujita, T., Inaba, K., Koide, K., 1978, 1980 on page 8, Preliminary report of the 1977 eruption of Usu volcano. *J. Fac. Sci.*, Hokkaido Univ., ser. IV, 18, 385-408.

Kusagaya, T., Tanaka, H.K.M., 2015, Muographic imaging with a multi-layered telescope and its application to the study of the subsurface structure of a volcano. *Proc. Jpn. Acad, Ser*. B, 91, 501-510.

Maekawa, T., Watanabe, H., 1981, Damages caused by ground deformations accompanying the 1977-1978 eruption of Usu volcano, Hokkaido (2nd Report). *Geophys. Bull*. Hokkaido Univ., 40, 47-54 (in Japanese with English summary)

Matsumoto, A., Nakagawa, M., 2010, Formation and evolution of silicic magma plumbing system: Petrology of the volcanic rocks of Usu volcano, Hokkaido, Japan. J*. Volcanol. Geotherm. Res*., 196, 185-207.

Matsushima, N., 2003, Mathematical simulation of magma-hydrothermal activity associated with the 1977 eruption of Usu volcano. *Earth Planets Space*, 9, 559-568.

Matsushima, N. , Oshima, H.,Ogawa, Y., Takakura, S., Satoh, H., Utsugi, M., Nishida, Y., 2001, Magma prospecting in Usu volcano, Hokkaido, Japan, using magnetotelluric soundings. *J. Volcanol. Geotherm. Res*., 109, 263-277.

Minakami, T., Ishikawa, T., Yagi, K., 1951, The 1944 eruption of Volcano Usu in Hokkaido, Japan. *Bull. Volcanol*., 11, 45-157.

Mizukoshi, I., Moriya, T., 1980 1979 on Fig 14 caption, Broad band and wide dynamic range observation of Usu volcano earthquake swarm. *J. Seismol. Soc. Jpn*., 33, 479-491 (in Japanese with English abstract).

Mori, H.Y., Ui, T., 2000, Crustal deformation and eruptic activities of Mt. Usu in 2000. J. JSNDS 19, 383–390 (in Japanese with English abstract).

Nakagawa, M., Matsumoto, A., Tajika, J., Hirose, S., Ohtsu, T., 2005, Re-investigation of eruption history of Usu volcano, Hokkaido, Japan: Finding of Pre-Meiwa Eruption (Late 17th Century) between Kanbun (1663) and Meiwa (1769) eruption. *J. Volcano. Soc. Jpn*,, 50, 39-52 (in Japanese with English abstract)

Nemoto, T,. Hayakawa, M., Takahashi, T., Oana, S., 1957, Report on the geological, geophysical and geochemical studies of Usu volcano (Showa-shinzan). Report No. 170, *Geol. Surv. Jpn* (in Japanese with English abstract), 149 pp.

Niida, K., Katsui, Y., Suzuki, T., Kondo, Y., 1980 1979 on page 8, The 1977-1978 eruption of Usu volcano. *J. Fac. Sci*. Hokkaido Univ., ser. IV, 19, 357-394.

Ogawa, Y., Matsushima, N., Oshima, H., Takura, S., Utsugi, M., Hirano, K., Igarashi, M., Doi, T., 1998, A resistiviity cross-section of Usu volcano, Hokkaido, Japan, by audiomagnetotelluric soundings. *Earth Planets Space*, 50, 339-346.

Okada, Hm., Watanabe, H., Yamashita, H., Yokoyama, I., 1981. Seismological significance of the 1977-1978 eruption s and the magma intrusion processsof Usu volcano, Hokkaido. *J. Volcanol. Geotherm. Res*., 9, 311-334.

Ōmori, F. ,1911 and 1913, The Usu-san eruption and earthquake and elevation phenomena. *Bull. Imp. Earthq. Inv. Com*., 5, 1-137.

Onizawa, S., Oshima, H., Mori, H., Maekawa, T., Suzuki A.,, Ichiyanagi, M., Okada Hm,, 2002, Three-dimensional seismic velocity structure around Usu volcano, Japan. *J. Volcanol. Soc. Jpn*, 47, 495-506 (in Japanese with English abstract)

Onizawa, S., Oshima, H., Aoyama, H., Mori, H. Y., Maekawa, T., Suzuki, A., Tsutsui, T., Matsuwo, N., Oikawa, J., Ohminato, T.,

Yamamoto, K., Mori, T., Taira, T., Miyamachi, H., Okada, H., 2007, P-wave velocity structure of Usu volcano: Implication to the structural controls on magma movements and eruption locations. *J. Volcanol. Geotherm. Res.,* 16, 175-194.

Satō, D., 1913 1910, Preliminary report on the explosion of Usu Volcano. *Rep. Geol. Surv. Jp*, 22, 6-46 (in Japanese).

Seino, M., 1983, Seismic activity accompanying the 1977-1978 eruption of Usu volcano, Japan. *Paper Met. Geophys*. 54, 105-141.

Tanaka, H.K.M., Yokoyama, I., 2008, Muon radiography and deformation analysis of the lava dome formed by the 1944 eruption of Usu, Hokkaido —Contact between high-energy physics and volcano physics—. *Proc. Jpn. Acad. Ser*. B 84, 107-116.

Tanaka, H.K.M.,. Yokoyama, I., 2013, Possible application of compact electronics for multilayer muon high-speed radiography to volcanic cones. *Geosci. Instrum. Method. Data Syst*., 2, 263-273.

Tomiya, A. Takahashi, E. 1995 2005 on page 18, Reconstruction of an evolving magma chamber beneath Usu volcano since the 1663 eruption. J. Petrol., 36, 617-636.

Tomiya, A., Miyagi, I., 2002, The eruptive products and magma process of March 31, 2000 eruption of Usu volcano. *Bull. Volcanol. Soc. Jpn.*, 47, 663-673 (in Japanese with English abstract).

Tomiya, A.,Takahashi, E., Furukawa, N. Suzuki, T., 2010, Depth and evolution of a silicic magma chamber: Melting experiments on a low-K Rhyolite from Usu volcano, Japan. *J. Petrol.,* 51, 1333-1354.

Tomiya, A., Matsushima, N., Shinohara, H., Miyagi, I., Urai, M., Sato, T., 2012, Researches on active volcanoes: Usu volcano, Geological survey of Japan, AIST, URL: https:// gbank.gsj.jp/volcano/ Act_ Vol/usu/vr/index.html (in Japanese).

Yokoyama, I., 1964, Preliminary report on a gravimetric survey on Toya caldera, Hokkaido, Japan. *J. Fac. Sci*., Hokkaido Univ. Ser. VII, 11, 247-250.

Yokoyama, I., 2002, Growth mechanism of the 1944 lava dome of Usu volcano in Hokkaido, Japan. *Proc. Japan Acad*., 78, Ser. B, 6-11.

Yokoyama, I., 2015, Eruption patterns of parasitic volcanoes. Annals of Geophysics, 58, SO327.

Yokoyama, I., Katsui, Y,. Oba, Y., Ehara, S., 1973, Usu volcano: geology and geophysics. Report of Hokkaido Prefecture, Sapporo, 254p. (in Japanese).

Yokoyama, I., Yamashita, H., Watanabe, H., Okada, Hm., 1981, Geophysical characteristics of dacite volcanism –- The 1977- 1978 eruption of Usu volcano. *J. Volcanol. Geotherm. Res*., 9, 335-358.

Yokoyama, I., Seino, M., 2000, Geophysical comparison of the three eruptions in the 20th century of Usu volcano, Japan. *Earth Planets Space*, 52, 73-89.

Watanabe, H., 1983, Changes in water level and their implications to the 1977-1978 activity of Usu volcano. Arc Volcanism: Physics and Tectonics, edited by D. Shimozuru and I. Yokoyama, 81-93.

Wohletz, K. H.,1986, Explosive magma-water interactions: Thermodynamics, explosion mechanisms, and field studies. *Bull. Volcanol*., 48, 245-264.

Geofísica Internacional (2018) 57-1: 39-58

Original paper

Estimation of ground subsidence in the city of Morelia, Mexico using Satellite Interferometry (INSAR)s

Gerardo Suárez, Said H. Jaramillo, Penélope López-Quiroz and Osvaldo Sánchez-Zamora

Received: June 07, 2017 ; accepted: October 19, 2017; published on line: January 01, 2018

Resumen

La ciudad de Morelia, en la zona central de México, ha sido afectada en años recientes por la subsidencia diferencial del suelo que se refleja en forma de fallas y fracturas en la superficie. El objetivo de este trabajo es el obtener series de tiempo de la deformación del suelo utilizando interferogramas InSAR, con el fin de determinar la evolución espacial y temporal de la subsidencia en la ciudad de Morelia. Con este fin se procesaron 28 imágenes de ENVISAT-ASAR, adquiridas de mayo de 2003 a septiembre de 2010. Se limitaron las lineas de base perpendiculares y temporales a ser menos de 400 m y 420 días respectivamente, como un criterio de calidad para seleccionar los interferogramas. De un total de 378 interferogramas, se consideró que únicamente 65 tenían la suficiente calidad para ser usados en la inversión, basado en la decorrelación obervada en las señales. Los resultados muestran que la mayor parte de la ciudad de Morelia no está afectada por subsidencia del suelo de manera significativa. En areas donde si hay subsidencia del terreno, las velocidades varían de 0.7 a 5 cm/año. La mayor subsidencia se da en forma de estructuras circulares y a lo largo de algunas de las fallas observadas en la superficie. La subsidencia del terreno está concentrada en áreas específicas al pie de la fallas La Colina, Central Camionera y La Paloma. Sin embargo, la subsidencia no es continua a lo largo de estas fallas y se observa únicamente en segmentos especificos de las mismas. En algunos casos, como por ejemplo la falla La Paloma, la subsidencia parece estar asociada con fuertes cambios litológicos entre el techo y el piso de las fallas. En otros casos, como en las fallas Central Camionera y La Colina, la subsidencia diferencial observada parece estar asociada a la compleja estructura del basamento y del subsuelo de la ciudad de Morelia, y relacionada primordialmente con la compactación diferencial de los sedimentos de la cuenca.

Palabras clave: Subsidencia del terreno, interferometría, InSAR, Morelia, México, extracción de aguas subterráneas

G. Suárez
O. Sánchez-Zamora
Instituto de Geofísica
Universidad Nacional Autónoma de México
Ciudad Universitaria
Delegación Coyoacán 04510
México CDMX, México
*Corresponding author:

S. H. Jaramillo
Posgrado en Ciencias de la Tierra
Instituto de Geofísica
Universidad Nacional Autónoma de México
Ciudad Universitaria
Delegación Coyoacán 04510
México CDMX, México

P. López-Quiroz
Centro de Geociencias
Universidad Nacional Autónoma de México
Querétaro, México

Abstract

In recent years, the city of Morelia, in central Mexico, has been affected by differential subsidence of the soil evidenced by faults and fractures on the ground. The goal of this study is to obtain ground deformation time series from InSAR interferograms, in order to determine the temporal and spatial evolution of subsidence in the city of Morelia. Twenty-eight ENVISAT-ASAR images, acquired from May 2003 to September 2010, were processed. Perpendicular and temporal baselines of less than 400 m and 420 days respectively, were used as criteria to select interferograms. From a total of 378 interferograms, only 65 were considered to be of sufficient quality, based on the observed signal decorrelation. The results show that most of the city of Morelia is not affected by significant subsidence. In the areas where subsidence occurs, the rates of subsidence vary between 0.7 and 5 cm/yr. Most of the subsidence is in the form of discrete circular patterns and along segments of the observed surface faults. Ground subsidence is concentrated in specific areas on the footwalls of La Colina, Central Camionera and La Paloma faults. Subsidence, however, is not continuous along these faults, but observed only in some segments. In some cases, as in the case of La Paloma fault, the subsidence appears to be directly associated with the strong lithological contrast between the footwall and the hanging wall. In the other two cases, such as the Central Camionera and La Colina faults, the differential subsidence observed appears to be related with the complex basement and sedimentary structure of the volcanic subsoil of the city of Morelia and related primarily to differential compaction of the sedimentary fill.

Key words: Ground subsidence, interferometry, InSAR, Morelia, Mexico, ground water extraction.

Introduction

The subsidence of sedimentary basins is a process that affects many cities worldwide (*e.g*., Amelung *et al*., 1999; Buckley *et al*., 2003; Chai *et al*., 2004; Dehghani *et al*., 2009; Ding *et al*., 2004; Le Mouélic *et al*., 2005; Lu and Liao, 2008; Marfai and King, 2007; Stramondo *et al*., 2008; Strozzi *et al*., 2001; Vilardo *et al*., 2009; Watson *et al*., 2002). In general, differential ground subsidence in urban areas is related to the withdrawal of groundwater to meet human, industrial and agricultural needs (Poland, 1984). The over-exploitation of the aquifers decreases the pore pressure and induces the compaction of the sediments as a result of the inelastic deformation of the aquitard (Amelung *et al*., 1999).

The firsts cases of differential subsidence in Mexico due to water extraction were observed in Mexico City in the early 1920s (Gayol, 1925). Subsidence increased rapidly from 1930 to 1960 due to the rapid growth of the population (Ortega-Guerrero *et al*., 1993). Carrillo (1948) was the first to relate directly the subsidence with the over-exploitation of the aquifers in Mexico City. In the 1980s, differential subsidence began to be observed and documented in several cities in central Mexico, such as: Aguascalientes, Morelia, Celaya, Irapuato, Salamanca, Querétaro, Toluca and San Luis Potosí (*e.g*., Aguirre-Díaz *et al*., 2000; Ávila-Olivera, 2008; Ávila-Olivera *et al*., 2010; Ávila-Olivera and Garduño-Monroy, 2006; Calderhead *et al*., 2011; Carreón-Freyre and Cerca, 2006; Castañeda *et al*., 1993, 1995; Chávez-Alegría, 2008; Cigna *et al*., 2011; 2012; Esquivel, 2009; Farina *et al*., 2007, 2008; Garduño-Monroy *et al*., 2001; López-Doncel *et al*., 2006; Mejía-Gómez and Sandoval-Minero, 2004; Pacheco-Martínez; 2007; Pacheco-Martínez and Arzate-Flores, 2007; Pacheco-Martínez *et al*., 2006; Schroeder-Aguirre, 2010; Trujillo-Candelaria, 1989, 2009; Vargas, 1999; Zermeño de León *et al*., 2004, 2005;).

More recently, interferometric techniques were used to study the rapid subsidence of Mexico City and its suburbs (e.g., Strozzi and Wegmüller, 1999; Strozzi *et al*., 2001; Carreón-Freyre *et al*., 2006; Cabral-Cano *et al*., 2008; López-Quiroz, 2008; López-Quiroz *et al*. 2009; Osmanolu *et al*., 2011). The common denominator shared by these cities is their location on lacustrine and fluvial-lacustrine basins filled with sediments that are heterogeneous in both composition and structure.

In the particular case of the city of Morelia, discussed in this paper, subsidence of the ground was first recognized in 1983, coinciding with the rapid increase of the urban population (Arreygue-Rocha *et al*., 2002; 2005). The differential subsidence was manifested on the surface as soil fractures damaging houses and buildings in the urban area (*e.g*., Garduño-Monroy *et al*., 2001; Ávila-Olivera and

Garduño-Monroy, 2006; Ávila-Olivera, 2008). The Central Camionera and La Colina faults were the first physiographic features identified as resulting from the differential subsidence of the ground (Figure 1). The rates of subsidence reported from *in situ* measurements range from 4 to 6 cm/yr (Garduño-Monroy *et al*., 2001). To our knowledge, no routine and repeated measurement of ground deformation are done in the city.

Several faults affecting the city of Morelia have been mapped: La Paloma, La Colina, Central Camionera, Cuautla, Torremolinos, El Realito, La Soledad, Chapultepec and Ventura Puente (Ávila-Olivera, 2008; Ávila-Olivera and Garduño-Monroy, 2008; Cabral-Cano *et al*., 2010; Cigna *et al*., 2012) (Figure 1). The orientation of these faults is predominantly NE-SW and E-W. Several authors proposed that these faults are parallel to the mapped regional tectonic faults (Ávila-Olivera, 2008; Ávila -Olivera and Garduño-Monroy, 2006; Farina *et al*., 2007; 2008; Garduño-Monroy *et al*., 2001). Furthermore, Garduño-Monroy *et al*., (2001) suggested that La Colina and La Paloma faults are the surface expression of motion on basement faults of tectonic origin.

The early studies that measured subsidence in the city of Morelia using InSAR were based on interferograms produced using only images pairs (Table 1). More recently, Cabral-Cano *et al*. (2010) and Cigna *et al*. (2012) used the method of persistent scatterers (PSI) (Ferreti *et al*., 2000; 2001) to obtain time series of the subsidence at specific locations. Chaussard *et al*., (2014) used the Small Baselines (SBAS) methodology on ALOS images to estimate average subsidence in the city. Here, we extend the work of Cigna *et al*. (2012) using the method of SBAS (Berardino *et al*., 2002; Schmidt and Bürgmann, 2003; Usai, 2003; Cavalié *et al*., 2007; López-Quiroz *et al*., 2009) to obtain time series of the subsidence across several cross sections and specific locations. The purpose of applying this technique was to increase the signal coherence and to minimize its temporal and spatial decorrelation (Berardino *et al*., 2002; Yan *et al*., 2009). The use of this method allowed us to obtain reliable time series that reflect the evolution of the ground deformation as a function of time, induced by subsidence of the soil in Morelia.

InSAR processing

Twenty-eight ENVISAT-ASAR images, acquired from May 2003 to September 2010, were processed using the software *JPL/CalTech Repeat Orbit Interferometry Package (ROI_PAC)* (Rosen *et al*., 2004). *ROI_PAC* was used to

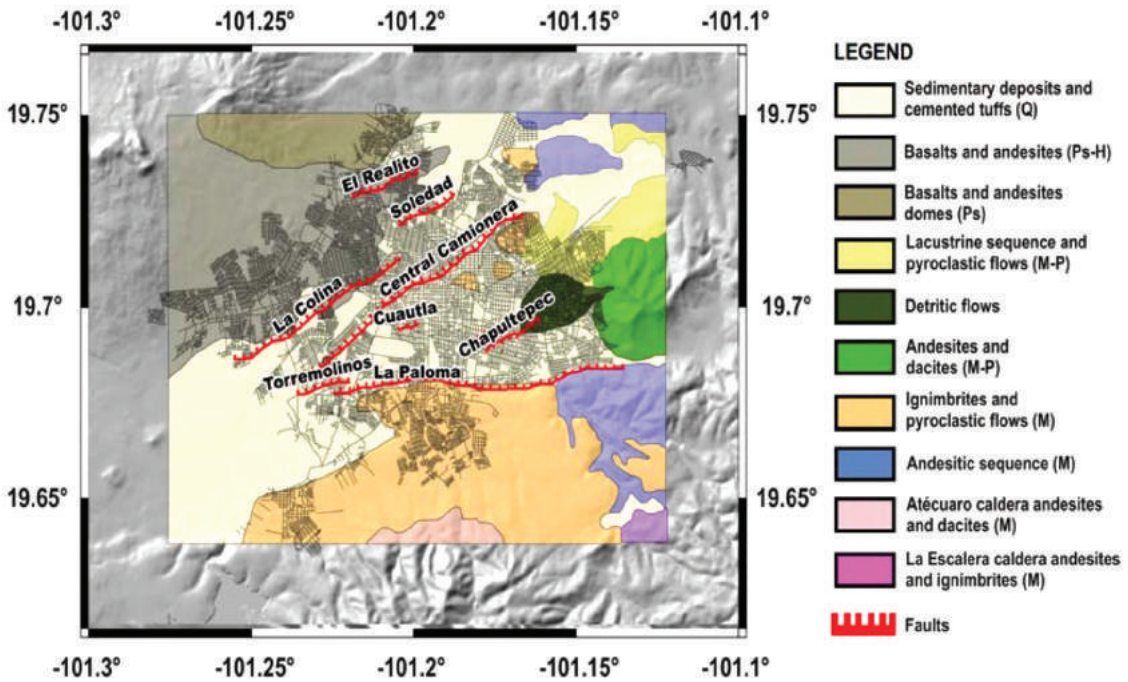

Figure 1. Geological setting and location of the main faults that affect the city of Morelia in Michoacán, México (modified from Cigna *et al*., 2012). Abbreviations: Q-Quaternary; Ps-Pleistocene; H-Holocene; M-Miocene.

Table 1. Analyses carried out in Morelia using InSAR.

Author	Method	Interferograms spanning time	Subsidence [mm/yr]
Farina *et al*. (2007)	DInSAR[1]	July 2003 – November 2004 December 2004- December 2005	10-35
Ávila-Olivera (2008)	DInSAR[1]	July 2003 – November 2004 December 2004- December 2005	10
Farina *et al*. (2008)	DInSAR[1]	July 2003 – November 2004 December 2004- December 2005	10-35
Ávila-Olivera *et al*. (2010)	DInSAR[1]	July 2003 – November 2004	35
Cabral-Cano *et al*. (2010)	PSI[2]	July 2003 – October 2009	50
Cigna *et al*. (2011)	PSI[2]	July 2003 – October 2009	50
Cigna *et al*. (2012)	DInSAR[1] PSI[2]	July 2003 – May 2009	70-80 40-50

[1] DInSAR – Differential Interferometry
[2] PSI: Permanent Scatterer Interferometry

construct and to unwrap the interferograms. All scenes are descending-orbit images (track 69, frame 3213). The orbital fringes were removed using the satellite orbital corrections provided by the Department of Earth Observation and Space Systems (*DEOS*) of Delft University of Technology and by the European Space Agency (*ESA*). The topographic contribution was corrected using a 1" arc, digital elevation model (DEM) resampled from the 3" arc DEM of the Shuttle Radar Topography Mission (*SRTM*) (Farr and Kobrick, 2000). Multilooking by a factor of five was applied in the direction of azimuth. This process leads to a ground pixel resolution of ~20 x 20 m. In order to increase the signal to noise ratios, a nonlinear adaptive spatial filtering (Goldstein and Werner, 1998) was applied to all interferograms. As described below in more detail, the interferograms were unwrapped using the branch-cut algorithm (Goldstein *et al*., 1988).

In order to avoid loss of coherence in the interferograms, their baselines were limited to 1) spatial perpendicular baselines of less than 400 m; and 2) temporal baselines of less than 420 days. As a result, 65 interferograms were selected, constituting two separate groups (Figure 2). The first one spans from July 2003 to January 2007, and the second from December 2008 to September 2010. Unfortunately there are no InSAR acquisitions in the region from February 2007 to November 2008. Usai (2003) proposed to overcome large gaps in the interferometric data by creating synthetic interferograms that predict a particular deformation behavior. However, the period missing is very long to select *a priori* a reliable behavior. Therefore, the two observational periods are treated as independent groups.

Atmospheric phase delays due to the vertical stratification of the atmosphere (Hanssen, 2001) and to the orbital inaccuracies, for which we estimate the best fitting 'twisted plane' (Cavalié *et al*., 2007), were calculated simultaneously following López-Quiroz *et al*. (2009). The corrected interferograms were co-registered prior to the inversion process. The phase delay time series were obtained using a least-squares inversion (*e.g.,* Cavalié *et al*., 2007). The mean square errors (RMS) of all interferograms and pixels were calculated in order to detect unwrapping errors and inconsistencies in the interferometric dataset (Appendix A).

Finally, average subsidence rates were calculated as a function of time for all pixels meeting the following criteria: 1) To have the complete number of acquisitions and; 2) To show an RMS error of less than 0.5 rad. All analyses were performed in radar geometry and later geo-referenced to the DEM.

Description of the inversion process

As suggested by Schmidt and Bürgmann (2003), the inversion process was performed without smoothing in order to avoid aliasing effects. The names of the interferograms are identified by the year, month and day of the images used

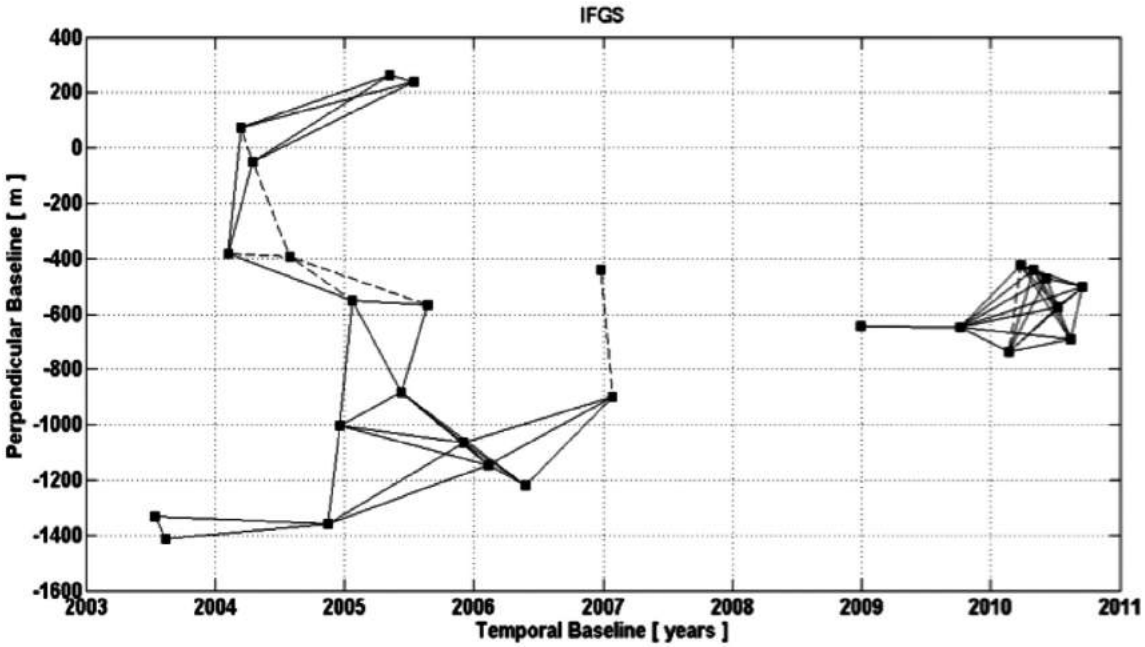

Figure 2. The squares represent the 28 InSAR images obtained for the city of Morelia from 2003 to 2010, plotted as a function of the acquisition date. The solid lines represent the 55 interferograms utilized during the inversion process. The dashed lines represent the 10 interferograms discarded in the inversion process.

to calculate them. Interferograms 20040313-20040417, 20061223-20070127, 20100220-20100327, 20100327-20100501, 20100327-20100605, and 20100501-20100605 were discarded because they did not meet the quality criteria described before. Furthermore, all interferograms sharing the common image 20040731 (20040207-20040731, 20040417-20040731, 20040731-20050122, 20040731-2050820) were not included in the analysis due to the strong atmospheric effects observed in that particular scene, which greatly increased the RMS errors.

Fifty-five interferograms were used in the analysis (Tables 2 and 3). The RMS values of the interferograms used to evaluate the time series are described in equations 2 and 5 in Appendix A and graphically shown on Figure 3.

Discussion of results

Regional ground subsidence in Morelia

The results of the analysis of the two independent time series show that, on a regional scale, most of the urban sprawl of Morelia is not affected by significant ground subsidence (Figures 4a and 4b). During the seven years studied, the average surface deformation was ±0.5 cm/yr. These values are within the error of the methodology. The areas showing subsidence occur on the footwall of some of the mapped faults. The subsidence, however, is not continuous along the whole length of the faults. Subsidence is concentrated in the western part of the city and on specific segments of La Paloma, Central Camionera and La Colina faults. The areas showing ground deformation are consistently the same in the two time series spanning this ten-year period, indicating that the subsidence is consistent in time and areal extent (Figures 4a and 4b). However, our results show a small general increase in the subsidence rate of the affected areas from December 2008 to September 2010, relative to the one observed from July 2003 to January 2007 (Figures 4a and 4b). Cigna *et al*. (2012) observed also this increase in subsidence in the latter years.

Although La Paloma fault represents one of the starker lithological contacts in the city, between the Miocene ignimbrite sequence of the Sierra Mil Cumbres and the basin fill formed by Quaternary sedimentary deposits and cemented tuffs (Figure 1), subsidence is observed mostly in the western end of the fault (Figures 4a and 4b). In this area of La Paloma fault, the zones that were mostly affected by a rapid rate of subsidence are residential areas in the southwestern part of the city: *INFONAVIT Villa Universidad, Valle Quieto, Arboledas,* and *Residencial del Sur.*

Table 2. Interferograms corresponding to the time series July 2003 to January 2007.

ID[1]	Interferogram[1]	B_t[2] [days]	B_D[3] [m]	ID[1]	Interferogram[1]	B_t[2] [days]	B_D[3] [m]
1	20030712-20030816	35	-83	16	20041218-20051203	350	-63
2*	20030712-20041113	490	-28	17	20041218-20060211	420	-141
3*	20030816-20041113	455	55	18	20050122-20050611	140	-335
4*	20040207-20040313	35	457	19	20050122-20050820	210	-16
5	20040207-20040417	70	335	20	20050607-20050716	70	-23
6	20040207-20050122	350	-167	21	20050611-20050820	70	319
7	20040313-20050507	420	188	22	20050611-20051203	175	-182
8[1]	20040313-20050716	490	165	23	20050611-20060211	245	-260
9	20040417-20050507	385	310	24	20050611-20060527	350	-335
10[1]	20040417-20050716	455	287	25	20051203-20060211	70	-78
11	20041113-20041218	35	355	26	20051203-20060527	175	-153
12	20041113-20051203	385	292	27	20051203-20070127	420	166
13[1]	20041113-20060211	455	214	28	20060211-20060527	105	-75
14	20041218-20050122	35	454	29	20060211-20070127	350	244
15	20041218-20050611	175	119	30	20060527-20070127	245	319

[1] Interferogram number. The interferogram was built using the satellite image pairs expressed as year, month and day. The asterisk indicates the interferogram did not meet the prescribed quality criteria.
[2] B_t is the temporal baseline between subsequent radar images
[3] B_D is the spatial perpendicular baseline between subsequent radar images

Table 3. Interferograms corresponding to the time series December 2008 – September 2010.

ID[1]	Interferogram[1]	B_t[2] [days]	B_D[3] [m]	ID[1]	Interferogram[1]	B_t[2] [days]	B_D[3] [m]
1	20081227-20091003	280	-1	14	20100327-20100710	105	-150
2	20091003-20100220	140	-90	15	20100327-20100814	140	-266
3	20091003-20100327	175	224	16	20100327-20100918	175	-79
4	20091003-20100501	210	207	17	20100501-20100710	70	-133
5	20091003-20100605	245	178	18	20100501-20100814	105	-249
6	20091003-20100710	280	74	19	20100501-20100918	140	-62
7	20091003-20100814	315	-42	20	20100605-20100710	35	-104
8	20091003-20100918	350	145	21	20100605-20100814	70	-220
9	20100220-20100501	70	297	22	20100605-20100918	105	-33
10	20100220-20100605	105	268	23	20100710-20100814	35	-116
11	20100220-20100710	140	164	24	20100710-20100918	70	71
12	20100220-20100814	175	48	25	20100814-20100918	35	187
13	20100220-20100918	210	235				

[1] Interferogram number. The interferogram was built using the satellite image pairs expressed as year, month and day.
[2] B_t is the temporal baseline between subsequent radar images
[3] B_D is the spatial perpendicular baseline between subsequent radar images

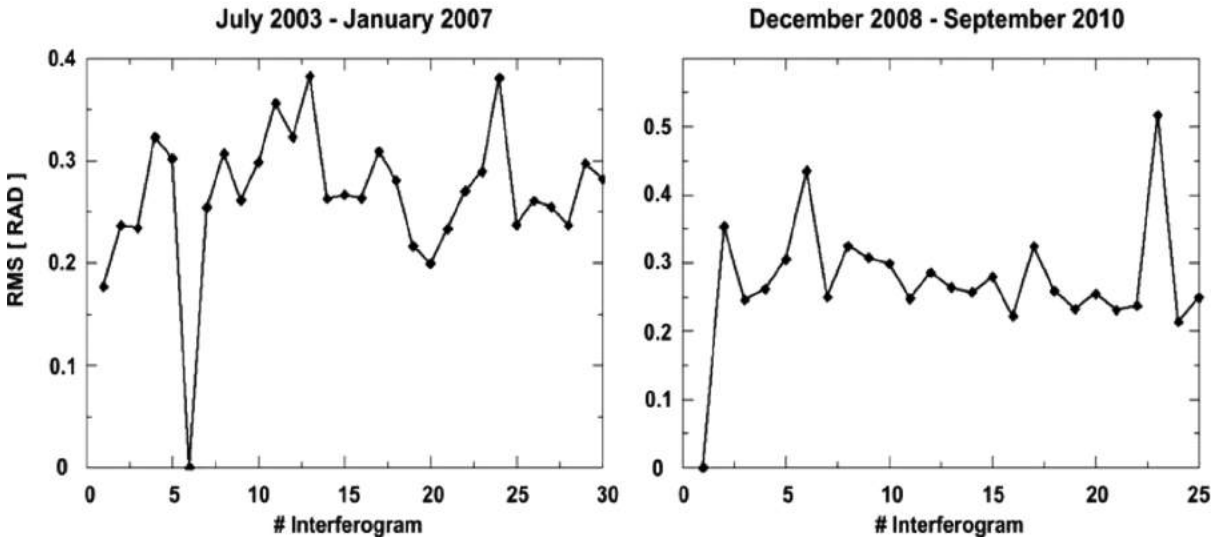

Figure 3. RMS values of the individual interferograms used in the final inversion process.

In the central part of the city of Morelia, the Chapultepec and Cuautla faults show no evidence of ground deformation during the seven years of observation (Figures 1, 4a and 4b). Both time series indicate that no discernable subsidence takes place near these faults during the observation period (Figures 4a and 4b). Farther to the north, the Central Camionera fault reflects rapid subsidence in the central part, gradually tapering off towards the west. The eastern Central Camionera fault shows no evidence of subsidence. The relatively rapid subsidence observed in the central segment of the Central Camionera fault affects the neighborhoods of *El Porvenir, Ampliacion Porvenir* and *Las Flores*.

La Colina fault, to the northwest of the city, reflects the geological boundary between the Pliocene basalts and andesites and the sediment fill of Quaternary age (Figure 1). The footwall of La Colina fault reflects subsidence along its whole length (Figures 4a and 4b). Comparing the two periods analyzed, the largest increase in the rate of subsidence took place along the eastern end of La Colina fault from December 2008 to September 2010 (Figure 4b). Subsidence on La Colina fault affects the housing units of *INFONAVIT Adolfo López Mateos, Las Águilas, Agua Clara,* and the neighborhoods *La Quemada, Irrigacion* and *Vicente Guerrero*.

Cigna *et al*. (2012) did not report a correlation between the ground subsidence in the city and the rate of water extraction and the decrease of the static level of the water wells. In the same manner, a comparison of the ground subsidence with the thickness of the Quaternary deposits showed no relation to the areas of high subsidence rates. Our results confirm the observations made by Cigna *et al*. (2012), suggesting that the subsidence is not directly and exclusively controlled by the thickness of the sediments or by the water extraction rates. The variables controlling the subsidence of the ground appear to be the complex structural distribution of the volcanic deposits forming the Morelia basin and the preexisting basement topography.

Subsidence time series and cross sections in the areas of higher subsidence

As mentioned above, we use the method of Small Baselines (SBAS) (Berardino *et al*., 2002; Schmidt and Bürgmann, 2003; Usai, 2003; Cavalié *et al*., 2007; López-Quiroz *et al*., 2009) in order to extend the work of Cigna *et al*. (2012). The use of this method allowed us to obtain reliable time series that reflect the evolution of the deformation induced by the subsidence in Morelia. Based on this approach, time series of the ground deformation were estimated across several cross sections of the faults. Also, rates of subsidence as a function of time were obtained for several locations in the city (Figures 4a, 4b and 5).

In order to construct the time series and the cross sections, only pixels that met the criteria of having a RMS < 0.5 rad were selected (see Equation 3 in Appendix A). In addition, the selected pixels had to be present in all interferograms. These criteria guarantee a reliable depiction of the behavior and velocity

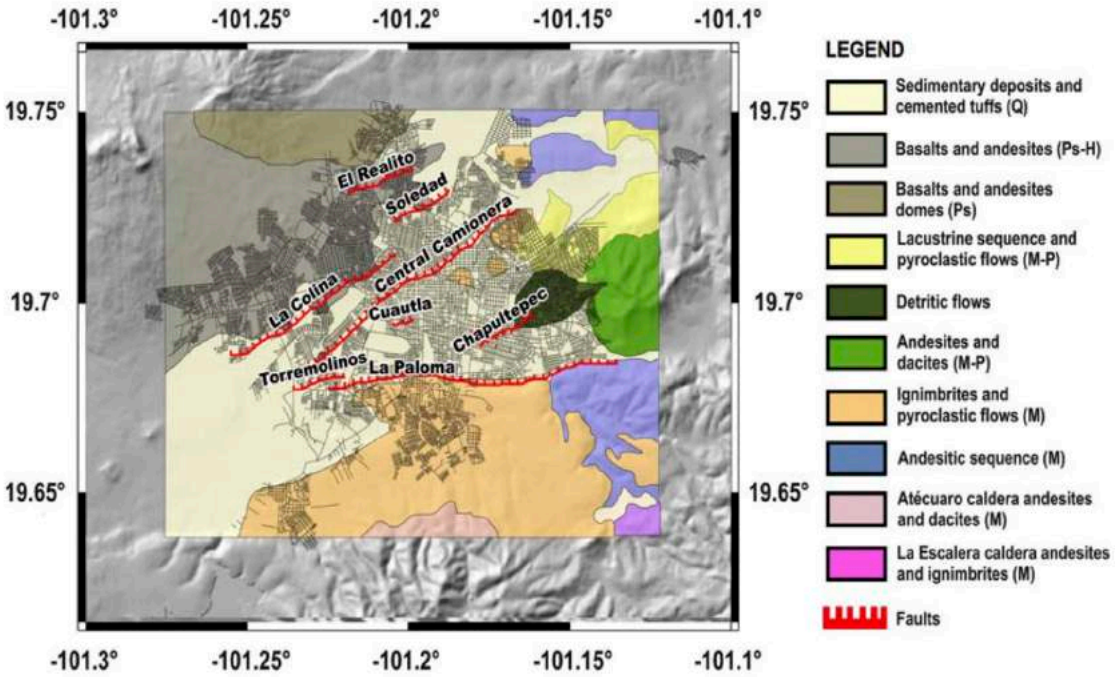

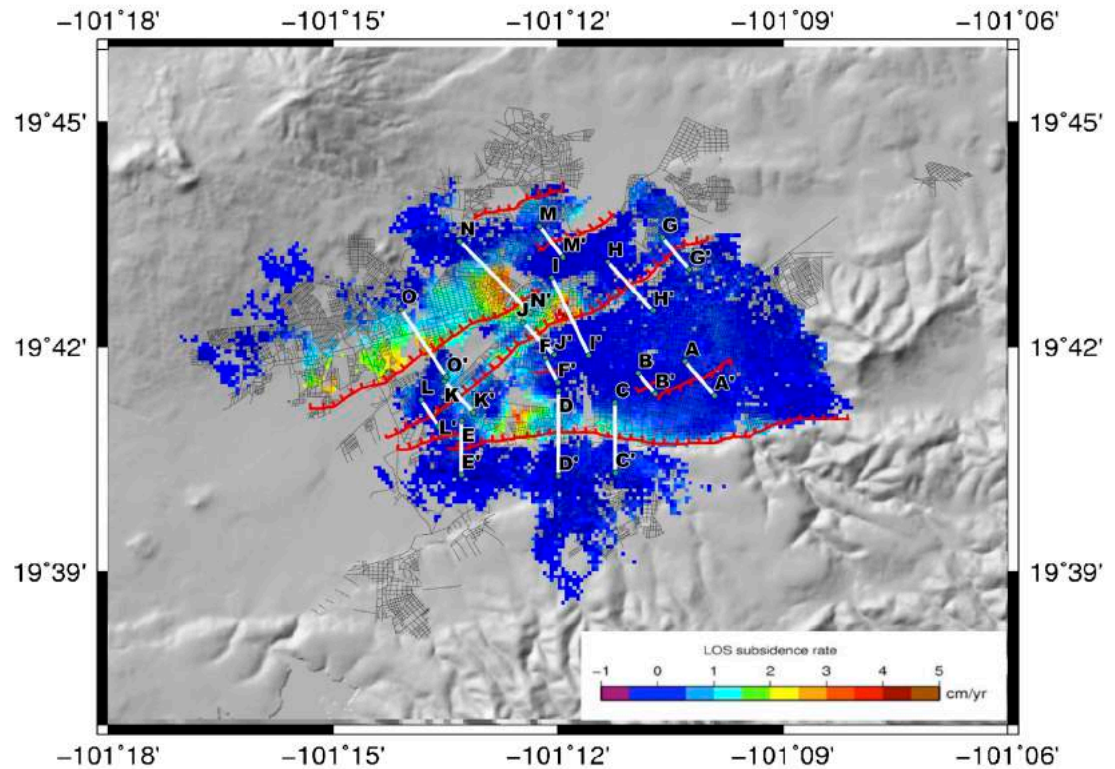

Figure 4. The maps show the average annual rate of subsidence along the Line of Sight (LOS) of the satellite: 4a) During the period July 2003 – January 2007; and 4b) from December 2008 to September 2010.

of the ground deformation (*e.g.,* López-Quiroz, 2008). All the cross sections and time series calculated are shown in the Electronic Supplement to this paper. In the discussion, we select some relevant examples to illustrate and discuss the observations.

Deformation in the vicinity of La Paloma fault

Three cross sections were calculated across the La Paloma fault (Sections CC', DD' and EE' on Figures 4a and 4b). Also, subsidence time histories were estimated for representative locations near the fault (points D, E, F, and G on Figure 5). Points D and E show that the hanging wall of La Paloma fault, on the Mil Cumbres Sierra, is stable in the seven-year period observed by the data. In these two points the rate of deformation is less than 1 mm/yr (see Electronic Supplement). Immediately to the north of point E, point G shows a rate of subsidence of approximately 0.7 cm/yr (Figure 6). This rate of subsidence is maintained consistently throughout the seven years covered in this study. Point F, in the western end of La Paloma fault shows a rate of subsidence of 1.8 cm/yr in the period from July 2003 to January 2007 (Figure 6); the subsidence rate later increased to 2.6 cm/yr, from December 2008 to September 2010 (Figure 6). In all cases, the subsidence of the ground behaves quasi linearly as a function of time, displaying no significant seasonal variations.

Cross sections across La Paloma fault show very different subsidence histories. Sections CC' and DD', located in the central part of La Paloma fault (Figure 4a), show an average rate of subsidence of approximately 1 cm/yr; a value similar to the subsidence rate observed in location G (see Figure 7 and Electronic Supplement). In the case of cross section EE', located in the western end of La Paloma fault, no discernible subsidence is present (Figure 7). The results of these three cross sections drawn across La Paloma fault depict the variability of ground subsidence in Morelia in different segments of the same fault.

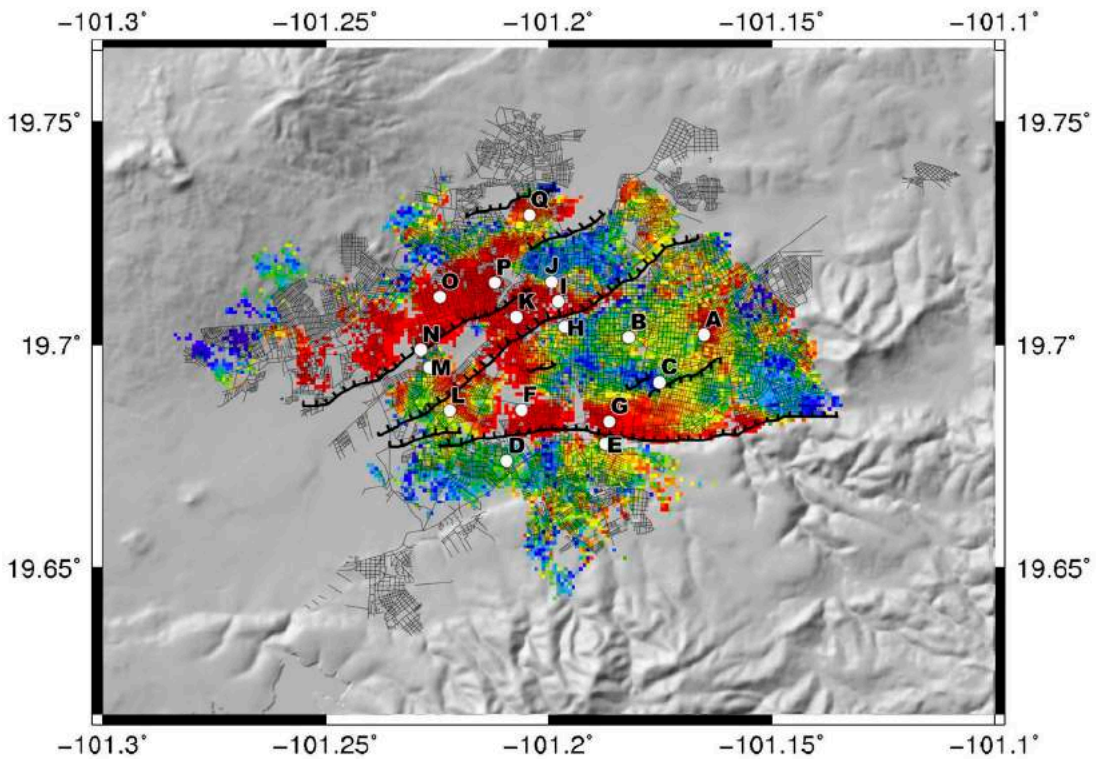

Figure 5. The map shows the location of the points in the city of Morelia for which a time series was estimated in the inversion process. The color scale indicates the correlation coefficient of the pixels used in the time series. Warm colors (red) show a high correlation and the colder tones (blue and purple) indicate areas of low correlation. The points selected to construct the time series were chosen, whenever possible, in areas of relatively large correlation.

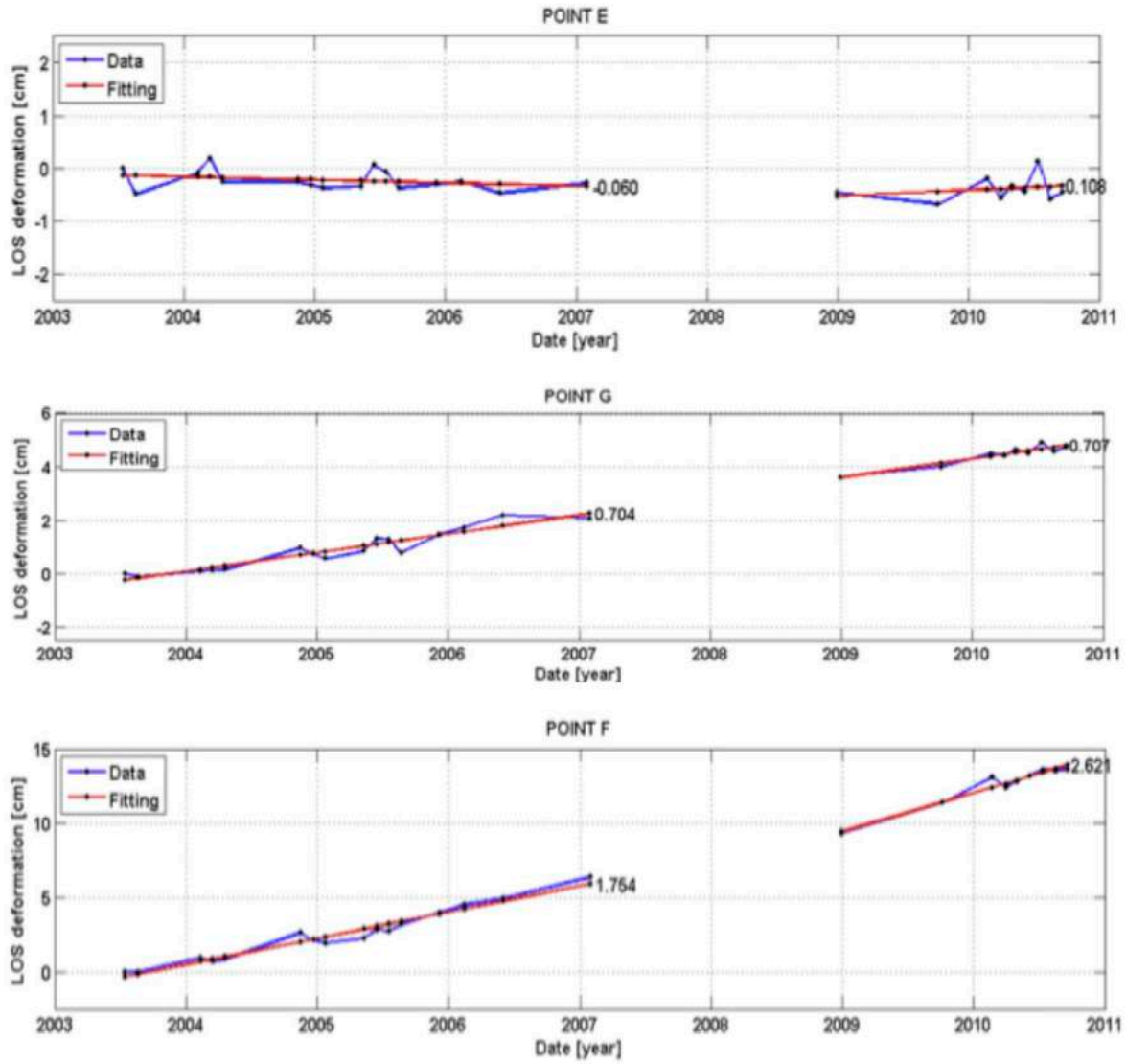

Figure 6. Time series for points E, G and F located in the vicinity of La Paloma fault (Figures 1 and 4). The solid blue line indicates the ground deformation estimated from the inversion process of the InSAR images in Line of Sight (LOS) of the satellite. The solid red line indicates the best linear fit of the deformation model; the numbers indicate the average annual subsidence rate.

Subsidence near Central Camionera fault

Subsidence time histories were estimated for several locations and for six cross sections in the vicinity of the Central Camionera fault. As in the case of La Paloma fault, the cross sections indicate great variability of the ground subsidence rates along the strike of the fault (see the Electronic Supplement). Point H lies on the hanging wall of the Central Camionera fault and shows no appreciable subsidence during the time covered (Figure 8). The area called Prados Verdes (point I on Figure 5) is on the footwall of the fault. This area shows the largest ground subsidence rate observed in the city (Figure 8). During the first period of observation, point I shows a relatively low rate of subsidence (Figure 8). During this time, the water well located in the vicinity of this area was not operational due to the installation of new casing. The bore diameter was increased from 96 to 102 m (Cigna *et al*., 2012). The drastic increase of subsidence, going from 1.2 to 4.4 cm/yr during the second observational period (Figure 8), is presumably related to the increase of the water extraction rate and a

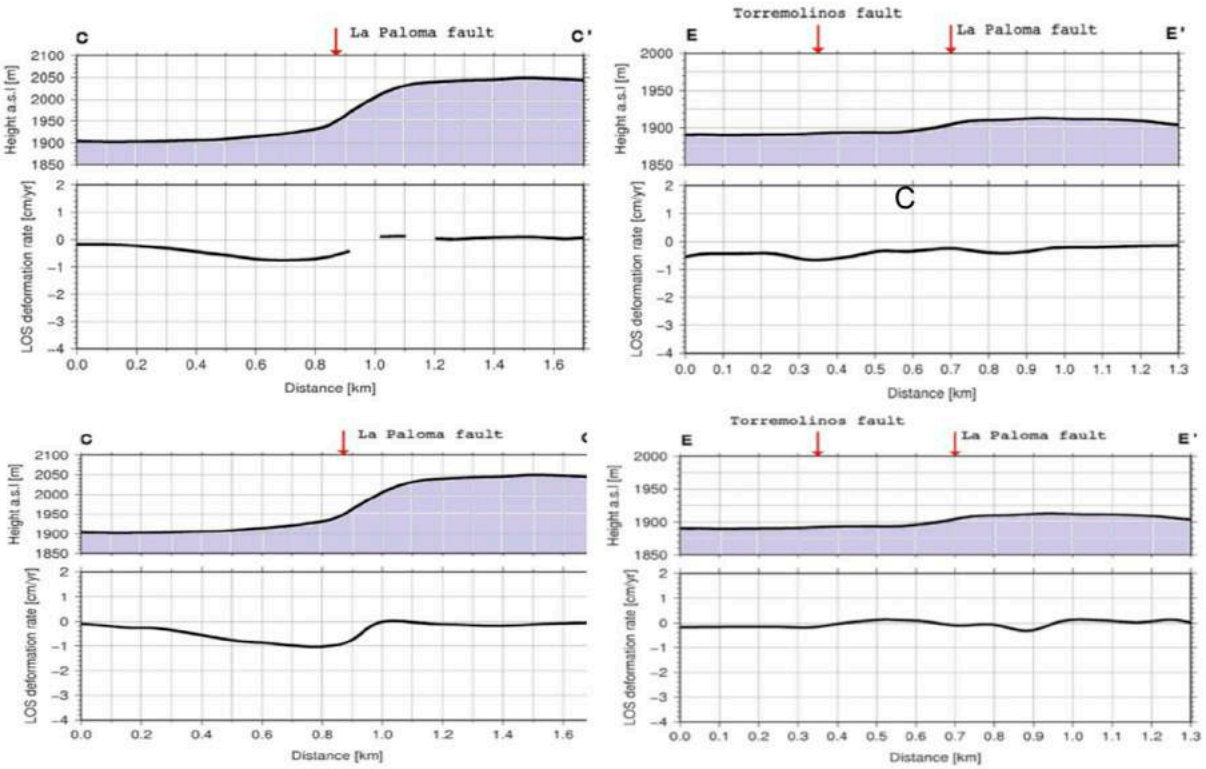

Figure 7. Cross sections CC´and DD´ across La Paloma fault as shown on Figure 4. The topography is shown on top and the deformation of the ground estimated from InSAR is shown at the bottom. The upper image of each cross section depicts the period from 2003 to 2007; the lower pane reflects deformation from 2008 to 2010.

further reduction of the static level of the well (Cigna *et al*., 2012). To the west of the Prados Verdes area, point K, also on the footwall of the Central Camionera fault, shows a stable and linear rate of subsidence of approximately 1 cm/yr.

Six cross sections were calculated across the Central Camionera fault. In the central part of the fault, on cross section II', there is a clear change in the subsidence rate on both sides of the fault. Along this cross section, the variation in the rates of subsidence, observed also in point I, is clearly evident (Figure 9). This rapid change in the rate of subsidence is probably due also to the increase in production of Prados Verdes well. In the eastern part of the fault (Section HH') there is no discernable ground deformation during the seven years of the study (Figure 9). A similar result is observed also in cross section LL' (see the Electronic Supplement). The gaps observed in cross sections HH´and II´ are due to points on the ground where coherence was lost and where the RMS values were above the prescribed levels of quality.

Subsidence in the footwall of La Colina fault

In the area near La Colina fault, several locations were selected to calculate the variation of subsidence as a function of time. Points N and P, on the hanging of the fault, show a very similar subsidence behavior. In the first three years of observation, the subsidence in both cases ranged from 1.7 cm/yr in Point N, to 1.8 cm/yr in Point P (Figure 10). From 2009 to 2010, the subsidence rate increased to almost 3 cm/yr in point P and to 2 cm/yr in Point N, again showing an increase in the subsidence rate of the ground in the second period studied. In all cases, however, the behavior is linear, showing no temporal or seasonal variations. Point O is also in the footwall of La Colina Fault. However, this location is farther away from the fault trace than points N and P. The average rate of subsidence is slower than in the previous two locations, showing an average subsidence of between 0.6 and 0.8 cm/yr (Figure 10).

Two cross sections were calculated crossing La Colina fault (cross sections NN' and OO´ (Figure 11). Cross sections NN´ and OO´ show

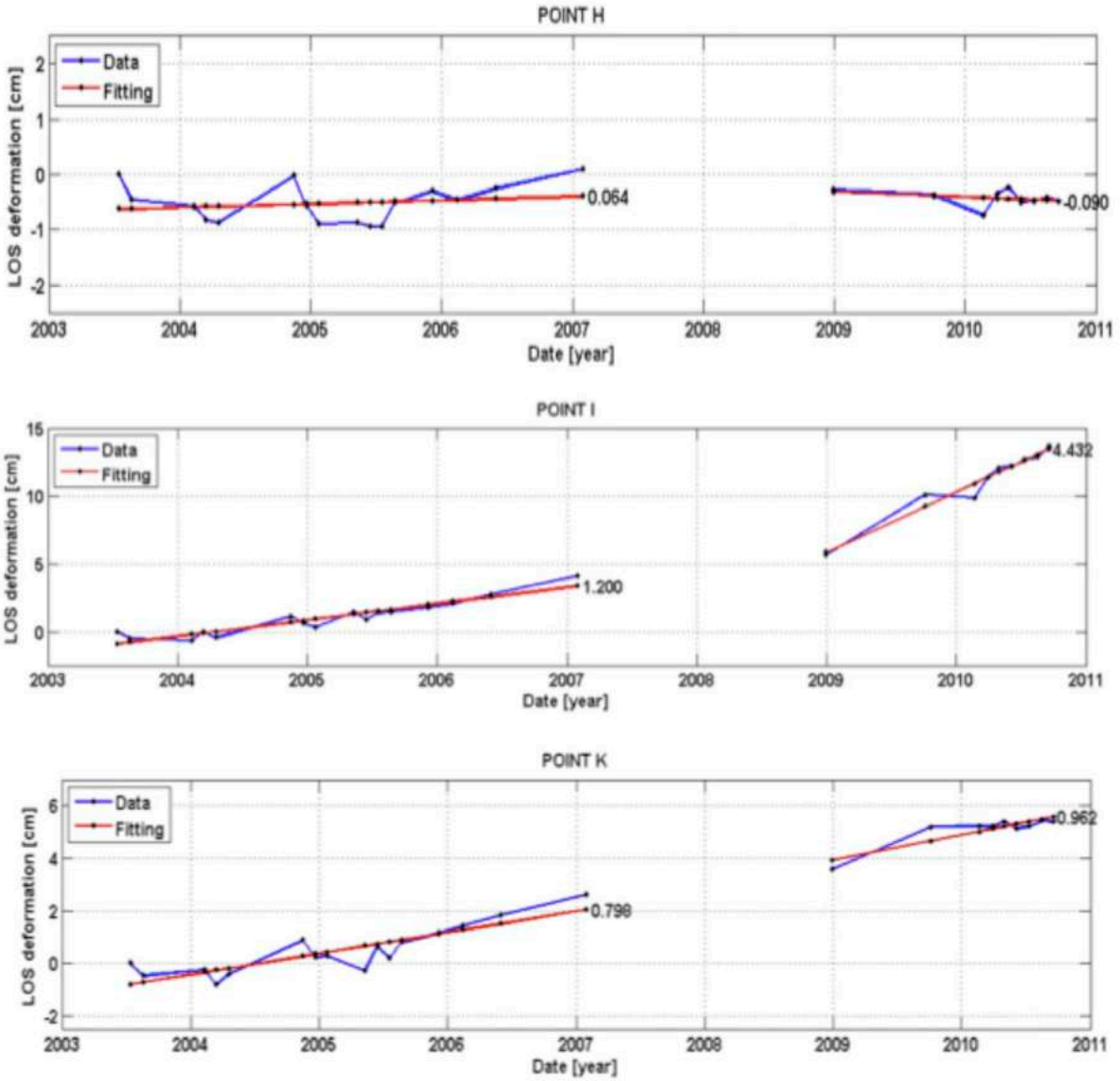

Figure 8. Time series for points H, I and K located in the vicinity of the Central Camionera fault (Figure 5). The solid blue line indicates the ground deformation estimated from the inversion process of the InSAR images in Line of Sight (LOS) of the satellite. The solid red line represents the best linear fit of the deformation model; the numbers indicate the average annual subsidence rate.

subsidence of the ground to the north of the surface expression of La Colina fault. In both cases, a broad area subsides at a maximum rate of approximately 2 to 2.5 cm/yr. The deformation of the ground stops to the north of the city, where the Pliocene basalt and andesite deposits delineate the northern boundary of the Morelia basin (Figure 11). The deformation rate on these two cross sections remains constant during the two periods studied. In both cases, some coherence is lost in the central part of the cross sections.

Summary and conclusions

A new analysis of ground subsidence in the city of Morelia, in central Mexico, is presented using the small baselines methodology to estimate interferograms. The purpose of this work is to extend the work done by Cigna *et al*. (2011; 2012) in mapping the ground subsidence in the city. The identification of the areas of the city where subsidence occurs and the estimation of subsidence rates in various locations is important to mitigate and predict the locations

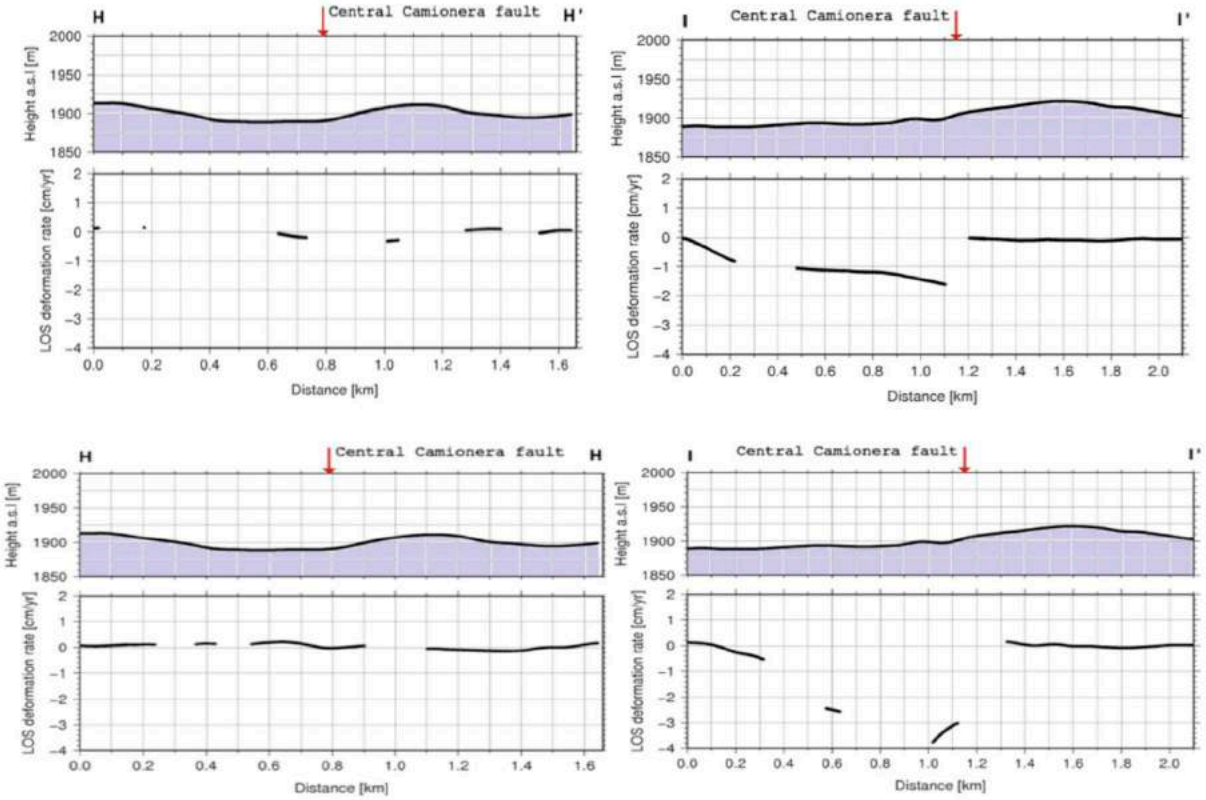

Figure 9. Cross sections HH´ and II´ across the Central Camionera fault as shown on Figure 4a. The topography is shown on top and the deformation of the ground estimated from InSAR is shown at the bottom. The upper image of each cross section depicts the period from 2003 to 2007; the lower pane reflects deformation from 2008 to 2010.

of the city that will be more prone to damage and ground faulting in the future.

From a regional point of view, most of the city of Morelia shows no significant subsidence. In fact, there is no deformation observed on many of the mapped faults, such as the Chapultepec, Cuautla and Torremolinos. The subsidence evidenced by the InSAR observations is concentrated in the western half of the city and along three major faults: La Paloma, Central Camionera and La Colina. However, the ground deformation is not continuous and homogeneous along these faults. Subsidence takes place only on specific locations along the footwall of these three faults. La Colina fault is the one that exhibits a more continuous deformation of the ground along strike.

The largest subsidence rate of 4 cm/yr is observed to the north of the central part of the Central Camionera fault. This region showed a rapid increase in subsidence from 2009 to 2010, probably due to the increased flow of Prados Verdes well. In general, however, there is no direct correlation between the rates of water extraction and the areas of larger subsidence. In the same manner, as observed by Cigna *et al*. (2012), there is no clear correlation between the thickness of the Quaternary sediments in different parts of the Morelia basin and the rate of subsidence.

Garduño Monroy *et al*. (2001) suggested that the ground deformation in the city of Morelia is the surface expression of motion on subsurface basement faults. These authors suggest that these buried faults are continuously deforming by aseismic creep. These authors attribute the presence of surface deformation of the ground as a reflection of the motion on basement faults beneath the sediments, caused by creep at depth. However, the rates of subsidence observed on the ground are of several cm/yr. The rates of subsidence observed in Morelia

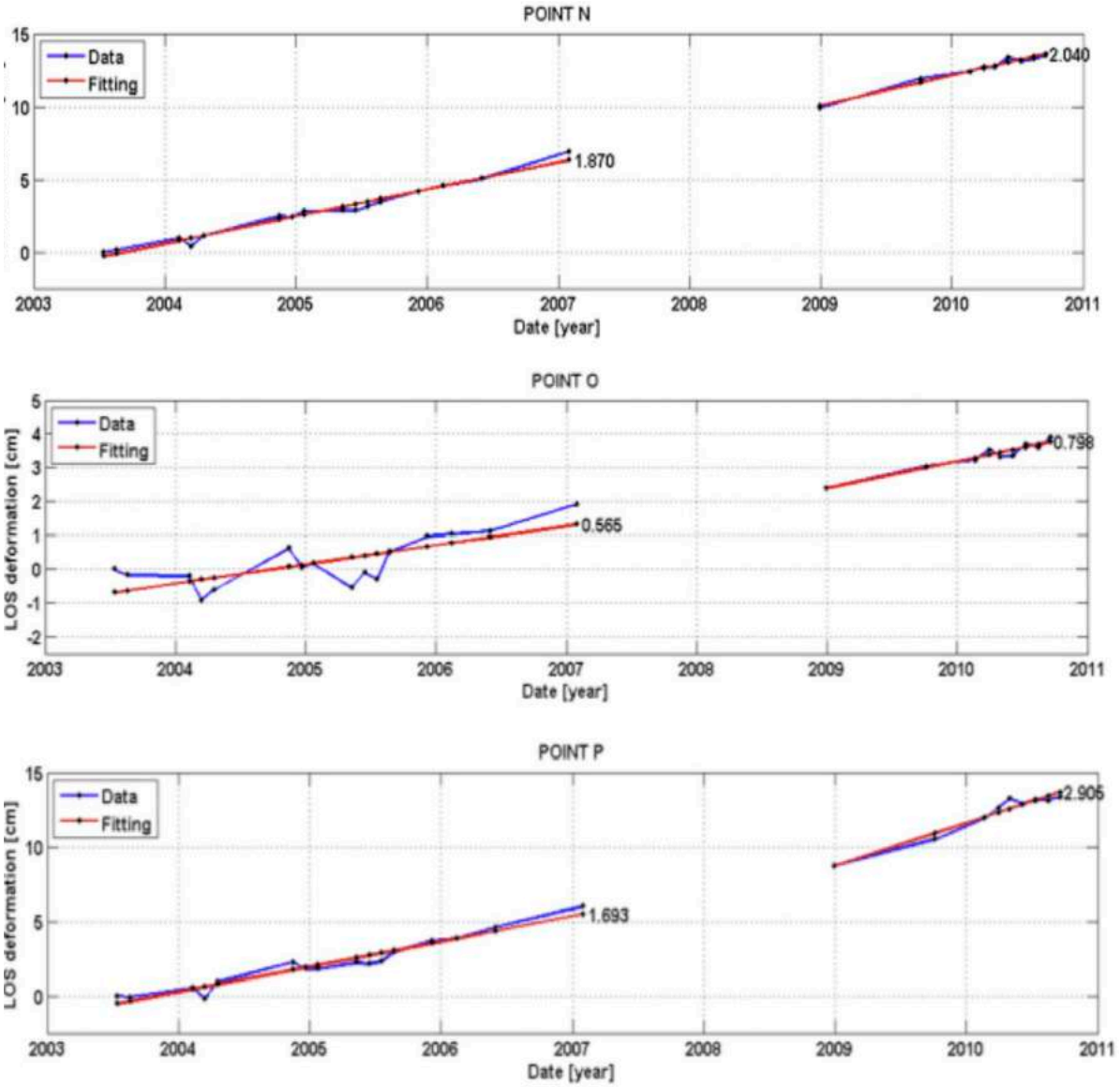

Figure 10. Time series for points N, O and P located in the vicinity of La Colina fault (Figure 5). The solid blue line indicates the ground deformation estimated from the inversion process of the InSAR images in Line of Sight (LOS) of the satellite. The solid red line indicates the best linear fit of the deformation model; the numbers indicate the average annual subsidence rate.

are almost an order of magnitude larger than creep deformation measured on active faults. For example, fault creep observed on San Andreas is in the order of mm/yr (*e.g.,* Schulz *et al.*, 1982; Lienkaemper *et al*., 2001; Lyons and Sandwell, 2003). Thus slow aseismic creep motion on subsurface faults would not explain the large subsidence rates observed in the Morelia basin.

The ground subsidence observed in the city of Morelia is highly variable in areal extent and concentrated in specific areas. The lack of direct correlation between subsidence of the ground and water extraction and the thickness of the sediments suggests that the deformation of the ground is due to the preexisting topography of the basement that controlled the complex depositional history of volcanic and lacustrine deposits in the Morelia basin. This poses a challenge to manage the exploitation of the aquifer in order to minimize and control the ground deformation.

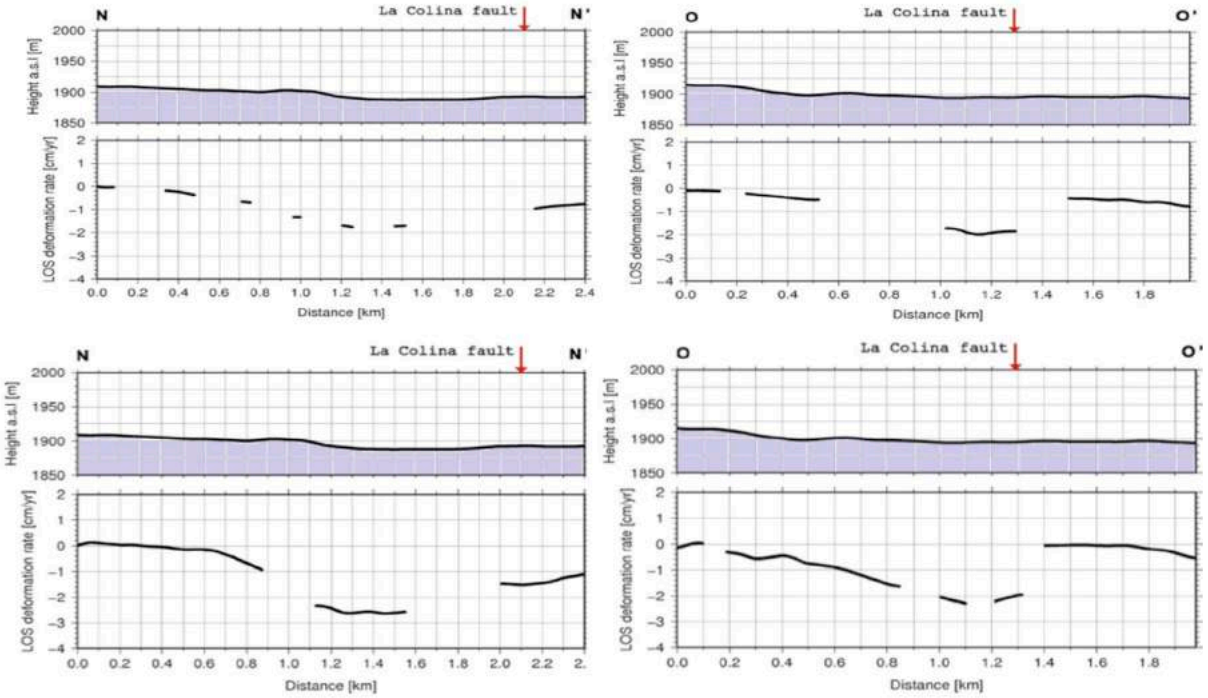

Figure 11. Cross sections NN´and OO´ across La Colina fault as shown on Figure 4a. The topography is shown on top and the deformation of the ground estimated from InSAR is shown at the bottom. The upper image of each cross section depicts the period from 2003 to 2007; the lower pane reflects deformation from 2008 to 2010.

References

Aguirre-Díaz, G. J., Zúñiga-Dávila- Madrid, F. R., Pacheco-Alvarado.F. J., Guzmán-Speziale, M., and Nieto-Obregón, J., 2000. El graben de Querétaro, México. Observaciones de fallamiento activo. *GEOS,* 20, 1, 2-7.

Amelung, F., Galloway, D. L., Beii, J. W., Zebker, H. A., and Laczniak, R. J., 1999. Sensing the ups and downs of Las Vegas: InSAR reveals structural control of land subsidence and aquifer-system deformation. *Geology,* 27, 6, 483-486.

Arreygue-Rocha, E., Garduño-Monroy, V. H., Canuti, P., Casagli, N., Lotti, A., and Chiesa, S., 2002. Análisis geomecánico de la inestabilidad del escarpe La Paloma en la Ciudad de Morelia, Michoacán, México. *Revista Mexicana de Ciencias Geológicas,* 19, 2, 91-106.

Arreygue-Rocha, E., Garduño-Monroy, V. H., Canuti, P., Casagli, N., and Lotti, A., 2005. Riesgos geomorfólogicos e hidrológicos en la Ciudad de Morelia, Michoacán, México. *Geotermia,* 18, 1, 26-35.

Ávila-Olvera, J. A., and Garduño-Monroy, V. H., 2006. Hundimientos ocasionados por Procesos de Subsidencia-Creep-Falla (PSCF) en la ciudad de Morelia, Mich., México. *Geotermia,* 19, 2, 50-59.

Ávila-Olvera, J. A., 2008. Evolución de los procesos de subsidencia-creep-falla, casos: Morelia, Mich. and Celaya, Gto. UNAM, Tesis, 249 pp.

Ávila-Oiivera, J. A., and Garduño-Monroy, V. H., 2008. A GPR study of subsidence creep-fault process in Morelia, Michoacán, Mexico. *Engineering Geology,* 100,69-81.

Ávila-Olvera, J. A., Farina, P., and Garduño-Monroy, V. H., 2010. Land subsidence monitored by satellite interferometry in Mexican cities. *IAHS Pub.* 339, 316-318.

Berardino, P., Fomaro, G., Lanari, R., and Sansosti, E., 2002. A new algorithm for surface deformation monitoring based on Small Baseline differential SAR Interferograms. *IEEE Transactions on Geoscience and Remote Sensing,* 40, 11, 2375-2383.

Buckley, S. M., Rosen, P. A., Hensley, S., and Tapley, B. D., 2003. Land subsidence in Houston, Texas, measured by radar interferometry and constrained by extensometers. *Journal of Geophysical Research,* 108,811, 2542, 1-18.

Cabral-Cano, E., Dixon, T. H., Miralles-Wilhelm, F., Diaz-Molina, O., Sánchez-Zamora, 0., and Carande, R. E., 2008. Space geodetic imaging of rapid ground subsidence in Mexico City. *Geological Socíety of America Bulletin,* 120, 1556-1566.

Cabral-Cano, E., Arciniega-Ceballos, A., Díaz-Molina, O., Cigna, F., Ávila-Oiivera, A., Osmanoglu, B., Dixon, T., DeMets, C., Garduño-Monroy, V. H., Vergara-Huerta, F., and Hernández-Quintero, J. E., 2010. Is there a tectonic component to the subsidence process in Morelia, Mexico?, *IAHS Publication* 339, 164-169.

Calderhead A., Therrien, R., Rivera, A., Martel, R., and Gañias, J., 2011. Simulating pumping-induced regional land subsidence with the use of lnSAR and field data in the Toluca Valley, Mexico. *Advances in Water Resources,* 34, 83-97.

Carreón-Freyre, 0., and Cerca, M., 2006. Delineating the near-surface geometry of the fracture system affecting the Valley of Querétaro, Mexico: Correlation of GPR signatures and physical properties of sediments. *Near Surface Geophysics,* 49-55.

Carreón-Freyre, D., Hidalgo-Moreno, C.M., and Hemández-Marín, M., 2006. Mecanismos de fracturamiento de depósitos arcillosos en zonas urbanas. Caso de deformación diferencial en Chalco, Estado de México. *Boletín de la Sociedad Geológica Mexicana,* Número Especial de Geología Urbana, LVIII, 2, 237-250.

Carrillo, N., 1948. lnfluence of artesian wells on the sinking of México City, in Volume: Nabor Carrillo, "El hundimiento de la Ciudad de México y el Proyecto Texcoco. Comisión Impulsora y Coordinadora de la Investigación Científica Anuario 47: 7-14.

Castañeda, M. H., Murillo-Méndez, M. A., Fuentes-López, *J.* A., and Monsiváis-Santoyo, J. P., 1993. Levantamiento cartográfico de las fallas y facturas geológicas de la ciudad de Aguascalientes. *Revista Investigación y Ciencia de la UAA,* 9, 43-47.

Castañeda, M. H., Murillo-Méndez, M. A., Fuentes-López, J. A., and Monsiváis-Santoyo, J. P., 1995. Comentarios al estudio de fallas y fracturas geológicas de la ciudad de Aguascalientes. Mecanismo de fracturamiento. *Revista Investigación y Ciencia de la UAA,* 14, 40-43.

Cavalié. 0., Doin, M. P., Lasserre, C., and Briole, P., 2007. Ground motion measurement in the Lake Mead area, Nevada, by differential synthetic aperture radar interferometry time series: probing the lithosphere rheological structure. *Journal of Geophysical Research,* 112, 803403, 1-18.

Chai, J . C., Shen, S. L., Zhu, H. H., and Zhang, X. L., 2004. Land subsidence due to groundwater drawdown in Shanghai. *Géotechnique,* 54, 2, 143-147.

Chaussard, E., Wdowinski, S., Cabral-Cano and E., Amelung, F., 2014, Land subsidence in central Mexico detected by ALOS InSAR time-series, *Remote Sensing of Environment*, 140, 94-106, ISSN 0034-4257, https://doi.org/10.1016/j.rse.2013.08.038.

Chávez-Alegría, 0., 2008. Modelación física experimental del fenómeno de subsidencia. Universidad Autónoma de Querétaro. Tesis, 151 pp.

Cigna, F., Cabral-Cano, E., Osmanoglu, B., Dixon, T. H., and Wdowinski, S., 2011. Detecting subsidence-induced faulting in Mexican urban areas by means of persistent scatterer interferometry and subsidence horizontal gradient mapping. *IGARSS,* 2125-2128.

Cigna, F., Osmanoglu, B., Cabral-Cano, E., Dixon, T. H., Ávila-Olivera, J. A., Garduño-Monroy, V. H., DeMets, C., and Wdowinski, S., 2012. Monitoring land subsidence and its induced geological hazard with Synthetic Aperture Radar lnterferometry: A case study in Morelia, Mexico. *Remote Sensing of Environment,* 117, 146-161.

Dehghani, M., Zoej, M. J. V., Entezam, Mansourian, A., and Saatchi, S., 2009. lnSAR monitoring of progressive land subsidence in Neyshabour, northeast Iran. *Geophys. J. lnt.,* 178, 47-56.

Ding, X. l., Liu, G.X., Li, Z.W., Li, Z.L and Chen, Y. Q., 2004. Ground subsidence monitoring in Hong Kong with satellite lnterferometry. *Photogrammetric Engineering and Remote Sensing,* 70, 10, 1151-11156.

Esquivel, R. R., 2009. Análisis y modelado de deformaciones locales de la corteza terrestre con radar de apertura sintética y datos geodésicos. Tesis, UNAM, 105 pp.

Farina, P., Ávila-Olivera, J. A., and Garduño-Monroy, V. H., 2007. Structurally-controlled urban subsidence along the Mexican volcanic belt (MVB) monitored by lnSAR. *Envisat Symposium.* Montreux, Switzerland.

Farina, P., Avila-Olivera, J. A., Garduño-Monroy, V. H., and Catani, F., 2008. DlnSAR analysis of differential ground subsídence affecting urban areas along the Mexican Volcanic Belt (MVB). *Rivista italiana di Telerilevamento,* 40(2), 103-113.

Farr, T. G., and Kobrick, M., 2000. Shuttle Radar Mission produces a wealth of data. *American Geophysical Union, EOS*, 81,48, 583-585.

Ferreti, A., Pratti, C., and Rocca, F., 2000. Nonlinear subsidence rates estimation using permanent scatters in differential SAR interferometry. *IEEE Transactions on Geosciences and Remote Sensing,* 39 (5), 2202-2212.

Ferretj A., Pratti, C., and Rocca, F., 2001. Permanent Scatterers in SAR lnterferometry. *IEEE*, *Transactions Geosciences and Remote* Sensing, 39, 1, 8-20.

Garduño-Monroy, V. H., Arreygue-Rocha, E., lsrade-Aicántara, and Rodrlguez-Torres, G. M., 2001. Efectos de las fallas asociadas a la sobrexplotación de acuíferos y la presencia de fallas potencialmente sísmicas en Morelia, Michoacán, México. *Revista Mexicana de Ciencias Geológicas,* 18, 37-54

Gayol, R., 1925. Estudio de las perturbaciones que en el fondo de la Ciudad de México ha producido el drenaje de las aguas del subsuelo, por las obras del desagüe y rectificación de los errores a que ha dado lugar una incorrecta interpretación de los efectos producidos: *Revista Mexicana de Ingeniería y Arquitectura,* v. 111, 96-132.

Goldstein, R. M. and Wemer, C. L., 1998. Radar interferogram filtering for geophysical applications. *Geophysical Research Letters,* 25, 21,4035-4038.

Goldstein, R.M., Zebker, H.A., and Wemer, C. L., 1988. Satellite radar interferometry: Two-dimensional phase unwrapping. *Radio Science,* 23, 4, 713-720.

Hanssen, R. F., 2001. Radar interferometry: data interpretation and error analysis. *Kluwer Academíc Publíshers,* 308 pp.

Le Mouélic, S., Raucoules, D., Carmec, C., and King, C., 2005. A Least Squares adjustment of multi-temporal lnSAR data: Application to the ground deformation of Paris. *Photogrammetric Engineering and Remote Sensing,* 17, 2, 197-204.

Lienkaemper, J. J., Galehouse, J. S. and Simpson, R. W. (2001). Long-term monitoring of creep rate along the Hayward fault and evidence for a lasting creep response to 1989 Loma Prieta earthquake. *Geophys. Res. Lett*, *28*(11), 2265-2268.

López-Doncel, R., Mata-Segura, J. L., Cruz-Márquez, J., Arzate-Fiores, J., and Pacheco-Martínez, J., 2006. Riesgo geológico para el patrimonio histórico. Ejemplos del centro histórico de la ciudad de San Luis Potosí. *Boletín de la Sociedad Geológica Mexicana,* Número Especial de Geología Urbana, LVIII, 2, 259-263.

López-Quiroz, P., 2008. Séries temporelles de la subsidence de la ville de Mexico obtenues par interférométrie radar. TELECOM, ParisTech, Tesis doctoral, 140 pp.

López-Quiroz, P., Doin, M. P., Tupin, F., Briole, P., and Nicolas, J. M., 2009. Time series analysis of Mexico City subsidence constrained by radar interferometry. *Journal of Applied Geophysics,* 69, 1-15.

Lu, L., and Liao, M., 2008. Subsidence measurement with PS-InSAR techniques in Shanghai urban. *The Intematíonal Archives of the Photogrammetry, Remote Sensing and Spatial lnformation Science,* XXXVII, 173-178.

Lyons, S. and Sandwell, D. (2003). Fault creep along the southern San Andreas from interferometric synthetic aperture radar, permanent scatterers, and stacking. *Journal of Geophysical Research: Solid Earth*, *108*(B1).

Marfai, M. A., and King, L., 2007. Monitoring land subsidence in Semarang, Indonesia. *Environmental Geology.,* 53, 651-659.

Mejía-Gómez, J. A., and Sandoval-Minero, R., 2004. Uso del agua subterránea en la region acuífera lrapuato-Valle de Santiago (México) y su impacto sobre el sistema hidrogeológico. *Boletín Geológico y Minero,* 115, 311-318.

Ortega-Guerrero, A., Cherry, J. A., and Rudolph, D. L., 1993. Large-Scale Aquitard Consolidation near, Mexico City. *Ground Water,* 31, 5, 708-718.

Osmanoglu, B., Dixon, T. H., Wdowinski, S., Cabral-Cano, E., and Jiang, Y., 2011. Mexico City subsidence observed with persistent scatterer lnSAR. *International Journal of Applied Earth Observation and Geoinformation,* 13. 1-12.

Pacheco-Martínez, J., 2007. Modelo de subsidencia del valle de Querétaro y predicción de agrietamientos superficiales. UNAM, Tesis, 224 pp.

Pacheco-Martínez, J., and Arzate-Flores, J., 2007. Análisis multicapa de la subsidencia en el Valle de Querétaro, México. *Revista Mexicana de Ciencias Geológicas,* 24, 3, 389-402.

Pacheco-Martínez, J., Arzate, J., Rojas, E., Arroyo,M., Yutsi, V., and Ochoa, G., 2006. Delimitation of ground failure zones due to land subsidence using gravity data and finite element modeling in the Querétaro valley, México. *Engineering Geology,* 84, 143-160.

Poland, J. F., 1984. Guidebook to studies of land subsidence due to groundwater withdrawal, prepared for the International Hydrogeological Programme, Working Group 8.4. UNESCO, Book Crafters, Chelsea, Massachusetts.

Rosen, P.A., Hensley, S., Peltzer, G., and Simons, M., 2004. Updated repeat orbit interferometry package released. *EOS Transactions AGU*, 85, 5, 47.

Schmidt, D. A., Bürgmann, R., 2003. Time-dependent land uplift and subsidence in the Santa Clara valley, California, from a large interferometric synthetic aperture radar data set. *Journal of Geophysical Research*, 108, 89, 2416, 1-13.

Schroeder-Aguirre, A. A., 2010. Análisis de la deformación del fallamiento por subsidencia en la zona de lrapuato, Gto, UNAM, Tesis, 111 pp.

Schulz, S. S., Mavko, G. M., Burford, R. O., and Stuart, W. D. (1982). Long-term fault creep observations in central California. *Journal of Geophysical Research: Solid Earth*, 87(B8), 6977-6982.

Stramondo, S., Bozzano, F., Marra, F., Wegmüller, U., Cinti, F. R., Moro, M., and Saroli, M., 2008. Subsidence induced by urbanization in the city of Rome detected by advanced lnSAR technique and geotechnical investigations. *Remote Sensing of Environment*, 112, 3160-3172.

Strozzi, T., and Wegmüller, U., 1999. Land subsidence in Mexíco City mapped by ERS Differential SAR lnterferometry. Geoscience and Remote Sensing Symposium. /GARSS'99 Proceedings, IEEE, 4, 1940-1942.

Strozzi, T., Wegmüller, U., Tosi, L., Bitell, G., and Spreckels, V., 2001. Subsidence monitoring with differential SAR lnterferometry. Photogrammetric Engineering and Remote Sensing, 67, 11, 1261-1270.

Trujillo-Candelaria, J. A., 1989. Fallamientos de terrenos en Celaya, Gto. Academia Mexicana de Ingeniería. *Alternativas Tecnológicas*, 29, 367-369.

Trujillo-Candelaria, J.A., 2009. Fallamientos de terrenos por sobrexplotación de acuíferos en Celaya, Gto., Aquaforum, 52, 24-27.

Usai, S., 2003. A least squares database approach for SAR lnterferometric data. *IEEE Transactíons on Geoscience and Remote Sensing*, 41, 4, 753-760.

Vargas, R. M. V., 1999. La subsidencia y su problemática en la ciudad de Celaya, Guanajuato. UNAM, Tesis, 144 pp.

Vilardo, G., Ventura,G., Terranova, C., Matano, F., and Nardó, S., 2009. Ground deformation due to tectonic, hydrothermal, gravity hydrogeological and anthropic processes in the Campania Region (Southem ltaly from Permanent Scatterers Synthetic Aperture Radar lnterferometry, *Remote Sensing of Envíronment*, 113, 197-212.

Watson, K. M., Bock, Y., and Sandwell, D. T., 2002. Satellite interferometric observations of displacements associated with seasonal groundwater in the Los Angeles basin. *Journal of Geophysical Research*, 107, B4, 1-17.

Yan, Y., López-Quiroz, P., Doin, M. P., Tupin, F., and Fruneau, B., 2009. Comparison of two methods in multi-temporal differential SAR Interferometry: Application to the measurement of Mexico City subsidence. MultiTemp 2009 -The Fifth International Workshop on the Analysis of Multi-temporal. Remote Sensing Images, Groton, Connecticut.

Zermeño de León, M. E., Mendoza-Otero, E., y Calvillo-Silva, G., 2004. Medición del hundimiento y modelo para estudiar el agrietamiento de la ciudad de Aguascalientes. Revista Investigación y Ciencia de la UAA, 31, 35-40.

Zermeño de León, M. E., Esquivel-Ramírez, R., Hemández-Navarro, A., Mendoza-Otero, E., and Arellano-Sánchez, J., 2005. Influencia de la extracción del agua en la subsidencia y agrietamiento de la ciudad de Aguascalientes. *Revista Investigación y Ciencia de la UAA*, 32, 15-22.

Appendix A

Orbital and stratified atmospheric correction:

Equation 1 was adjusted (Cavalié *et al*., 2007; López-Quiroz *et al*., 2009):

$$\phi_0 = (ax+b)y + cx + d + \phi z \text{ for } z > 1930m \quad (1)$$

where a, b, c, $d\phi$ are obtained using least square minimization. And z is the elevation where the deformation is concentrated and obtained by permorfing a linear regression between the interferometric phase and the elevation.

Inversión process

The phase delay time series were obtained using a least squares inversion (Cavalié *et al*., 2007) solving the linear equation:

$$d_l = G_l\, m_l \quad (2)$$

where, d_l is the vector including the data of interferometric phase from N_l interferograms for pixel, l; m_l, is a vector including the phase delay increments between two successive images; G_l is a matrix of zeros and ones, constructed based on the fact that the phase of an interferogram (ϕ_{ij}^l), is the sum of the successive phase delays between images i and j:

$$\phi_{ij}^l = \sum_{k=i}^{j-1} m_k^l \quad (3)$$

RMS estimate in the case of pixels (Cavalié *et al*., 2007):

$$\phi RMS_{pixel}^l = \frac{1}{N_l} \sum N_l \left(\phi_{ij}^l - \sum_{k=i}^{j-1} m_k^l \right)^2 \quad (4)$$

RMS of each interferogram (Cavalié *et al*., 2007):

$$\phi_{RMS_{ifg}}^{ij} = \frac{1}{p} \sum l \left(\phi_{ij}^l - \sum_{k=i}^{j-1} m_k^l \right)^2 \quad (4)$$

Geofísica Internacional (2018) 57-1: 59-65

Original paper

Ionospheric response to Huge Gas Explosion in Kaohsiung City, Taiwan, on July 31, 2014

Jyh-Woei Lin

Received: September 07, 2016; accepted: November 14, 2017; published on line: January 01, 2018

Resumen

En este trabajo se utilizó el Análisis de Componente Principal Bidimensional (2DPCA) para determinar la anomalía de contenido total de electrones (TEC) utilizando el eigenvalor principal de 2DPCA como indicador matemático en la respuesta de la ionósfera a la gran explosión de gas ocurrida en la ciudad de Kaohsiung (Taiwan) a las 15:59 (TU) del 31 de julio de 2014. 2DPCA provee una cuidadosa descripción del manejo de los datos. Los resultados mostraron que se observa una anomalía TEC sobre Taiwan de las 16:00 a las 16:05 (TU). Las ondas de choque acústicas causaron una anomalía TEC detectable sin considerar el estatus atmosférico y la transmisión de las ondas acústicas TEC fue de, por lo menos, 5 minutos.

Palabras clave: Análisis bidimensional de componente principal (2DPCA), contenido total de electrones (TEC), gran explosión de gas en la iudad de Kaohsiung, ondas de choque acústicas.

Abstract

In this paper the two-dimensional Principal Component Analysis (2DPCA) was used to determine the total electron content (TEC) anomaly using the principal eigenvalue of 2DPCA as a mathematical indicator in the ionospheric response to the huge gas explosion in Kaohsiung city (22°36’39”N 120°19’8”E), Taiwan at 15: 59 (UT) on July 31, 2014. 2DPCA has been shown to be sensitive to detect weak TEC anomalies. 2DPCA gives a careful data handling description. Results have shown that a TEC anomaly over Taiwan was observed from 16:00 to 16:05 (UT). The acoustic shock waves have caused a TEC anomaly detectable without considering the atmosphere situation and traveling of acoustic shock waves during this explosion. The duration time of the TEC anomaly was at least 5 minutes.

Key words: Two-dimensional principal component analysis (2DPCA), total electron content (TEC), huge gas explosion, Kaohsiung City, acoustic shock waves.

Jyh-Woei Lin
Department of Electrical Engineering
Southern Taiwan University of Science and Technology
No. 1, Nan-Tai Street, Yungkang Dist.
Tainan City, Taiwan,
*Corresponding author: pgjwl1966@gmail.com

Introduction

One of the potential area of application of this paper correspond to explosion related ionospheric anomalies. Jones and Spracklen (1974) found an explosion occurred on first of, June, 1974, at the Nypro plant at Flixborough, Lincolnshire, that produced a blast wave which crossed the atmosphere and penetrated into the ionosphere. Blanc and Jacobson (1989) described ionospheric anomalies as caused through the acoustic shock wave produced by a 5-kt chemical explosion. Andreeva *et al*. (2001) work used the ionosphere radiotomography method to detect the long-lived local disturbances of the ionospheric density over the site of ground industrial explosions. Calais *et al.* (1998) found an ionospheric signature of surface mine blasts from Global Positioning System (GPS) receivers. The perturbation started 10 to 15 min after the blast, and lasted for about 30 minutes. The goal of this paper is to use Two-Dimensional Principal Component Analysis (2DPCA) to examine the ionospheric spatial distribution of any driven TEC anomaly associated with huge gas explosion in Kaohsiung (22°36′39″N 120°19′8″E), Taiwan at 15: 59 (UT) on July 31, 2014, without considering the atmosphere environment during this explosion but only the two-dimensional Total Electron Content (TEC) data. The sample time interval chosen was 16:00 to 16:10 (UT). The two-dimensional TEC data are derived from NASA Global Differential GPS system (GDGPS) and the global TEC maps (GIMs) are derived using TEC data from ~100 real-time GDGPS tracking sites with a time resolution of 5 minutes (Kechine *et al*., 2004; Ouyang *et al*., 2008).

Method

2DPCA

2DPCA signals are represented by a matrix A (n x m dimension). Linear projection of the form is considered as follows (Sanguansat, 2012),

$$y = Ax \tag{1}$$

where x is an n dimensional projection axis and y is the projected feature of signals on x, called principal component vector.

$$S_x = E(y-Ey)(y-Ey)^T \tag{2}$$

Here S_x is the covariance matrix of the projected feature vector.

The trace of S_x is defined as:

$$J(x) = tr(S_x) \tag{3}$$

$$tr(S_x)=tr\{x^TGx\}, \text{ where } G=E[(AEA)(AEA)] \tag{4}$$

matrix G is thed signal covariance matrix. The vector x maximizing Eq.4 corresponds to the principal (largest) eigenvalue of G, and let the principal eigenvalue to be the most dominant component of the data, therefore the principal eigenvalue is a mathematical indicator representing the principal (main) characteristics of the data. Small signal size (SSS) problem (sparse data in a matrix) of two dimensional TEC data can be removed by 2DPCA (Sanguansat, 2012). The Principal Component Analysis (PCA), converts the measurements into one-dimensional data before covariance matrix calculation. The covariance matrix of PCA is based on an input matrix with *m x n* dimension, of which is reshaped from one-dimensional data (length of m multiplying n). Reshaping data will cause a computing error since PCA is a tool to deal with one-dimensional data. It means that the spatial structure and information can not be well preserved due to some original information loss when inverting to original dimension under the condition of the matrix being small sample size (SSS). Such information loss is called SSS problem. However, the covariance matrix in 2DPCA is full rank for a matrix of sparse data. Therefore the curse of dimensionality and the SSS problem (sparse data in a matrix) can be avoided (Sanguansat, 2012).

TEC Data Processing

The global TEC data prior to the explosion occurred at 15:55 (UT) on July 31, 2014, were examined to detect explosion-related TEC anomaly and GIMs are only used to observe TEC situation in this study. However the TEC anomaly is detectable in the time interval 16:00 to 16:10 (UTC) by 2DPCA and therefore the procedure of TEC data processing in the time interval is shown. Figure 1(a) shows the GIMs during the time from 16:00 to 16:10 on July 31, 2014. For GIMs in Figure 1(a), each GIM includes global coverage completely, which is divided into 600 small grids with respective size of 12° in longitude and 9° in latitude, respectively. The global TEC data are divided into 600 grids with respective size of 12° in longitude and 9° in latitude, respectively. The spatial resolution of the global TEC data for the GDGPS system is 5 and 2.5 degrees in longitude and latitude, respectively (Hernández-Pajares *et al*., 2009). Therefore 4 TEC data, which belong to two-dimensional data, are enough to take into a grid. The 4 TEC data in each grid are formed as a matrix *A* of Eq.1 with 2x2 dimensions, which is a small sample signal size

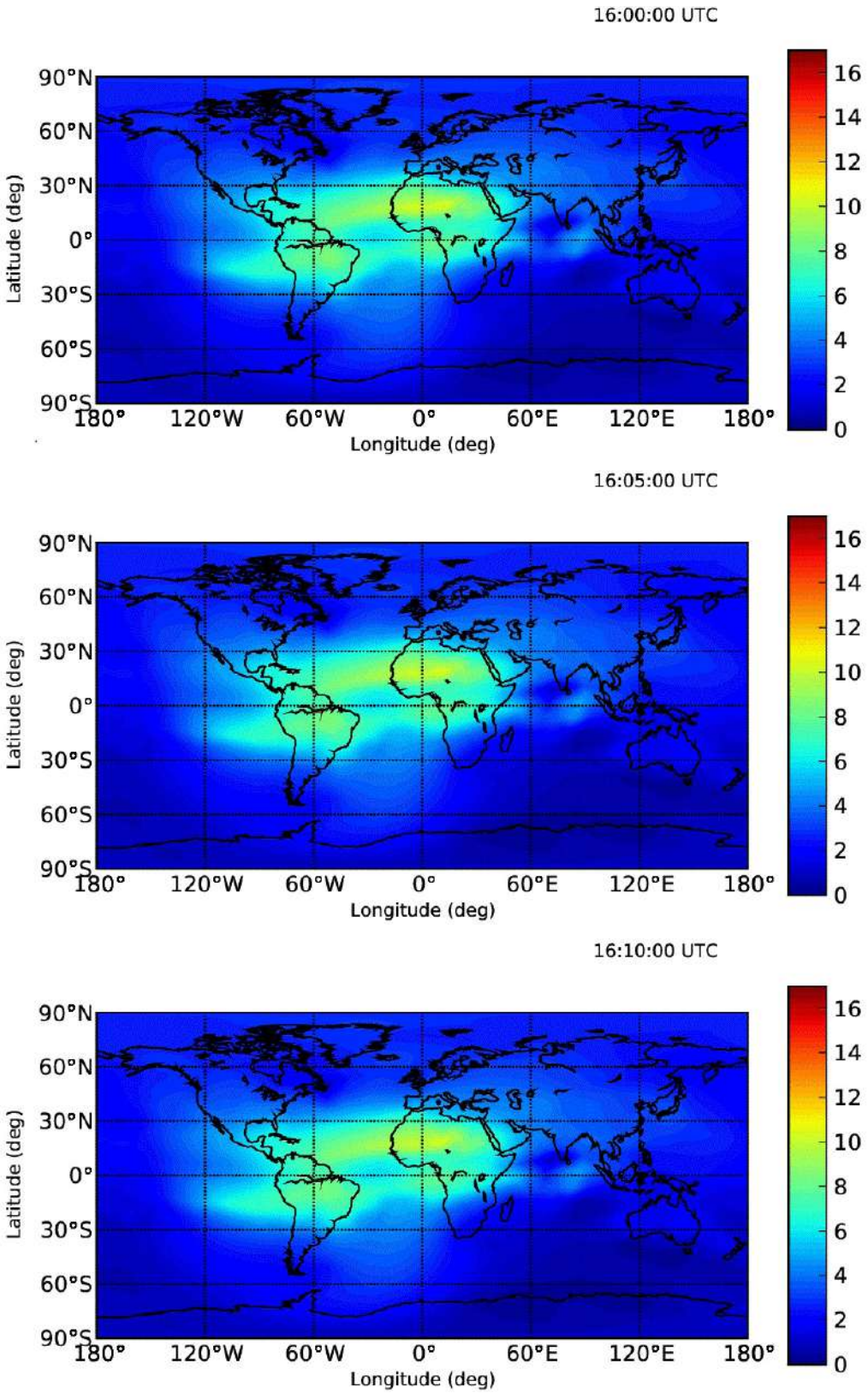

Figure 1a. These figures show GIMs during the time from 16:00 to 16:10 (UT) on July 31, 2014. The geographic coordinates of Kaohsiung are (22°36'39"N 120°19'8"E) (TEC data Source: NASA Global Differential GPS system). They are different from the TEC data source of Lin (2011). They were extracted from FORMOSAT-3 satellite system (Belongs to Taiwan) with low spatial and time resolutions at that time.

(SSS) in each grid. This allows for 600 principal eigenvalues to be computed for each of the 600 smaller grids.

Results

The large principal eigenvalues were shown to have relations to the earthquakes (Lin 2010; 2011). The explosions cause ground vibrations that are similar to the effects of the earthquakes and the volcanic explosions (Lin, 2013), causing acoustic shock waves and the large principal eigenvalues were found to represent volcanic explosions. Results have shown the explosion generated TEC anomaly that was represented by large principal eigenvalues. The large principal eigenvalue can indicate a TEC anomaly. However large principal eigenvalue could not show the actual time variations of TEC and their anomalies from clear reference time variations because a principal eigenvalue donates a mathematical indicator for the principal characteristics of the data. Therefore the large principal eigenvalues in Figs 1(b) show the existence of explosion-related TEC anomaly represented by a large principal eigenvalue from 16:00 to 16:05 on July 31, 2014, with a duration time of about 5 minutes. The possibility of other factors such as solar flare and geomagnetic effects affecting the results are considered by examining Kp and Dst indices (Fares Saba *et al*., 1997) and shown in Figure 2(a) (b) that reveals that July 31, was a geomagnetic quiet day. The region of TEC anomaly may be due to ionospheric disturbances with very quick horizontal spreading.

Discussion

2DPCA was able to detect TEC anomaly detectable by 2DPCA from 16:00 to 16:05 UT on July 31, 2014, over Kaohsiung City and Taiwan. The most evident physical mechanism was acoustic shockwave waves (Blanc and Jacobson, 1989) creating large scale ionospheric density irregularities and traveling up into the ionosphere. The duration time of TEC anomaly was estimated at least 5 minutes. The speed of acoustic shock waves was difficult to estimate since only the large principal eigenvalue was shown as TEC anomaly. However the 2DPCA could not estimate the time from the beginning of the explosion to the beginning of TEC disturbance. Moreover the behavior of plasma in the ionosphere is very complicated from seismotraveling ionospheric distrubances (STIDS) after or during an earthquake and the distrubances are amplified in a large area of the ionosphere (Liu, 2011). Therefore the ionospheric distrubances was over Taiwan. For comparison, some studies are stated. Drobzheva and Krasnov (2003) have used a terrestrial atmospheric model due to a chemical explosion on the ground to describe the propagation of acoustic pulses and the effects of these pulses on the ionosphere above the explosion. The results agreed well with acoustic and radio sounding data measured for the 1981 Mill Race explosion at seven different altitudes approximately from 10 to 260 km. In their work, a terrestrial atmospheric model was given but a principal eigenvalue as a mathematical indicator was not necessary to give a model to detect sensitively a weak TEC anomaly without a realistic propagation model. Jones and Spracklen (1974) and Krasnov *et al*. (2003) described and re-analyzed an explosion of unprecedented magnitude occurred at the Nypro plant at Flixborough, Lincolnshire. The information regarding the time sequence of the explosion and the amplitude of the blast wave was considered to the Mill Race experiment. However, 2DPCA was used for TEC data to detect the anomaly related to the explosion without considering the atmosphere environment and traveling of acoustic shock waves. Moreover the research topics of studies of Drobzheva and Krasnov (2003) and Jones and Spracklen (1974) are different from the topic of this study. 2DPCA is shown to be more sensitive to detect weak TEC anomaly from TEC data. Therefore 2DPCA is a careful data handling description for the topic in this study. Afraimovich *et al*. (2001) researched the acoustic shock wave due to the occurrence of earthquakes to affect ionosphere. They studied the earthquake effects in Turkey on August 17, and November 12, 1999, and in Southern Sumatra on June 4, 2000, and found that the ionospheric response related to the earthquakes due to acoustic shock waves is 180-390 s. Compared with the result of this study, 2DPCA has shown its advantage and credibility to estimate the duration time of explosion-related TEC anomaly. It is worth noting that this explosion is very huge and then it is possible to predict explosion time due to high gas release a short time before the explosion to reduce the number of dead people when the time resolution of TEC is more high.

Conclusion

2DPCA had the advantage to detect an explosion-TEC anomaly due to acoustic shock waves. Results have shown that a local ranging TEC anomaly was detectable at 16:00 to 16:05 UT on July 31, 2014, over Taiwan. The TEC anomaly could be caused by acoustic shock waves with a duration of at least 5 minutes.

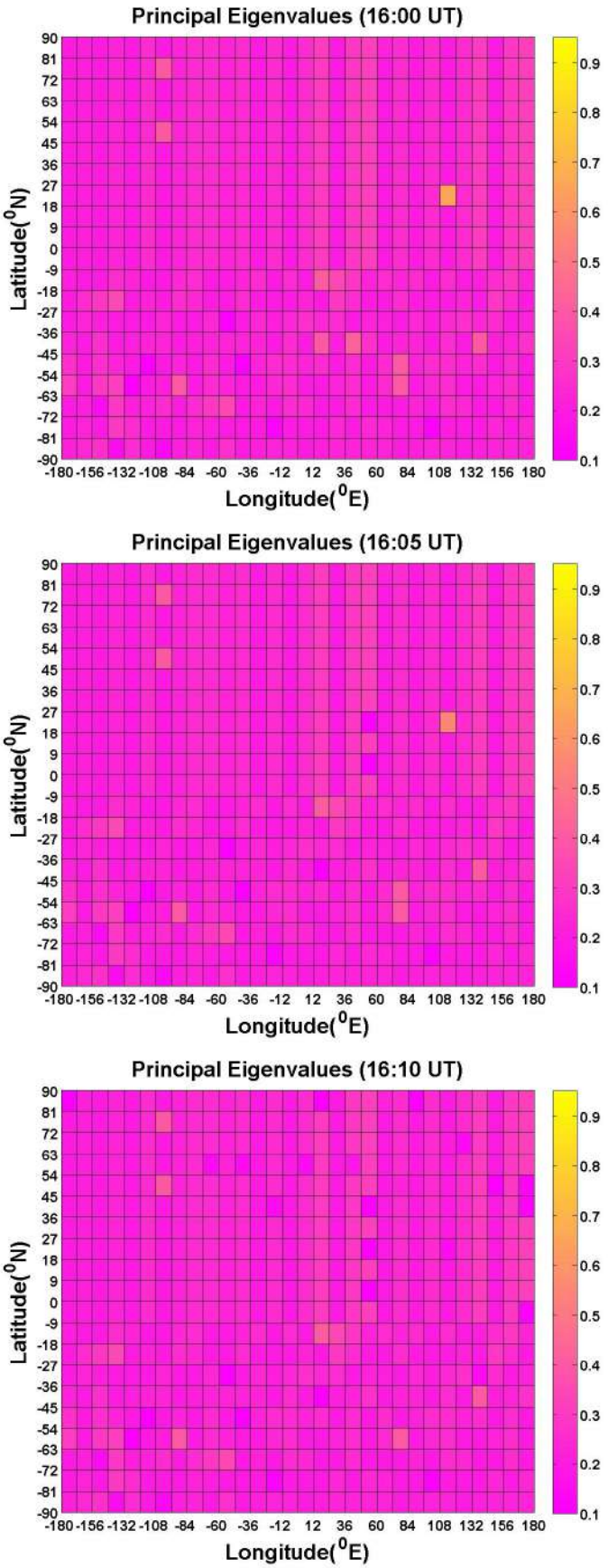

Figure 1b. The figures give a color-coded scale of the magnitudes of principal eigenvalues corresponding to Figure 1a. The color within a grid denotes the magnitude of a principal eigenvalue corresponding to Figure 1a, so that there are 600 principal eigenvalues assigned, respectively. The geographic coordinates of Kaohsiung city are (22°36′39″N 120°19′8″E). In these three figures, the values of the principal eigenvalues are between 0.11 and 0.93, therefore the colour bar is scaled between 0.1 and 0.95 instead of 0 and 1 in order to compare the strength of TEC anomalies with the three principal eigenvalues over Kaohsiung city. The TEC source from FORMOSAT-3 satellite system had low spatial and time resolutions, therefore the global TEC data are divided into 100 grids of 36° in longitude and 18° in latitude, respectively (Lin, 2011).

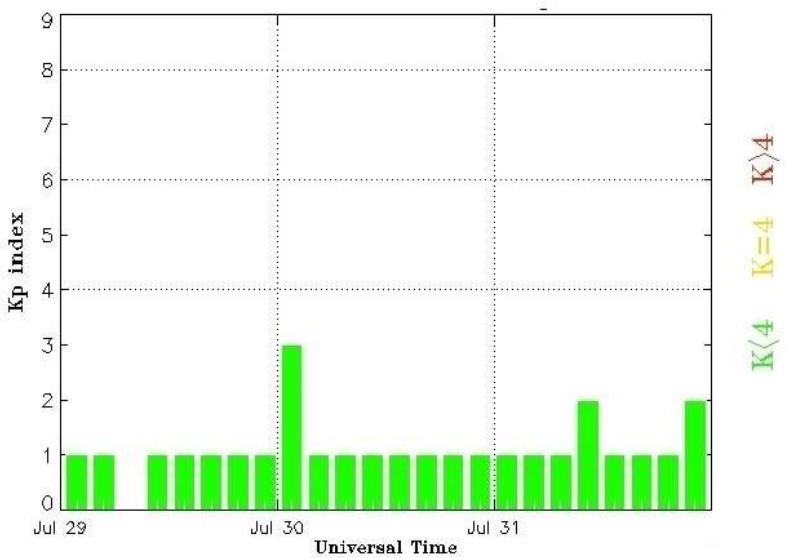

Figure 2a. Shows the Kp index from July 29 to 31, 2014 (Space Weather Prediction Center). The Kp index was derived by calculating a weighted average of K-index from a network of geomagnetic observatories. Kp smaller than 4 represents geomagnetic quiet time (Bartels et al, 1939). In this figure, Kp index have no better time resolution to show geomagnetic effects, and therefore the Dst index will be shown for geomagnetic effects due to better time resolution in Figure 2b.

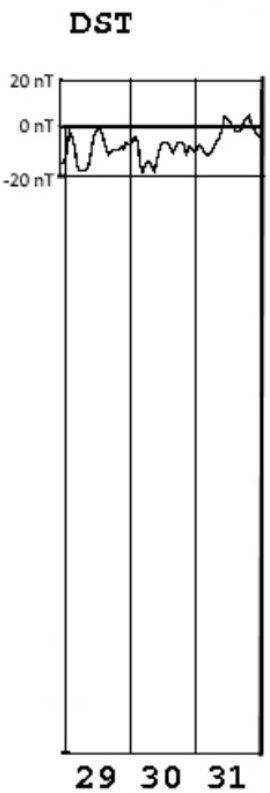

Figure 2b. Shows the Dst index from July 29 to 31 (World Data Center for Geomagnetism, Kyoto). The Dst index is a measure of geomagnetic activity due to solar activity and the unit is nT (Hamilton, 1988).

Acknowledgements

The author is grateful to NASA Global Differential GPS system (GDGPS) for the useful references data; In Memory of deaths due to this huge explosion in Kaohsiung city, Taiwan. Especially, also to my mother, " Lo, Yu-Mei" (8 Nov 1943--9 Oct 2016).

References

Andreeva E.S., Gokhberg M.B., Kunitsyn V.E., Tereshchenko E.D., Khudukon B.Z., Shalimov S.L., 2001, Radiotomographical Detection of Ionosphere Disturbances Caused by Ground Explosions. *Cosmic Res.*, January 2001, 39, Issue 1, pp 10-14. Doi: 10.1023/A:1002827609677.

Afraimovich, E. L., N. P. Perevalova, A. V. Plotnikov, and A. M. Uralov, 2001, The shock-acoustic waves generated by earthquakes. Annales Geophysicae, 19, 395-409.

Bartels, J., N. H. Heck and H. F. Johnston, 1939, The three-hour-range index measuring geomagnetic activity, Journal of Geophysical Research, Vol. 44 (4), 411-454, Doi: 10.1029/TE044i004p00411.

Blanc, E and A. R. Jacobson, 1989, Observation of ionospheric disturbances following a 5-kt chemical explosion 2. Prolonged anomalies and stratifications in the lower thermosphere

after shock passage, Radio Sci., 24(6), 739–746, doi:10.1029/RS024i006p00739.

Calais, E., J. B. Minster, M. Hofton and M. Hedlin, 1998, Ionospheric signature of surface mine blasts from Global Positioning System measurements, Geophysical Journal International. Vol. 132, No.1, 191-202, Doi:10.1046/j.1365-246x.1998.00438.x

Drobzheva, Ya. V and V.M. Krasnov, 2003, The acoustic field in the atmosphere and ionosphere caused by a point explosion on the ground, Journal of Atmospheric and Solar-Terrestrial Physics, 65, 369-377, Doi:10.1016/S1364-6826(02)00141-4.

Fares Saba, M. M., W. D. Gonzalez, A. L. clua de Gonzalez, 1997, Relationships between the AE, ap and Dst indices near solar minimum (1974) and at solar maximum (1979), Annales Geophysicae, Vol. 15 (10), 1265–1270, Doi: 10.1007/s00585-997-1265-x

Hamilton, D. C., G. Gloeckler, F. M. Ipavich, W. Stüdemann, B. Wilken, and G. Kremser 1988, Ring current development during the great geomagnetic storm of February 1986, J. Geophys. Res., 93 (A12), 14343–14355, doi:10.1029/JA093iA12p14343.

Hernández-Pajares, M., J. M. Juan, J. Sanz, R. Orus, A. Garcia-Rigo · J. Feltens, A. Komjathy, S. C. Schaer and A. Krankowski, 2009, The IGS VTEC maps: a reliable source of ionospheric information since 1998. J Geod, 83:263–275. DOI 10.1007/s00190-008-0266-1.

Jones, T. B. and C. T. Spracklen, 1974, Ionospheric effects of the Flixborough explosion, Letter to Nature, Nature 250, 719 - 720 (30 August 1974); Doi: 10.1038/250719a0.

Kechine, M. O., C.C.J.M. Tiberius, H. van der Marel, 2004,Real-time kinematic positioning with NASA's Internet-based Global. Differential GPS (IGDG). Independent performance assessment of the GDGPS system for real-time kinematic positioning performed at University of Delft, The Netherlands. GNSS Conference, St. Petersburg, Russia.

Krasnov, V. M., Ya. V. Drobzheva, J. E. S. Venart and J. Lastovicka, 2003, A re-analysis of the atmospheric and ionospheric effects of the Flixborough explosion, Journal of Atmospheric and Solar-Terrestrial Physics, Vol. 65, No 11–13, 1205–1212, Doi: 10.1016/j.jastp.2003.07.010.

Lin, J. W., 2010, Ionospheric total electron content (TEC) anomalies as associated with earth quakes through Karhunen-Loéve Trans form (KLT). Terr. Atmos. Ocean. Sci., 21, 253-265, doi: 10.3319/TAO.2009.06.11.01 (T).

Lin, J. W., 2011, Use of principal component analysis in the identification of the spatial pattern of an ionospheric total electron content anomalies after China's May 12, 2008, M = 7.9 Wenchuan earthquake, Advances in Space Research 47, 1983–1989, Doi:10.1016/j.asr.2011.01.013.

Lin, J. W., 2013, Ionospheric Anomaly due to the volcanic eruption in Colima, Mexico, 06 January 2013: Two-Dimensional Principal Component Analysis, European Journal of Remote Sensing, 46: 689-698, Doi: 10.5721/EuJRS20134640..

Liu, J. Y., C. H. Chen, C. H. Lin, H. F. Tsai, C. H. Chen, and M. Kamogawa, 2011, Ionospheric disturbances triggered by the 11 March 2011 M9.0 Tohoku earthquake, J. Geophys. Res., 116, A06319, doi: 10.1029/2011JA016761.

Ouyang, G., J. Wang, J. Wang and D. Cole, 2008, Analysis on Temporal-Spatial Variations of Australian TEC. International Association of Geodesy Symposia, 2008, Volume 133, Part 4, 751-758, DOI: 10.1007/978-3-540-85426-5_86.

Sanguansat, P, 2012, Principal Component Analysis– Engineering Applications, Published by InTech, Janeza Trdine 9, 51000 Rijeka, Croatia. 300pp. ISBN 978-953-51-0182-6.

Geofísica Internacional (2018) 57-1: 67-77

Original paper

Impact of powerful volcanic eruptions and solar activity on the climate above the Arctic Circle

Elena A. Kasatkina*, Oleg I. Shumilov, Mauri Timonen and Alexander G. Kanatjev

Received: April 26, 2017; accepted: October 09, 2017; published on line: January 01, 2018

Resumen

En este trabajo, se evalúa la respuesta del crecimiento de los árboles en la región polar (Península de Kola y la Laponia de Finlandia) a las erupciones volcánicas más potentes (VEI > 4) durante un periodo de 1445-2005. El análisis se basó en dos cronologías de anillos de árboles de elevada resolución: Loparskaya (1445-2005) y Finnish (~ 7500 años). Estas cronologías se desarrollaron a partir de muestras de Pinus sylvestris L. recogidas cerca de la línea de árboles del norte en la estación de Loparskaya (68.63º N, 33.25º E) y la Laponia finlandesa (68-70º N; 20-30º E), respectivamente. El análisis de sobreposición de época indicó una disminución significativa en el crecimiento de los anillos de los árboles polares durante 7 años después de las erupciones. Asimismo, el estudio de los anillos muestra que el nivel de crecimiento de los árboles en la región polar se ve afectado por las más poderosas erupciones volcánicas producidas en latitudes bajas. En cambio, los volcanes islandeses no tienen un impacto significativo en el clima de la Península de Kola y la Laponia finlandesa. La aplicación del análisis wavelet para la cronología del anillo de árboles de Loparskaya permitió identificar la existencia de los ciclos principales de actividad solar (11, 20-25 y ~ 100 años). Además el análisis wavelet reveló una fuerte coherencia en las bandas 8-13 y 20-30 años indicando un posible vínculo entre la actividad solar y el cambio climático a escala regional.

Palabras clave: erupciones volcánicas, datos de los anillos de los árboles, cambio climático, actividad solar.

Abstract

The tree growth response in polar region (Kola Peninsula and Finnish Lapland) to the most powerful (VEI>4) volcanic eruptions is assessed over a period of 1445-2005. The analysis was based on the Loparskaya (1445-2005) and Finnish supra-long (~ 7500 years) tree-ring chronologies. These chronologies were developed from *Pinus sylvestris* L. samples collected near the northern tree line at Loparskaya station (68.63º N, 33.25º E) and Finnish Lapland (68-70º N; 20-30º E), respectively. A superposed epoch analysis indicated a significant decrease in polar tree-ring growth over 7 years after the eruptions with subsequent recovery to its normal level. The level of tree growth in polar region is affected by most powerful low-latitude volcanic eruptions. By contrast, high-latitude Icelandic volcanoes have no significant impact on the climate of Kola Peninsula and Finnish Lapland. The application of wavelet analysis for the Loparskaya tree ring chronology allowed to identify the existence of the main cycles of solar activity (11, 20-25, and ~ 100 years). Moreover, the wavelet analysis revealed a strong coherence in the 8-13 and 20-30 year bands, indicating a possible link between solar activity and climate change on a regional scale.

Key words: volcanic eruptions, tree-ring data, climate change, solar activity.

E.A. Kasatkina*
O.I. Shumilov
A.G. Kanatjev
Polar Geophysical Institute
Fersmana str. 14, 184209 Apatity
Murmansk Oblast, Russia
*Corresponding author: oleg@aprec.ru

M. Timonen
Natural resources Institute Finland (LUKE)
Rovaniemi, Finland

Introduction

It is well known that, throughout the Holocene prior the industrial period, global climate changes took place under the influence of only natural factors including solar activity and powerful volcanic eruptions (Shumilov *et al*., 2000; Shindell *et al*., 2003; Soon and Baliunas, 2003). These factors strongly affect climate and atmosphere of the Earth (Crowley, 2000; Shumilov *et al*., 2000; Shindell *et al*., 2003; Soon and Baliunas, 2003; Velasco and Mendoza, 2008), but which of them (and some others as well) plays a dominant role is currently under discussion. However, it should be noted that considerable contribution to climatic change in recent decades is due to man-made factors (Vecchi and Soden, 2007). Volcanic eruptions emit huge amounts of volcanic dust, sulfur dioxide and water vapor into the atmosphere reducing the atmospheric transparency and preventing the penetration of solar radiation to the earth's surface. All these processes result in breaking the radiation balance of the atmosphere and lead to reduction of the surface temperature in most cases. Sulfate aerosols that enter the stratosphere after powerful volcanic eruptions may exist there for several years (Robock, 2000). Recent powerful volcanic eruptions such as Tambora (1815), Krakatau (1883), Santa Maria (1902), Katmai (1912), Agung (1963), El Chichon (1982), and Pinatubo (1991), caused a cooling in the Northern Hemisphere by 0.2 – 0.8º C for several years (Rampino and Self, 1982; Robock, 2000; Wigley, 2000; Zanchettin *et al*., 2013). For example, the 1815 Tambora eruption produced the "year without a summer" in 1815 (Rampino and Self, 1982; Robock, 2000). However, volcanic eruptions cause not always and not everywhere cooling events. The climatic response to volcanic eruptions varies regionally and depends on the amount, chemical composition and height of volcanic emissions. Some studies documented that volcanic activity can lead to regional warming and even droughts, as happened, for example, after the 1783 Laki eruption in Iceland, when most of the European territory was covered by an unusually dry fog (Thordarson and Self, 2003; Ogle *et al*., 2005), and after the 1991 Pinatubo eruption in Indonesia (McCormick *et al*., 1995; Robock, 2000).

The period of instrumental meteorological observations does not exceed 100 – 120 years and covers only a small number of powerful volcanic eruptions. Therefore, the climatic effects of volcanic activity were studied using several proxy records (the content of sulfuric acidity in ice cores and tree-ring data) (Hammer *et al*., 1980; Scuderi, 1990; Briffa *et al*., 1998; Gervais and MacDonald, 2001; Vaganov and Shiyatov, 2005; Shumilov *et al*., 2000; 2011; Kasatkina *et al*., 2013). The possible response of tree-ring growth and even the formation of so-called "frost rings" (Vaganov and Shiyatov, 2005) are associated with a decrease of temperature after major volcanic eruptions. The emission of a large amount of volcanic gases into the atmosphere leads to acid precipitation, which can as well cause deep depression in tree growth (Thordarson and Self, 2003; Ogle *et al*., 2005). Moreover, the reduction of atmospheric transparency can affect the process of photosynthesis (Scuderi, 1990; Ogle *et al*., 2005).

It should be noted that the temperature decreases are more considerable when the volcanic eruptions occur during the minima of solar activity. Widely known is the period of global cooling during the Maunder minimum of solar activity (1645 – 1715 AD) which occurred in the Little Ice Age. The main solar factors influencing climate and atmosphere are solar radiation (Lean *et al*., 1995; Haigh, 1996), cosmic rays and, possibly, cosmic dust influencing the cloud cover of the atmosphere (Shumilov *et al*., 1996; Svensmark and Friis-Christensen, 1997; Kasatkina and Shumilov, 2005; Kasatkina *et al*., 2007). Climatic impacts are most clearly expressed in ring width of trees growing in extreme conditions close to the tree line at sites of their biological surviving (Fritts, 1976; Grace *et al*., 2002). The northern (or Arctic) tree line is the northernmost latitude where trees can grow. The Arctic tree-ring chronologies are of most interest for paleoclimatic studies because the trees growing near the northern tree-line seem to be highly sensitive to the influence of such external factors as temperature and solar radiation.

The aim of this study is to verify a hypothesis concerning the possible regional climatic response to volcanic and solar activity impacts during the last millennium by analyzing polar tree-ring chronologies from Kola Peninsula and Finnish Lapland.

Geographic setting

The tree-ring data used in this study were collected near the northern tree-line at Loparskaya station, Kola Peninsula (68.63 N, 33.25 E) (Figure 1). The climate of the Kola Peninsula unlike the other polar regions of Russia is influenced by warm air masses of the North Atlantic and cold air of Arctic regions (the Barents Sea, the Kara Sea, and the Taymir Peninsula). The Kola Peninsula involves

three climatic zones: sea coast, central area, and mountain section. The climate of the northern sea coast including the sampling site is influenced by the Barents Sea. The mean temperature is in the range from -6 to -12º C in the coldest month (February) and from 12 to 13º C in the warmest month (July). The annual mean temperature (precipitation) in the region ranges from 0º C (600-700 mm) on the coasts of the Barents and White Seas to -2º C (500-600 mm) in the central part of the Kola Peninsula. The mountain area is characterized by a cooler summer, a relatively mild winter, and a lot of precipitation with an average value of 1000 mm.

The Kola Peninsula is covered by taiga in the south and tundra in the north. The dominant tree species at or near the tree-line include pine (*Pinus sylvestris* L.), spruce (*Picea obovata* Ledeb.), and birch (*Betula pubescens* ssp. *szerepanovii*).

Methods

A total of 36 timber cores of *Pinus sylvestris* L. were sampled at the northern tree-line, including the oldest living pine with more than 560 years of age. Ring widths were measured with a precision of 0.01 mm by using an image analysis system (scanner and relevant software) (Kanatjev *et al*., 2014). Using these samples, the Loparskaya tree-ring chronology from living trees covering the period from 1445 to 2005 was developed. The data were processed using modern methods adopted in dendrochronology (cross-dating and standardization) with the help of COFECHA and ARSTAN programs (Holmes, 1983; Cook and Kairiukstis, 1990). In this study we also used the Finnish supra-long (~ 7500 years) tree-ring chronology collected at Northern Lapland (68-70º N; 20-30º E) (Helama *et al*., 2008).

Superposed epoch analysis of both chronologies was performed to asses the tree growth response on the most powerful (VEI>4, Volcanic Explosivity Index) volcanic eruptions (http://www.volcano.si.edu/world/largeeruptions.cfm). The VEI evaluates volcanic eruptions based on the height of the eruption column and solid material ejected (Newhall and Self, 1982). The most powerful volcanic eruptions can cause lowering of temperature and tree growth for five years and more (Rampino and Self, 1982; Scuderi, 1990; Robock, 2000; Wigley, 2000; Gervais and MacDonald, 2001; D'Arrigo *et al*., 2013; Zanchettin *et al*., 2013). In the present study, the analysis was based only on those events that are at least 7 years apart. As a result, a total of 19 events are considered covering the period from 1445 to 2005 (see the Table 1). Analysis of individual events (Huaynaputina in 1600, Laki in 1783 and Tambora in 1815) was also performed. Yearly averages of sunspot numbers were obtained from the National Geophysical Data Center (ftp://ftp.ngdc.noaa.gov) for the period of 1700 – 2005.

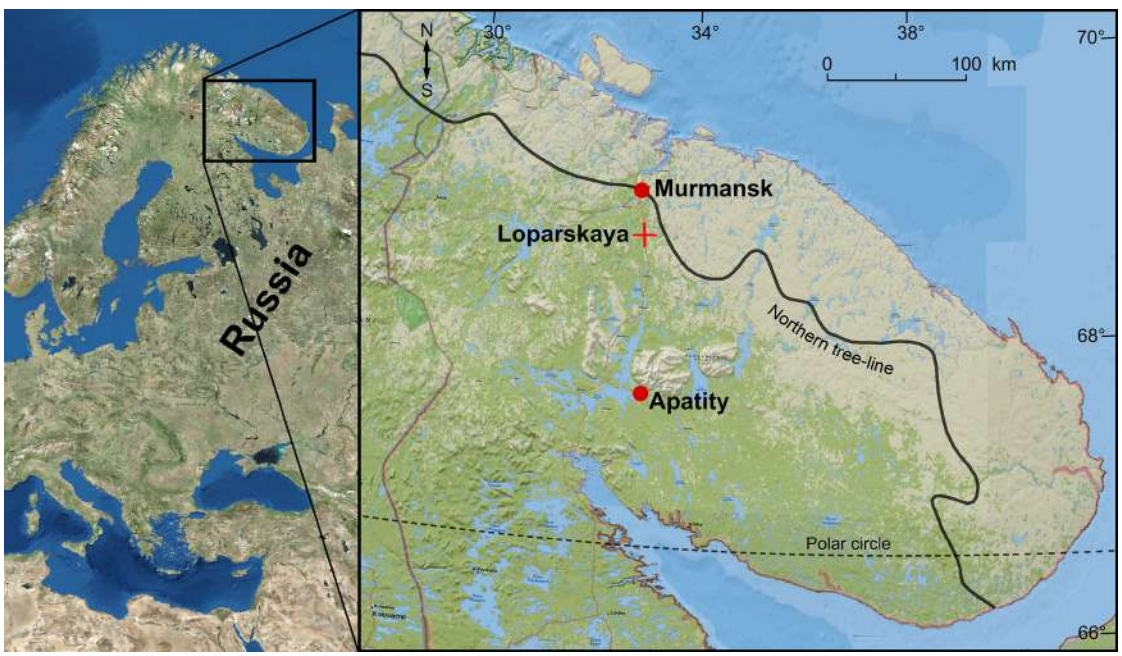

Figure 1. Location of the sampled site (cross) in relation to the northern pine tree line.

To identify the main periodicities and their evolution in time-frequency mode, we applied the continuous wavelet transform (CWT) of a time series *X* (Torrence and Compo, 1998):

$$Wx = \frac{1}{\sqrt{s}} \int_{-\infty}^{\infty} X(t)\psi\left(\frac{t-b}{s}\right) dt \quad (1),$$

where *t* is the time, *s* is the wavelet scale, *b* is the shift of the analysis window, ψ is the base wavelet function. We used here the Morlet function that may be defined as a plane wave modulated by a Gaussian function (Torrence and Compo, 1998):

$$\psi(t) = \pi^{-1/4} e^{iw0t/s} e^{-t^2/(2s)^2} \quad (2),$$

where ω_0 is the dimensionless frequency (we use here ω_0=6, since it provides a good balance between time and frequency localization). In order to avoid the edge effects, Torrence and Compo (1998) introduced the cone of influence (COI) in which the wavelet power caused by a discontinuity at the edge has dropped by a factor e^{-2}.

To examine the relationship in time-frequency scale between tree-ring growth and solar activity, the cross-wavelet transform was applied to two time series (Grinsted *et al*., 2004):

$$W_{LN}(s) = W_L(s) W_N{}^*(s) \quad (3),$$

where (*) denotes the complex conjugate, *L* and *N* indexes denote tree-ring and sunspot number time series respectively. The phase angle of W_{LN} describes the phase relationship between *L* and *N* in time frequency space. We standardized (zero mean, unit standard deviation) both time series before analysis. The wavelet coherence (WTC) was used to assess a localized correlation coefficient in time frequency space between tree ring data and sunspot numbers (Grinsted *et al*., 2004):

$$R^2(s) = \frac{\left|S\left(s^{-1} W_{LN}(s)\right)\right|^2}{S\left(s^{-1}\left|W_L(s)\right|^2\right) \cdot S\left(s^{-1}\left|W_N(s)\right|^2\right)} \quad (4),$$

where *S* denotes smoothing in both time and scale. The statistical significance levels of CWTs and WTC were estimated using Monte Carlo method against a red noise model (Torrence and Compo, 1998; Grinsted *et al*., 2004).

Results and Discussion

In this study, we analyzed climatic impacts of solar and volcanic activity with help of both (Loparskaya and Finnish supra-long) tree-ring chronologies developed on the basis of samples taken near the northern tree line (Figure 1).

Figure 2 shows tree-ring growth responses on the most powerful volcanic eruption of Huaynaputina (VEI=6) in February 1600 (see the Table). For comparison, the upper timberline Cirque Peak (California; 36.5º N, 118.2º E) foxtail pine tree-ring record (Scuderi, 1990) is also presented (see Figure 2c). The 1600 eruption of Huaynaputina in Peru was the largest volcanic eruption in South America spanning the past 2000 years (de Silva and Zielinski, 1998; Fei *et al*., 2015; Stoffel *et al*., 2015). Based on ice core and tree-ring records, this eruption injected a large amount of sulfur (up to 32 Mt) into the atmosphere, reducing solar

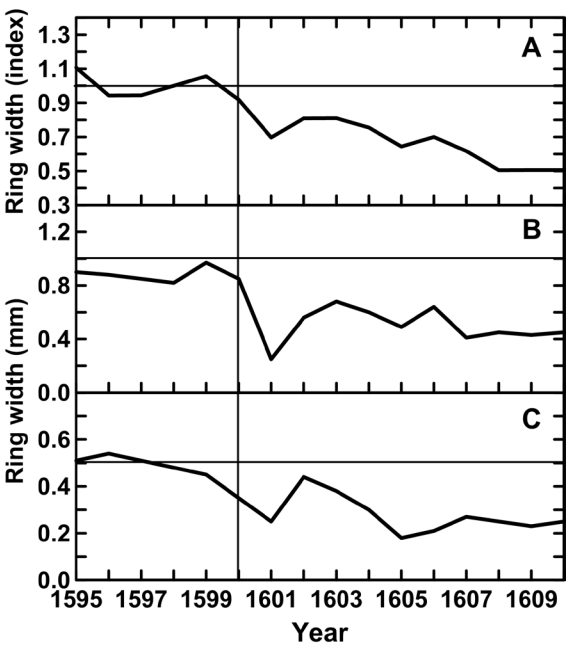

Figure 2. Tree-ring growth response to the volcanic eruption of Huaynaputina (VEI=6) in Peru (1600 AD): **(A)** the Loparskaya (68.63 N, 33.25 E) pine tree-ring chronology, **(B)** the Finnish supra-long (~ 7500 years) pine tree-ring chronology (68-70º N; 20-30º E), **(C)** the Circue Peak (California; 36.5º N, 118.2º E) foxtail pine tree-ring chronology (Scuderi, 1990).

Table 1. Most powerful volcanic eruptions (VEI>4) since AD 1470.

Volcanoes		Eruption dates	Coordinates	VEI
Sakura-Jima, Japan		November 3, 1471	31.6 N, 130.7 E	5
Agua de Pau, Azores		June 28, 1563	37.8 N, 25.5 W	5
Huaynaputina, Peru	+	February 19, 1600	16.6 S, 70.9 W	6
Parker, Philippines	+	January 4, 1641	6.1 N, 124.9 E	5
Gamkonora, Indonesia		May 20, 1673	1.4 N, 127.5 E	5
Tongkoko, Indonesia	+	1680	1.5 N, 125.2 E	5
Fuji, Japan		December 16, 1707	35.4 N, 138.7 E	5
Katla, Iceland	+	May 11, 1721	63.5 N, 19 W	5
Shikotsu, Japan	+	August 19, 1739	42.7 N, 141.3 E	5
Katla, Iceland		October 17, 1755	63.5 N, 19 W	5
Laki, Iceland		June 8, 1783	64.4 N, 17.3 W	4+
St Helens, USA	+	January 15, 1800	46.2 N, 122.2 W	5
Tambora, Indonesia		April 10, 1815	8.3 S, 118.0 E	7
Galunggung, Indonesia		October 8, 1822	7.3 S, 108.1 E	5
Cosiguina, Nicaragua	+	January 20, 1835	13 N, 87.6 W	5
Askja, Iceland		March 29, 1875	65 N, 17 W	5
Azul, Chile	+	April 10, 1932	35.7 S, 70.8 W	5
Agung, Indonesia		March 17, 1963	8.3 S, 115.5 E	5
Pinatubo, Philippines	+	June 15, 1991	15.1 N, 120.4 E	6

By crosses indicated the major volcanic eruptions that affect the tree growth at the study area.

insolation and resulting in global temperature drop (Hammer *et al*., 1980; Scuderi, 1990; de Silva and Zielinski, 1998). The eruption of Huaynaputina in 1600 AD had a global impact on human society and dramatically affected the weather and environment in Central Europe, southern Scandinavia, China and the North America (Scuderi, 1990; de Silva and Zielinski, 1998; Verosub and Lippman, 2008; Fei *et al*., 2015; Stoffel *et al*., 2015). In Russia, this event caused strong frosts in the summer of 1601 and crop failure which led to severe famine and unprecedented mortality (more than 500,000 people) in 1601 – 1603, social disruption and political unrest called the Time of Troubles (Verosub and Lippman, 2008). Figure 2 shows a significant (more than 25%) reduction in tree growth, which is observed almost simultaneously in all three sites in the year following the eruption. All three curves behave identically and reveal a significant ring width decrease more than ten years (see Figure 2).

The 1815 eruption of Tambora in Indonesia (VEI>7), which was the most powerful over the study period, ejected 80 Mt of sulfuric dioxide into the atmosphere and led to the temperature decrease (~ 0.8º C) in the Northern Hemisphere (Sadler and Grattan., 1999; Ogle *et al*., 2005; Stoffel *et al*., 2015). In North America and Central Europe, 1816 was called the "year without a summer". However, the climate in Scandinavia in that year was mild, and no significant temperature drops were observed (Sadler and Grattan., 1999; D'Arrigo *et al*., 2013). From Figure 3, it is observed that the year 1816 shows no decrease in tree growth relative to the previous year. The decrease began much earlier (in 1808) and lasted until 1822, and again, all three curves are identical (see Figure 3). Some evidence (large acidity peak in ice core) indicate that a powerful climatically effective unknown volcanic eruption occurred in 1908/1909 (Scuderi, 1990; White *et al*., 1997; D'Arrigo *et al*., 2012; Guevara-Murua *et al*., 2014; Wahl *et al*., 2014). Two other powerful low-latitude volcanic eruptions in 1673 (Gamkonora) and in 1822 (Galunggung) also did not lead to the expected volcanic cooling (see Table 1). According to radiocarbon dating, a powerful volcanic eruption in 1660 (± 20 y) in New Guinea may have preceded the eruption of Gamkonora (White *et al*., 1997; Wahl *et al*., 2014). In this case, the expected volcanic cooling possibly resulted from increased atmospheric opacity from low-

latitude eruptions in 1673 (Gamkonora), 1815 (Tambora), and 1822 (Galunggung) could be masked on the already existing background provided by the previous eruptions.

It should be noted that all these eruptions occurred during the minimuma of solar activity, which possibly intensified the climatic response.

Icelandic volcanoes are most closely located to the Kola Peninsula and Finnish Lapland. Therefore, it is more interesting to study the environmental and climatic impacts of their most powerful eruptions on this region. Figure 4 shows tree growth response to the eruption of Laki (VEI= 4+), which began in June 1783. The 1783 eruption of Laki in Iceland continued eight months, ejecting around 122 Mt of sulfur dioxide into the atmosphere and causing an unusually dry fog and drought in most of Europe (Thordarson and Self, 2003; Ogle *et al*., 2005). According to our data, no deviation in the annual tree growth was observed in 1783 – 1785 (see Figure 4). From Figure 4b, it is seen that the Loparskaya tree-ring record reveals a significant drop (by 50% relative to the previous year) in 1786, three years after the eruption of Laki volcano, therefore it can

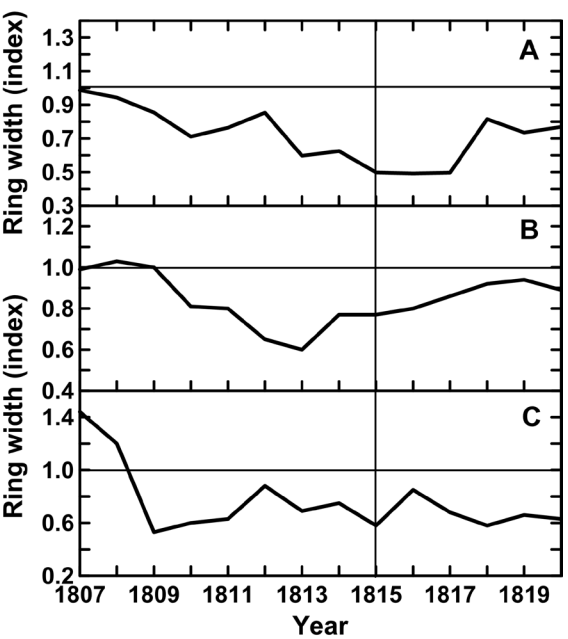

Figure 3. Tree-ring growth response to the volcanic eruption of Tambora (VEI=7) in Indonesia (1815): **(A)** the Loparskaya (68.63 N, 33.25 E) pine tree-ring chronology, **(B)** the Finnish supra-long (~ 7500 years) pine tree-ring chronology (68-70º N; 20-30º E), **(C)** the Circue Peak (California; 36.5º N, 118.2º E) foxtail pine tree-ring chronology (Scuderi, 1990).

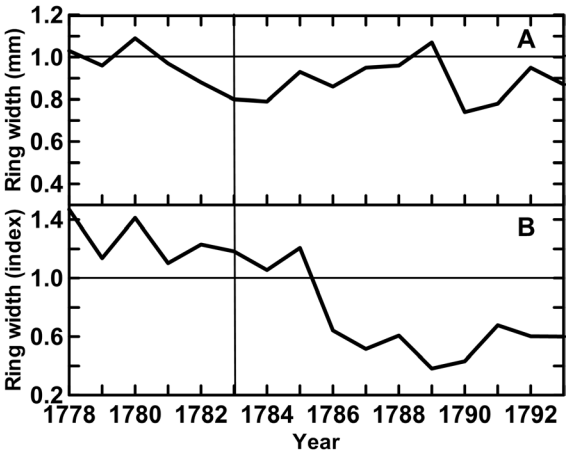

Figure 4. Tree-ring growth response to the volcanic eruption of Laki (VEI=4+) in Iceland (1783): **(A)** the Loparskaya (68.63 N, 33.25 E) pine tree-ring chronology, **(B)** the Finnish supra-long (~ 7500 years) pine tree-ring chronology (68-70º N; 20-30º E).

hardly be associated with this event. This conclusion is also confirmed by the absence of any depression after 1783 in the annual tree growth according to the Finnish data (Figure 4a). Similar results demonstrating the absence of a decrease in the annual growth immediately after the Laki eruption were obtained in other studies (Sadler and Grattan, 1999; Thordarson and Self, 2003; Ogle *et al*., 2005). The analysis of climatic response to other powerful eruptions of Icelandic volcanoes (see the Table 1) revealed no changes. As it concerned the Laki eruption, that question had been considered in details in connection with a meteorological situation during the event (Grattan and Pyatt, 1999; Thordarson and Self, 2003; Sonnek *et al*., 2016). In accordance with these results, one can assume that a stable blocked high-pressure air pattern over Europe concentrated volcanic gases near the Earth's surface and prevented them to spread into the Kola Peninsula.

Figure 5 presents the composite response of tree growth in polar region obtained by the superposed epoch method for 19 volcanic eruptions listed in the Table 1. A significant suppression in tree growth is observed at both polar sites for seven years after the eruption with the subsequent recovery (see Figure 5). This result is consistent, in general, with the findings obtained earlier from dendroclimatic reconstructions of northern Eurasia (Vaganov and Shiyatov, 2005) and North America (Scuderi, 1990). Our analysis showed that the main contribution to the observed decrease in tree growth at both polar sites was made by low-latitude volcanic eruptions (see the Table 1).

As was noted above, global climatic changes occurred under the composite influence of two main natural factors: powerful volcanic eruptions and solar activity. The main solar factors acting on climate and atmosphere are solar radiation (Lean *et al*., 1995; Haigh, 1996), cosmic rays and possibly, cosmic dust influencing the cloud cover of the atmosphere (Shumilov *et al*., 1996; Svensmark and Friis-Christensen, 1997; Kasatkina and Shumilov, 2005; Kasatkina *et al*., 2007). Volcanic factors act during powerful eruptions, while solar factors work continuously depending on cyclic intensity of solar activity. As can be seen from Fig. 6, the long variation in tree-ring indexes seems to demonstrate a certain similarity with the envelope of the 11-year maxima of sunspot numbers (r=0.31, p<0.05). The Sporer (1416 – 1534), Maunder (1645 – 1715), and Dalton (1801 – 1816) minima of solar activity are accompanied by cooling in the Kola Peninsula and tree growth depression. The significant tree growth depression and cooling from 1780 to 1830 coincide with the Dalton minimum of solar activity and most powerful volcanic eruption of Tambora in 1815 (see Figure 6).

For identification of solar cycles in tree-ring records and understanding their evolution in time frequency scale, we applied the Morlet-based continuous wavelet transform (CWT) and the wavelet coherence analysis (WTC). Figure 7 shows the wavelet power spectrum for the (a) Loparskaya tree-ring chronology, the (b) yearly sunspot number, and the (c) WTC between the tree rings and sunspot number. WTC is used as a localized correlation coefficient between two time series in time frequency space (Grinsted *et al*., 2004). Arrows indicate a phase relationship between the variables (see Figure 7c). The wavelet spectrum for the Loparskaya tree-ring chronology shows significant periodicity around 100 years (Gleissberg solar cycle), which is present all the time (see Figure 7a). The ~ 22 year solar cycle signal (Hale cycle) with less intensity intermittently appears between 1470-1620, 1680-1830, and 1920-1970 (see Figure 7a). The major ~ 11 year solar cycle signal (Schwabe cycle) is highly suppressed along the time interval, weakly appearing between 1500-1570, 1600-1750, and 1870-1900. The CWT for tree-ring data exhibits also a significant (or near the confidence level) power peak in the 2-7 year band, appearing intermittently along all the time interval. This periodicity corresponds to the second harmonic

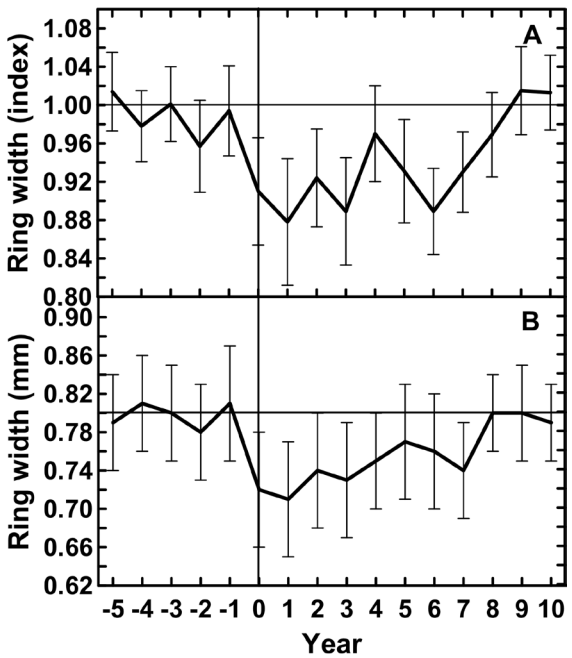

Figure 5. Response of polar tree-ring growth to the most powerful (VEI>4) volcanic eruptions since AD 1470 (see the Table) obtained by the superposed epoch method: **(A)** the Loparskaya (68.63 N, 33.25 E) pine tree-ring chronology, **(B)** the Finnish supra-long (~ 7500 years) pine tree-ring chronology (68-70º N; 20-30º E). Standard errors are shown by vertical lines.

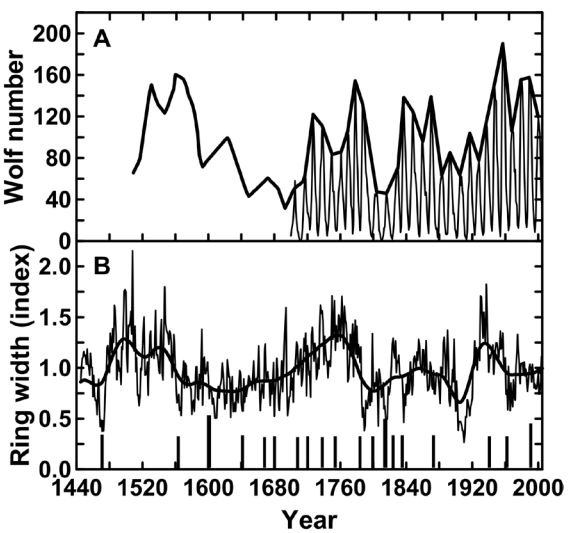

Figure 6. (A) Time series of sunspot number (1700-2005) (thin line) and their 11-year maximum envelope (1500-2005) (thick line). The sunspot numbers since the 1500 AD have been reconstructed on the polar aurora data (Shove, 1955). **(B)** The Loparskaya tree-ring width standard chronology of *Pinus sylvestris* L. (1445-2005) (thin line) and its smoothed 23-year moving average alpine. Most powerful volcanic eruptions (VEI>4) since AD 1470 are shown by vertical lines (see the Table).

(5.5 year) of the Schwabe cycle, and, possibly, is also related to the North Atlantic Oscillation impact (Velasco and Mendoza, 2008). Figure 7c shows strong coherences in the 8-13 year band in phase between 1715 and 1730, and in anti phase for the time intervals of 1770-1840 and 1880-1920 (see Fig. 7c). The wavelet coherence also shows a statistically significant high power in the 20-30 year band over a period of 1770-1850 and 1920-2005 with a non-stationary phase relationship, the ~ 100 year is practically outside of the COI (see Fig. 7c).

In general, the wavelet coherence analysis between tree-ring data and sunspot numbers demonstrated a strong coherence in the 8-13 and 20-30 year bands indicating a possible link between solar activity and climate change on a regional scale. Earlier evidences of solar cycle signals were found in a lot of paleoclimatic proxy records from different sites (Baliunas *et al*., 1997; Kasatkina *et al*., 2007; Shumilov *et al*., 2007; Rigozo *et al*., 2002; Velasco and Mendoza, 2008; Wang and Zhang, 2011; Edvardsson *et al*., 2016; Sunkara and Tivari, 2016).

Conclusions

1. Our analysis of tree ring chronologies obtained for the Kola Peninsula and Finnish Lapland revealed the most significant (by 25% relative to the previous year) depression in tree growth after the 1600 eruption of Huaynaputina in Peru (VEI=6),which was the largest volcanic eruption in South America over the past 2000 years.

2. A superposed epoch analysis revealed a significant reduction in polar tree growth, which was observed for seven years after volcanic eruption with a subsequent recovery to its normal level.

3. The level of tree growth in polar region is affected by most powerful low-latitude volcanic eruptions. High-latitude Icelandic volcanoes have no significant impact on the climate of Kola Peninsula and Finnish Lapland.

4. The application of wavelet analysis for the Loparskaya tree ring chronology identified

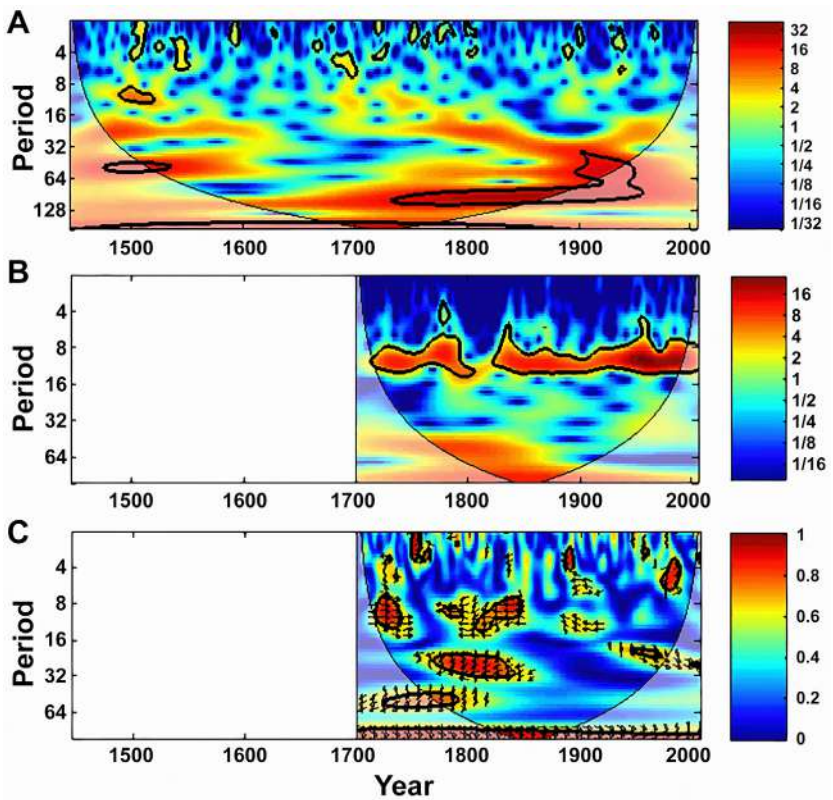

Figure 7. The continuous wavelet power spectrum of the standardized tree-ring index **(A)** and sunspot number **(B)** time series; **(C)** the wavelet coherency between tree-ring indices and sunspot numbers. The relative phase relationship is shown as arrows (with in-phase pointing right, anti-phase pointing left). The 5% significance level against red noise is shown as a thick contour.

the existence of the main cycles of solar activity (11, 20-25, and ~ 100 years). The wavelet coherence analysis revealed a strong coherence in the 8-13 and 20-30 year bands indicating a possible link between solar activity and climate change on a regional scale.

5. Our results demonstrate the possibility of using polar tree-ring widths as indicators of solar and volcanic activity above the Arctic Circle.

References

Baliunas S., Frick P., Sokoloff D., Soon W., 1997, Time scales and trends in the Central England temperature data (1659-1990): A wavelet analysis. *Geophys. Res. Lett., 24,* 1351-1354.

Briffa K.R., Jones P.D., Schweingruber F.H., Osborn T.J., 1998, Influence of volcanic eruptions on Northern Hemisphere summer temperature over the past 600 years. *Nature, 393,* 450-452.

Cook E.R., Kairiukstis L., 1990, Methods of Dendrochronology. Dordrecht: Kluwer Academic Publishing, 211 pp.

D'Arrigo R., Wilson R., Anchukaitis K.J., 2013, Volcanic cooling signal in tree ring temperature records for the past millennium. *J. Geophys. Res., 118,* 9000-9010.

Edvardsson J., Adolphi F., Lindrholm H.W., Corona C., Muscheler R., Stoffel M., 2016, Periodicities in mid- to late-Holocene peatland hydrology identified from Swedish and Lithuanian tree-ring data. *Quarter. Sci. Rev.,* 200-208.

Fei J., Zhang D.D., Lee H.F., 2015, 1600 AD Huaynaputina eruption (Peru), abrupt cooling, and epidemics in China and Korea. *Adv. Meteorol., 2016,* doi: 10.1155/2016/3217038.

Fritts H.C., 1976, Tree rings and climate. London: Academic Press, 567 pp.

Gervais B.R., MacDonald G.M., 2001, Tree-ring and summer temperature response to volcanic aerosol forcing at the northern tree-line, Kola Peninsula, Russia. *The Holocene, 11,* 499-505.

Grace J., Berninger F., Nagy L., 2002, Impacts of climate change on the tree line. *Annals of Botany, 90,* 537-544.

Grattan J.P., Pyatt F.B., 1999, Volcanic eruptions dry fogs and the European palaeoenvironmental record: localized phenomena or hemispheric impacts? *Global Planet. Change, 21,* 173-179.

Grinsted A., Moore J.C., Jevrejeva S., 2004, Application of the cross wavelet transform and wavelet coherence to geophysical time series. *Nonlin. Processes Geophys., 11,* 561-566.

Guevara-Murua A., Williams C.A., Hendy E.J., Rust A.C., Cashman K.V., 2014, Observations of a stratospheric aerosol veil from a tropical volcanic eruption in December 1808: is this the Unknown ~ 1809 eruption? *Clim. Past., 10,* 1707-1722.

Haigh J.D., 1996, The impact of solar variability on climate. *Science, 272,* 981-984.

Hammer C.U., Clausen H.B., Dansgaard W., 1980, Greenland ice sheet evidence of post-glacial volcanism and its climatic impact. *Nature, 288,* 230-235.

Helama S., Mielikainen K., Timonen M., Eronen M., 2008, Finnish supra-long chronology extended to 5634 BC. *Norw. J. Geograph., 62,* 271-277.

Holmes R.L., 1983, Computer-assisted quality control in tree-ring dating and measurement. *Tree-Ring Bulletin., 44,* 69-75.

Kanatjev A.G., Shumilov O.I., Kasatkina E.A., 2014, Software for dendrochronological measurements. *Instruments and Experimental Techniques, 57,* 214-217.

Kasatkina E.A., Shumilov O.I., 2005, Cosmic ray-induced stratospheric aerosols: A possible connection to polar ozone depletions. *Ann. Geophys., 23,* 675-679.

Kasatkina E.A., Shumilov O.I., Lukina N.V., Krapiec M., Jacoby G., 2007, Stardust component in tree rings. *Dendrchronologia, 24,* 131-135.

Kasatkina E.A., Shumilov O.I., Timonen M., Kanatjev A.G., 2013, Consequences of powerful volcanic eruptions according to dendrochronological data. *Izvestiya, Atmospheric and Oceanic Physics, 49,* 432-438.

Lean J., Beer J., Bradley R., 1995, Recostruction of solar irradiance since 1610, Implications for climate change. *Geophys. Res. Lett., 22,* 3195-3198.

McCormick M.P., Thomason, L.W., Trepte C.R., 1995, Atmospheric effects of the Mt Pinatubo eruption. *Nature, 373,* 399-404.

Newhall C.G., Self S., 1982, The Volcanic Explosivety Index (VEI): An estimate of explosive magnitude for historical volcanism. *J. Geophys. Res., 87,* 1231-1238.

Ogle N., Turney C.S.M., Kalin R.M., O'Donnel L., Butler C.J., 2005, Palaeovolcanic forcing of short-term dendroisotopic depletion: The effect of decreased solar intensity on Irish oak. *Geophys. Res. Lett., 32.* doi: 10.1029/2004GL021623.

Rampino M.R., Self S., 1982, Historic eruptions of Tambora (1815), Krakatau (1883), and Agung (1963), their stratospheric aerosols and climatic impact. *Quater. Res.*, *18,* 127-143.

Rigozo N.R., Nordemann D.J.R., Echer E., Zanandera A., Gonzalez W.D., 2002, Solar variability effects studied by tree-ring data wavelet analysis. *Adv. Space Res., 29,* 1985-1988.

Robock A., 2000, Volcanic eruptions and climate. *Rev. Geophys., 38,* 191-219.

Sadler J.P., Grattan J.P., 1999, Volcanoes as agents of past environmental change. *Global Planet. Change., 21,* 181-196.

Schove D.J., 1955, The Suspot cycle, BD 649 to AD 2000. *J. Geophys. Res., 60,* 127-136.

Scuderi L.A., 1990, Tree-ring evidence for climatically effective volcanic eruptions. *Quater. Res.*, *34,* 67-85.

Shindell D.T., Schmidt G.A., Miller, R.L., Mann M.E., 2003, Volcanic and solar forcing of climate change during the Preindustrial Era. *J. Climate., 16,* 4094-4107.

Shumilov O.I., Kasatkina E.A., Henriksen K., Vashenyuk E.V., 1996, Enhancement of stratospheric aerosols after solar proton event. *Ann. Geophys., 14,* 1119-1123.

Shumilov O.I., Kasatkina E.A., Raspopov O.M., Turunen E., Jacoby G., 2000, An estimation of the climate response to the variations in solar and volcanic activity. *Geomagn. Aeron., 40,* 687-691.

Shumilov O.I., Kasatkina E.A., Lukina N.V., Kirtsideli I.Yu., Kanatjev A.G., 2007, Paleoclimatic potential of the northernmost juniper trees in Europe. *Dendrchronologia, 24,* 123-130.

Shumilov O.I., Kasatkina E.A., Mielikainen K., Timonen M., Kanatjev A.G., 2011, Palaeovolcanos, Solar activity and tree-rings from Kola Peninsula (northwestern Russia) over the last 560 years. *Int. J. Environ. Res., 5,* 855-864.

de Silva S.L., Zielinski G.A., 1998, Global influence of the AD 1600 eruption of Huaynaputina, Peru. *Nature, 393,* 455-458.

Sonnek K.M., Martensson T., Vieback E., Tunved P., Grahn H., Schoenberg P., Brannstrom N., Bucht A., 2017, The impacts of a Laki-like eruption on the present Swedish society. *Nat. Hazards, 88,* 1565-1590.

Soon W., Baliunas S., 2003, Proxy climatic and environmental changes of the past 1000 years. *Clim. Res., 23,* 89-100.

Stoffel M., Khodri M., Corona C., Guillet S., Poulain V., Bekki S., Guiot J., Luckman B.H., Oppenheimer C., Lebas N., Beniston M., Masson-Delmotte V., 2015, Estimates of volcanic-induced cooling in the Northern Hemisphere over the past 1,500 years. *Nature Geosci., 8,* 784-788.

Sunkara S.L., Tiwari R.M., 2016, Wavelet analysis of the singular spectral reconstructed time series to study the imprints of solar-ENSO-geomagnetic activity on Indian climate. *Nonlin. Processes Geophys., 23,* 361-374.

Svensmark H., Friis-Christensen E., 1997, Variation of cosmic ray flux and global cloud coverage – a missing link in Solar-climate relationships. *J. Atm. Terr. Phys., 59,* 1225-1232.

Thordarson T., Self S., 2003, Atmospheric and environmental effects of 1783 – 1784 Laki eruption: A review and re-assessment. *J. Geophys. Res., 108,* 4011-4019.

Torrence C., Compo G.P., 1998, A practical guide to wavelet analysis. *Bull. Am. Meteorol. Soc., 79,* 1998.

Vaganov E.A., Shiyatov S.G., 2005, Dendroclimatic and dendroecological research in Northern Eurasia. *Lesovedenie, No 4,* 18-27.

Velasco V.M., Mendoza B., 2008, Assessing the relationship between solar activity and

some large scale climatic phenomena. *Adv. Space Res., 42,* 866-878.

Vecchi G.A., Soden B.J., 2007, Global warming and the weakening of the tropical circulation. *J. Clim., 20,* 4316-4340.

Verosub K.L., Lippman J., 2008, Global impacts of the 1600 eruption of Peru's Huaynaputina. *EOS Trans., 89,* 141-142.

Wahl E.R., Diaz H.F., Smerdon J.E, Ammann C.M., 2014, Late winter temperature response to large tropical volcanic eruptions in temperate western North America: Relationship to ENSO phases. *Global Planet. Change, 122,* 238-250.

Wang X., Zhang Q.-B., 2011, Evidence of solar signals in tree rings of Smith fir from Sygera Mountain in southeast Tibet. *J. Atm. Sol.-Terr. Phys., 73,* 1959-1966.

White D.E., White J.W.C., Steig E.J., Barlow L.K., 1997, Reconstructing annual and seasonal climatic responses from volcanic events since A.D. 1270 as recorded in the deuterium signal from the Greenland Ice Sheet Project 2 ice core. *J. Geophys. Res., 102,* 19683-19694.

Wigley T.M.L., 2000, ENSO, volcanoes and record-breaking temperatures. *Geophys. Res. Lett., 27,* 4101-4104.

Zanchettin D., Bothe O., Graf H.F., Lorenz S.J., Luterbacher J., Timmreck C., Jungclaus J.H., 2013, Background conditions influence the decadal climate response to strong volcanic eruptions. *J. Geophys. Res., 118,* 4090-4106.

Geofísica Internacional (2018) 57-1: 79-86

Short Note

Evidence of small ferrimagnetic concentrations in mice (*Mus musculus*) livers and kidneys exposed to the urban dust : A reconnaissance study

Francisco Bautista, María E. Gonsebatt, Rubén Cejudo, Avto Goguitchaichvili, Ma. Carmen Delgado and Juan J. Morales

Received: August 15, 2017; accepted: November 09, 2017; published on line: January 01, 2018

Resumen

Investigaciones previas llevadas al cabo sobre el polvo y los suelos urbanos de la Ciudad de México revelaron una concentración relativamente alta de metales pesados debido a la contaminación atmosférica. Los análisis magnéticos detallados demostraron que las muestras de polvo urbano contienen una fase de magnetita neoformada procedente de la combustión de los vehículos. En este trabajo informamos los resultados de las medidas magnéticas realizadas en hígados y riñones de *Mus musculus* para evaluar si las partículas magnéticas pueden penetrar y acumularse en estos órganos vitales. Las medidas sistemáticas de la susceptibilidad magnética y las curvas de adquisición de magnetización remanente isotérmica atestiguan la existencia de pequeñas concentraciones de granos ferrimagnéticos de coercitividad baja / media (muy probablemente magnetita). Este estudio confirma que los minerales magnéticos finos pueden penetrar y llegar a hígados y riñones de ratones, en concentraciones relativamente pequeñas.

Palabras clave: Contaminación atmosférica, Ciudad de México, ratones, *Mus musculus*.

Abstract

Previous investigations carried out on Mexico City urban dust and soils revealed relatively high concentration of heavy metals due to the atmospheric pollution. Detailed magnetic analyzes demonstrated that the dust samples contain neo-formed magnetite phase coming from the vehicles combustion. Here, we report the results of magnetic measurements carried out on *Mus musculus* livers and kidneys in order to evaluate whether the magnetic particles may penetrate and accumulate in these organs. The systematic measurements of the magnetic susceptibility and isothermal remanent magnetization acquisition curves attest the existence of small concentrations of low/medium coercivity ferrimagnetic grains (most probably magnetite). This study confirms that fine magnetic minerals can penetrate and reach livers and kidneys of mice in relatively small concentrations.

Key words: Atmospheric pollution, Mexico City, mice, *Mus musculus*.

F. Bautista
Laboratorio Universitario de Geofísica Ambiental
Centro de Investigaciones en Geografía Ambiental
Universidad Nacional Autónoma de México
Morelia, Michoacán México
**Corresponding author: leptosol@ciga.unam.mx*

M.E. Gonsebatt
Laboratorio de Toxicología Ambiental
Instituto de Biomédicas
Universidad Nacional Autónoma de México
Ciudad Universitaria, México.

R. Cejudo
A. Goguitchaichvili
C. Delgado
J. Morales
Laboratorio Universitario de Geofísica Ambiental
Instituto de Geofísica
Universidad Nacional Autónoma de México
Unidad Michoacán, México.

Introduction

Ten micrometer diameter (PM_{10}), or less, fine particles of anthropic origin contain magnetic minerals and traces of heavy metals that may be evidenced by magnetic methods as already reported in previous works (Qiong *et al*., 2013; Ihl *et al*., 2015; Cortés *et al*., 2015, 2017). These studies have used different environmental samples (plant, soil, urban dust among others) to determine the relationship between the concentration of heavy metals (Cr, Cu, Pb, Zn, etc.) and some magnetic parameters (Wang, 2013; Cejudo *et al*., 2015). The magnetic susceptibility (κ_{lf}) and isothermal remanent magnetization values (IRM) up to 0.7 T have shown relatively good correlation with the concentration of the majority of heavy metals (Cd, Cr, Cu, Ni, Pb, V and Zn) (Evans and Heller, 2003; Qiao *et al*., 2011; Bautista *et al*., 2014; Cejudo *et al*., 2015). The poor air quality in mega cities is mainly related with gas emission by cars, as they systematically emit fine particles containing both magnetic materials and heavy metals. These fine particles accumulate on the surface of the soil, floors (concrete, pavement, paving stones, etc.) and constitute the urban dust (Bautista *et al*., 2011; Cejudo *et al*., 2015; Sánchez-Duque *et al*., 2015; INECC, 2011; 2016).

The population is naturally exposed to urban dust that may penetrate into the human body through oral ingestion, breathing and skin contact (Baroli *et al*., 2007; Kwon *et al*., 2008). In humans, the particles with a size of 2.5 microns in diameter can enter through the respiratory tract to the region of the pulmonary alveoli and ultra-fine particles (less than 1 micron in diameter) can even penetrate into the circulatory system (Forsman and Hogstedt, 1995).

Digestive system has an important role in nutrient acquisition within the stomach and intestines where food and liquids are mixed with digestive juices to transform it into smaller molecules, which are absorbed by the intestinal walls and driven by the blood and the hepatic vein to the liver (Townsend *et al*., 2014). After necessary nutrients have been taken by the body, the residual waste is sent to the blood through the kidneys, where the filtration is achieved to remove most toxins and other substances (pesticides, drugs and food additives). The wastes removal occurs in tiny units inside the kidneys called nephrons, which act as filters where waste and excess water are combined and become urine (Guyton and Hall, 2011).

The main objective of this study is to reveal (if any) and quantify the presence of magnetic minerals in livers and kidneys of mice exposed to urban dust.

Magnetic experiments

In order to know whether the urban dust potentially penetrates in mice vital organs, a specific experimental procedure was carried out using three types of urban dust from Mexico City with different (contrasting) values of mass specific susceptibility and isothermal remanent magnetization at 0.7 T. (DIL, DIIL, DIIIL) and a control (CL).

The urban dust was dried in the shade and sieved to 2 mm to remove the coarse-grained fraction from the gravel. The material was put into 8 cc plastic boxes, ideal for magnetic measurements. Magnetic susceptibility (κlf) was measured at low frequency (0.46 kHz) with a MS2B Bartington and isothermal remanent magnetization (IRM) up to 0.7 T obtained at room temperature using a pulse magnetizer IM-10 (ASC Scientific).

The values of mass specific susceptibility ($\chi lf = \kappa lf/\rho$, density) and $IRM_{0.7T}$ (at 0.7 T) were recorded for each urban dust samples. The urban dust was classified according to the measurements of mass specific susceptibility and isothermal remanent magnetization in low, medium and high values. A mixture of 1000 mL saline solution and 1 g of each urban dust was prepared. The mice were dosed with 16 ml per day during a total of twelve days.

Fifteen mice (*Mus musculus*) were divided into three lots; each lot was assigned a saline solution prepared with urban dust. The first lot of mice (Group I) was dosed with a urban dust solution having low values of $IRM_{7.0T}$; the second lot (Group II) was dosed with a urban dust solution having medium values of $IRM_{0.7T}$ and the third lot of mice (Group III) was dosed with a urban dust solution with high values of $IRM_{0.7T}$. A control lot of five mice was also used to which a saline solution without urban dust was applied.

The time and dosed amount of the solution was the same for each lot during twelve days. Twenty samples of liver and kidney were obtained after mice sacrifice. The organs were separated immediately after sacrifice, and frozen at -70^{0}C. The organ samples were preserved at 4 °C in 8 cc plastic boxes for magnetic measurements.

Once the saturation was achieved at 0.7 T, a magnetic field of 0.2 T was applied in the opposite direction to measure the $IRM_{-0.2}$ value and to determines the ratio S_{-200} ($S_{-200} = IRM_{-0.2} / IRM_{0.7}$). S_{-200} reflects the relative proportion of high coercivity minerals (values less than 0.75) and low coercivity minerals (values between 0.75 and 1.0) (Thompson and Oldfield, 1986; Bloemendal *et al*., 1992; Gubbins and Herrero-Bervera, 2007). All magnetizations were measured with a Molspin (ASC Scientific) and JR6 (AGICO) spinner magnetometers.

A simple variance analysis was performed between the groups of mice dosed with saline solution and the magnetic measurements (k_{lf}, NRM, $IRM_{0.7}$, $IRM_{0.2}$ and S_{-200}). A factorial variance analysis was carried out using as factor to organs (liver and kidney) and groups of urban dust. A medium comparison analysis was carried out (Statgraphic, 2007).

Main results, discusion and concluding remarks

The three urban dust samples exhibited different values of mass specific magnetic (χ_{lf}) and isothermal remanent magnetization ($IRM_{0.7T}$); urban dust I (group DIL) is characterized with relatively low value of $IRM_{0.7T}$ (27.7 $mAm^2\ kg^{-1}$); urban dust II (Group DIIL) with a medium value of $IRM_{0.7T}$ (49.0 $mAm^2\ kg^{-1}$) while the urban dust III (group DIIIL) yielded the highest value of $IRM_{0.7T}$ (95.2 $mAm^2\ kg^{-1}$) (Table I).

Table 1. Results of magnetic measurements of three urban dust groups.

Sample	χ_{lf} $\mu m^3\ kg^{-1}$	$IRM_{0.7T}$ $mAm^2\ kg^{-1}$
Dust I	2.1	27.7
Dust II	2.8	49.0
Dust III	3.3	95.2

After twelve days dosing, 20 samples of liver and kidney were respectively obtained. The average mass for all liver sample was 0.5 g and kidney reached 0.3 g. The magnetic parameters were not normalized by density, since it was impossible to determine the sample density without affecting the integrity of the material.

The negative initial susceptibility values obtained in liver samples are very likely due to the high concentration of diamagnetic material (mainly water and organic matter) (Table II). The natural remanent magnetization (NRM) yielded values between 0.0 to 0.1 mA m^{-1}; the $IRM_{0.7}$ provided values between 0.6 to 2.1 mA m^{-1}; the $IRM_{0.2}$ provided values between 0.6 to 2.1 mA m^{-1} and the S_{-200} ratio showed values higher than 0.8 (Figure 1 and Table II).

The kidney samples showed magnetic susceptibility values between -9.1 to 5.0 x 10^{-6} (SI); NRM values between 0.0 to 0.1 mA m^{-1}; $IRM_{0.7}$ values between 0.6 to 2.0 mA m^{-1}; the $IRM_{0.2}$ showed values between 0.6 and 2.0 mA m^{-1} and the S_{-200} ratio showed the higher values between 0 and 2.3. Values of S_{-200} close to 1.0 indicate high proportion of low coercivity minerals. In a single case however, R4S1 kidney sample showed a value less than 0.7 indicative of high coercivity minerals (Table II, Figure 2).

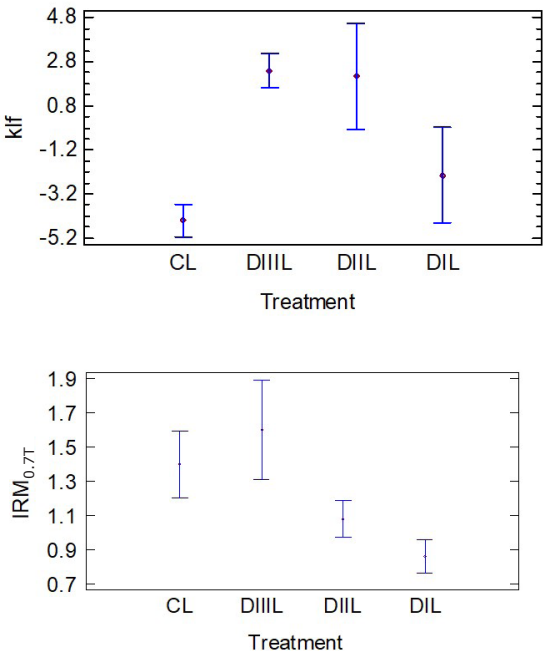

Figure 1. Box plot of magnetic susceptibility values and isothermal remanent magnetization at 0.7 T.

The variance statistical analysis yielded significant differences between the values obtained from liver samples. The highest values correspond to the DIII treatment with higher concentration of ferromagnetic minerals (Figure 1). In case of $IRM_{0.7}$ parameters, although significant changes were also detected, the values from control samples resulted relatively high most probably due to simple contamination.

The kidney samples associated with the high magnetic concentration urban dusts showed higher values of both susceptibility and $IRM_{0.7}$ as expected (Figure 2).

Table 2. Magnetic susceptibility and isothermal remanent magnetization values at 0.7 T for liver and kidney samples.

Sample	Weight g	K_{lf} x10^{-6}(SI)	NRM mA m^{-1}	$IRM_{0.7T}$ mA m^{-1}	$IRM_{-0.2T}$ mA m^{-1}	S_{-200}	S_{-25}
Liver samples							
Min	0.4	-10.5	0.0	0.6	0.6	0.8	0.85
Max	0.6	6.0	0.1	2.1	2.1	1.0	1.00
Mean	0.5	0.0	0.1	1.2	1.2	0.9	0.93
Kidney samples							
Min	0.2	-9.1	0.0	0.6	0.6	0.1	0.00
Max	0.4	5.0	0.1	2.0	2.0	2.3	0.70
Mean	0.3	-1.8	0.0	1.1	1.1	1.0	0.2

Magnetic parameters such as κ_{lf}, and $IRM_{0.7}$ showed that they could be used for the identification of magnetic signal in mouse organs by ingestion of urban dust. The natural remanent magnetization measurements were not adequate to identify the intake of magnetic particles in mice at low exposure.

The liver samples showed the highest concentrations of magnetic particles compared to the kidney samples. It follows that, at low exposure times to urban dust, damage could be detected first in the liver.

The IRM acquisition curves in liver samples exhibited the following behavior: between 0 to 100 mT fields, the remanent magnetization increases proportionally with the applied field. For magnetic fields between 100 to 200 mT, the growth of the magnetization stops and the saturation is reached. Liver samples of Group I showed relatively low values of saturation remanent magnetization ($IRM_{0.7}$ = 0.75 mA m^{-1}), while higher $IRM_{0.7}$ values were reported for group III ($IRM_{0.7}$ = 2.2 mA m^{-1}) (Figure 2 and 3).

High IRM values of 1.5 mAm^{-1} were recorded for kidney samples of group III, whereas samples of group II and I exhibited almost the same value of $IRM_{0.7}$ (1.2 mAm^{-1}, Figure 3).

The liver and kidney samples showed values of S_{-200} close to 1.0 indicating high proportions of low coercivity minerals (LCM) and low proportion of high coercivity mineral (HCM) (Figure 4).

The results obtained in this study showed that the liver and kidney of mice of *Mus musculus* species present significant magnetic response to the applied fields. The group of mice dosed with the highest concentrations of magnetic particles (dust III) yielded a higher concentration of magnetic minerals in their liver and kidney and vice versa. These experiments also indicated that low coercivity ferrimagnetic minerals (possibly magnetite) are present in in the liver and kidney of mice.

On the other hand, magnetic particles are being used in biomedical research because

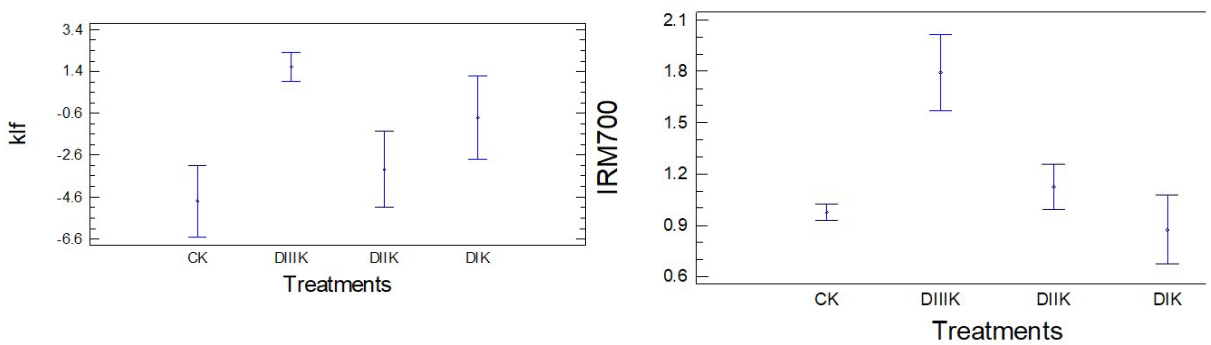

Figure 2. Magnetic susceptibility and isothermal remanent magnetization values at 0.7 T for kidney samples.

they can be carriers of drugs to attack malignant tumors (Chao *et al*., 2012) and to trap elements such as heavy metals and toxic substances in the blood (Ramanujan, 2009), and other apps (Li *et al*., 2016)..It is also known that magnetic particles in high concentration can cause cytotoxicity, DNA damage, oxidative stress, epigenetic events and inflammatory processes (Sing *et al*., 2010); Furthermore, it can accumulate in organs such as liver, brain, spleen and lungs subsequent to inhalation and penetration through hair follicles (Baroli *et al*., 2007; Kwon *et al*., 2008). However, little research has been done on the use of magnetic particles as indicators of contamination in animal tissues.

The distribution, transformations and biotransformations of the magnetic particles in the body are scarcely known (Levy *et al*., 2011).

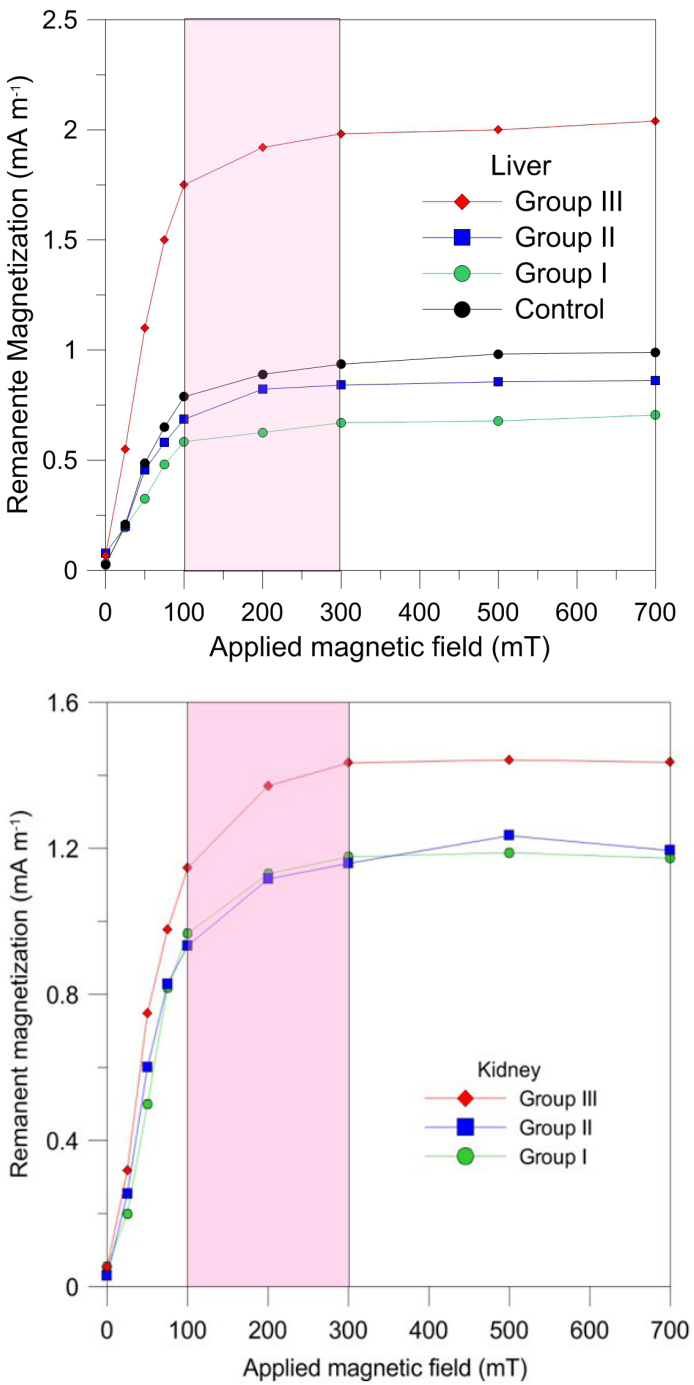

Figure 3. Isothermal remanent magnetization acquisition curves for liver and kidney *Mus musculus* samples.

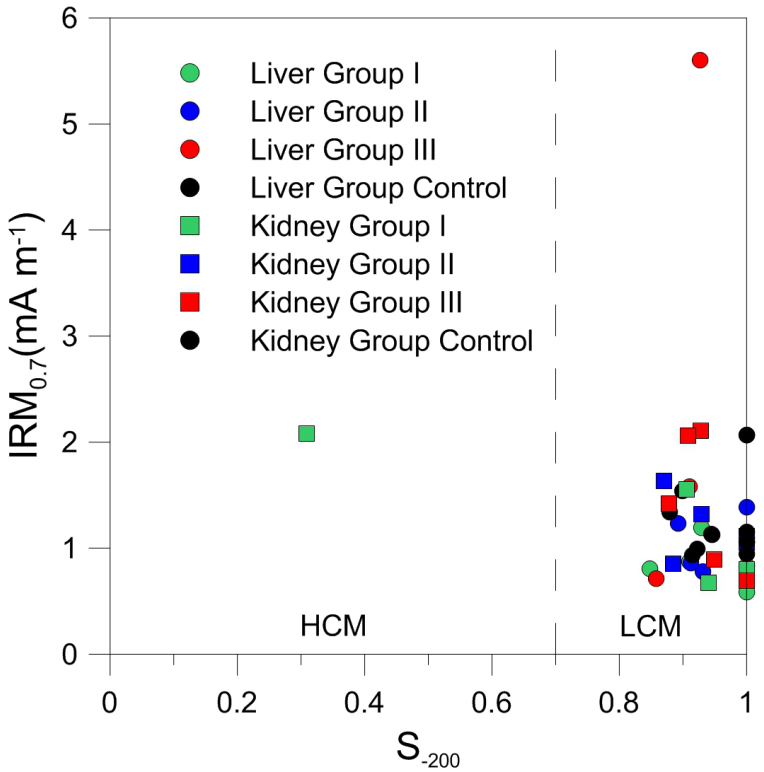

Figure 4. Relationship between S_{-200} and measures of $IRM_{0.7}$ for all liver (circles) and kidney (square) samples.

In addition, when the research is done with environmental samples, such as urban dust (mixture of particles in both size and chemical composition) very few studies are found.

These type of studies are relevant also for human health, showing that adults ingest approximately 50 mg per day of ambient dust and soil, while infants or children ingest twice as much (100-110 mg per day) (US EPA, 2011).

The main finding of the present study is that the liver was the organ with the highest magnetic signal. The kidney also achieved a magnetic signal but of smaller magnitude as compared with the liver.

This reconnaissance study confirms that fine magnetic minerals may be absorbed and stored by mice livers and kidneys in relatively small concentrations but also in small exposure time. The same mechanism may be speculated for the human vital organs. However, more experiments are required considering: a) a higher mice population; b) longer exposure to urban dust; c), the introduction of control lots; and e) the identification of the magnetic particles.

Acknowledgments

To Secretaria de Ciencias, Tecnología e Innovación de la Ciudad de México for the financial support of the project SECITI/051/2016. We thank the National Science and Technology Council (*CONACYT)* for the financial support CB-2011-01-169915. Authors would like to thank Hilda Rivas for technical support.

References

Baroli B, Ennas MG, Loffredo F, Isola M, Pinna R, Lopez-Quintela MA. 2007. Penetration of metallic nanoparticles in human full-thickness skin. J Invest Dermatol. 127:1701–12.

Bautista F., J.L. Palacio H. Delfín y (Eds.). 2011. Técnicas de muestreo para el estudio del manejo de recursos naturales y el cuidado del ambiente. Centro de Investigaciones en Geografía Ambiental. Universidad Nacional Autónoma de México. México D.F. 790 pp.

Bautista F., Cejudo R., Aguilar B., Goguichaisvili A., 2014. El potencial del magnetismo en la clasificación de suelos: una revisión. *Bull. Soc. Geol. Mex. 66, 2*, 365-376.

Bloemendal, J., King, J.W., Hall, F.R., and Doh, S.-J., 1992. Rock magnetism of Late Neogene and Pleistocene deep-sea sediments: relationship to sediment source, diagenetic processes, and sedimentlithology. Journal of Geophysical Research, 97: 4361–4375

Cejudo R., Bautista F., Quintana P., Delgado A., Aguilar A., Goguitchaisvili A., Morales J., 2015. Correlación entre elementos potencialmente tóxicos y propiedades magnéticas en suelos de la Ciudad de México para la identificación de sitios contaminados: definición de umbrales magnéticos. *Rev. Mex. Cienc. Geol. 32, 1,* 50-61.

Cortés J.L.; F. Bautista; P. Quintana; D. Aguilar y A. Gogichaishvili. 2015. El color del polvo urbano como indicador de contaminación por elementos potencialmente tóxicos: El caso de Ensenada, Baja California. Revista Chapingo Serie Ciencias Forestales y del Ambiente. 20 (2): 255-266. Doi: dx.doi.org/10.5154/r.rchscfa.2015.02.003.

Cortés J.L.; F. Bautista; P. Quintana; y A. Gogichaishvili. 2017. Distribución espacial de los metales pesados en polvos urbanos de la ciudad de Ensenada, Baja California, México. Revista Chapingo Serie Ciencias Forestales y del Ambiente. 23(1): 235-248.

Chao, X, Zhang Z, Guo L, Zhu J. Peng M., Vermorken A., Van de Ven W, Chen C. and Cui Y. 2012. A novel magnetic nanoparticle drug carrier for enhanced cancer chemotherapy. Plos one 7(10), e40388, https://doi.org/10.1371/journal.pone.0040388

Evans M.E., Heller F., 2003, Environmental Magnetism- Principles and Applications of Enviromagnetics. Int. Geophysics Ser., 86, Academic press, Amsterdam, 293 pp.

Forsman M and Hogstedt P 1995. Total lung dust inverse solutions in single plane SQUID magnetopneumography¨ Biomagnetism: Fundamental Research and Clinical Applications (Amsterdam: Elsevier) pp 793–7.

Guyton A., Hall J., 2011. Tratado de fisiología médica. Barcelona España, Elsevier. 12 edición, 1083 pp.

Gubbins D. and HerreroBervera E., 2007. Encyclopedia of Geomagnetism and Paleomagnetism, Springer, Heidelberg, 1072 p.

Kwon JT, Hwang SK, Jin H, Kim DS, Minai-Tehrani A, Yoon HJ, Han DY, Kang YW, Yoon BI, Lee JK, Cho MH. 2008. Body distribution of inhaled fluorescent magnetic nanoparticles in the mice. J Occup Health; 50:1–6.

Ihl T., F. Bautista, R. Cejudo*, C., Delgado*, AvtoGoguichaishvili, P Quitana y D. Aguilar. 2015. Concentration of toxic elements in topsoils of Metropolitan area of Mexico City: A spatial analysis using Ordinary Kriging and Indicator Kriging. RevistaInternacional de ContaminaciónAmbiental. 31: 42-62.

INECC. Instituto Nacional de Ecología, 2011, Guía metodológica para la estimación de emisiones de PM2.5, INE-Semarnat, México D.F. 105 pp.

INECC. Instituto Nacional de Ecología, 2016, Metalespesados, http://www.inecc.gob.mx/sqre-temas/763-aqre-metales, consultado en enero 2016.

Kwon JT, Hwang SK, Jin H, Kim DS, Minai-Tehrani A, Yoon HJ, Han DY, Kang YW, Yoon BI, Lee JK, Cho MH. 2008. Body distribution of inhaled fluorescent magnetic nanoparticles in the mice. J. Occup. Health;50:1–6.

Levy M., Wilhelm C., Luciani N., Deveaux V., Gendron F., Luciani A., Devaud M. and GazeauF.,2011. Nanomagnetism reveals the intracellular clustering of iron oxide nanoparticles. *Nanoscale*, 3, 4402.

Li XM, Wei JR, Aifantis KE, Fan Y, Feng Q, Cui F, Watar F. 2016. Current investigations into magnetic nanoparticles for biomedical applications.*J. Biomed. Mater Res. A*. 104(5):1285–1296.

Qiao Q., Zhang C., Huang B., Piper J., 2011. Evaluating the environmental quality impact of the 2008 Beijing Olympic Games: magnetic monitoring of street dust in Beijing Olympic Park, *Geophys. J. Int.,187*, 1222–1236.

Qiong W., Xiao-Hui B., Jian-Hui W. Yu-Fen Z., Yin-Chang F. 2013. Heavy metals in urban ambient PM10 and soil background in eight cities around China, Environmental Monitoring and Assessment, 185:1473–1482.

Ramanujan R.V. 2009. Chapter 17 Magnetic Particles for Biomedical Applications.En: R. Narayan (ed.), BiomedicalMaterials. Springer. 467-491 pp. DOI 10.1007/978-0-387-84872-3 17.

Sánchez-Duque, A.*, F. Bautista, A. Gogichaishvili, R. Cejudo-Ruiz, J. Reyes-López, F. Solís-Domínguez y J. Morales-Contreras. 2015. Evaluación de la contaminación ambiental a partir del aumento magnético en polvos urbanos - Caso de estudio para la ciudad de Mexicali, México. Revista Mexicana de Ciencias Geológicas. 32:501-513.

Singh, N., Jenkins, G. J. S., Asadi, R., and Doak, S. H. 2010. Potential toxicity of superparamagnetic iron oxide nanoparticles (SPION).Nano Reviews, 1, 10.3402/nano.v1i0.5358. http://doi.org/10.3402/nano.v1i0.5358

Statgraphic 2007, ANOVA Simple, 1-24, http://www.statgraphics.net/wp-content/uploads/2011/12/tutoriales/ANOVA%20Simple.pdf consulted on february 3, 2016.

Thompson, R., Oldfield, F., 1986, Environmental Magnetism: London, Allen and Unwin, 227 pp.

Townsend C., Beachamp R., Marck B., Mattox K., 2014, Sabiston Cirugía General y del Aparato Digestivo, Barcelona España, Elsevier., 576 p.

U.S. EPA. Exposure Factors Handbook 2011 Edition (Final).U.S. Environmental Protection Agency, Washington, DC, EPA/600/R-09/052F, 2011.

Wang X. 2013. Assessment of heavy metal pollution in Xuzhou urban topsoils by magnetic susceptibility measurements. Journal of Applied Geophysics, 92, 76-83.